Numerical Simulation of Magnetohydrodynamically Accelerated Hypersonic Channel Flows

by

Thomas Evan Kava

B.S.M.E, Baylor University, 2018

A thesis submitted to the

Faculty of the Graduate School of the

University of Colorado in partial fulfillment

of the requirements for the degree of

Doctor of Philosophy

Department of Aerospace Engineering Sciences

2023

Committee Members:

John Evans, Co-Chair

Iain Boyd, Co-Chair

Igor Adamovich

Hisham Ali

Robyn Macdonald

Kava, Thomas Evan (Ph.D., Aerospace Engineering Sciences)

Numerical Simulation of Magnetohydrodynamically Accelerated Hypersonic Channel Flows

Thesis directed by Prof. John Evans and Prof. Iain Boyd

Designing air-breathing hypersonic engines that fly at mesospheric altitudes is challenging due to the harsh aerothermal environments at those conditions and the limits of combustion. Magnetohydrodynamic (MHD) accelerators that leverage electromagnetic fields to generate thrust can overcome these limitations at low pressures. However, before using electromagnetic fields for propulsion at hypersonic conditions can become a reality, calculations must be performed to identify the operating conditions and inform the design of these systems.

This work will perform calculations based on one-dimensional MHD theory to outline the operational requirements and inform the design of hypersonic MHD accelerators. Past hypersonic MHD accelerator attempts have primarily focused on adding total enthalpy to hypersonic wind tunnel facilities. However, the engines studied here will operate at much lower static pressures where the Hall effect is significant. First-order Hall parameter predictions are given for various altitude conditions, and electric field requirements are discussed to guide numerical simulations.

Two numerical tools for simulating MHD accelerated hypersonic channel flows will be presented. The first tool, LeMANS-MHD, is a multi-dimensional hypersonic computational fluid dynamics code based on the low magnetic Reynolds number assumption. LeMANS-MHD, which couples the flow field to the electromagnetic field via a generalized Ohm's law solver, is used to discuss the complicated flow field structure in MHD accelerator channels. For MHD acceleration to be successful, the Lorentz force must overcome adverse pressure gradients due to Joule heating and viscous deceleration. Several numerical and physical challenges to advancing the state-of-the-art low-pressure hypersonic MHD accelerator technology are discussed. The second tool, a one-dimensional inviscid MHD solver, has been developed to guide multi-dimensional simulations and provide design insights for future prototypes. The one-dimensional model is capable of quickly performing design studies while also accounting for several physical effects such as ionization, recombination, and the Hall effect. Performance predictions are given for a range of hypersonic flight conditions. It is found that the Lorentz efficiency and the thrust coefficient improve as altitude increases. However, decreased performance is expected due to Joule heating as the inlet Mach number is increased.

To my grandparents.

Acknowledgements

First off, I would like to thank my entire committee for their guidance during my time in graduate school. Our discussions have been enlightening and have played a significant role in keeping me on track during this project. I especially want to thank my advisors, Dr. Iain Boyd and Dr. John Evans, as I could not have asked for a better co-advisorship. I am also indebted to the many fruitful discussions with Dr. Igor Adamovich, along with the data he provided that became fundamental to my research.

I am also thankful for the community of graduate students at CU Boulder, especially the students in the FSM office, including members of both NGPDL and CMGLab. I am particularly grateful for the guidance provided by senior lab members and postdocs Dr. Ross Chaudhry, Dr. Pawel Sawicki, Dr. DeAnna Gilchrist, and Dr. Aviral Prakash and the following labmates for all of the valuable feedback and collaboration throughout the years as well as making graduate school (through a pandemic!) much easier: Tim Aiken, Amin Taziny, James Wright, Jeff Hadley, Jenny Horing, Jens Rataczak, Kal Monroe, and Mitch Wall.

Finally, I want to thank all of my family and friends who have helped me get to this point, specifically my mom, dad, brother, and sister, who have been a constant source of love and emotional support. Finally, thank you, Aimee, for your unending patience and support. I could not have made it this far without you by my side.

Lockheed Martin supported this work under award number MRA17-003-RPP020. I thank Tom McGuire and Artan Qerushi at Lockheed and the team of researchers at The University of Queensland for all of their assistance.

Contents

Tables

Table

Figures

Figure

Chapter 1

Introduction

Since the invention of the Wright Flyer and its first flight in 1903, engineers have pushed the envelope to fly faster and further than ever before. This constant pursuit of innovation has led to many ground-breaking propulsion technologies for airplanes, spacecraft, and satellites. Today, vehicles flying at low speeds and low altitudes employ gas-powered turbines to generate thrust. Turboprops, turbofans, and turbojets, for example, power the vast majority of fixed-wing commercial aircraft that sustain the global economy. In all of these engines, compressors are used to increase the pressure of the freestream air such that the combustor can operate efficiently. However, as the vehicle moves faster, the compression due to it's motion is sufficient for combustion. High-speed engines that do not require compressors are called *ramjets*. The dimensionless *Mach number*, which is the ratio of velocity, u, to the local speed of sound, a, can distinguish flight regimes where vehicles are traveling fast enough such that compressors are no longer needed.

$$M = \frac{u}{a} \tag{1.1}$$

As the Mach number increases, engine design requirements change considerably. Not only are ramjets more efficient when the Mach number is greater than one, but they are a feasible propulsion system only when the vehicle is moving sufficiently fast. A secondary propulsion system is needed for vehicles with ramjet engines at rest and moving less than Mach 1 (subsonic). Once the vehicle is flying faster than Mach 1 (supersonic), a diffuser is still necessary to decelerate the freestream air to subsonic velocities in the combustor. When the vehicle is moving much faster than the

Figure 1.1: **NASA X-43A scramjet attached to a Pegasus rocket being carried by a B-52. The B-52 took the X-43A/Pegasus assembly to 12 km altitude, where it would detach and climb using the rocket until the scramjet separated and ignited at approximately 30 km. This single image contains three of the most common combustion-based engines: 1) gas turbine engine (B-52), 2) rocket motor (Pegasus), and a 3) scramjet engine (X-43). [2]**

speed of sound (hypersonic), a significant loss in total pressure occurs when slowing the freestream flow to subsonic speeds, and so supersonic combustion becomes an additional requirement for efficient operation, which is the case for supersonic combustion ramjets, or *scramjets*. Due to the extreme thermal and structural loads that occur at hypersonic velocities, scramjets are typically integrated into the vehicle's airframe. Freestream air compression is provided by oblique shock waves originating from the leading edge of the vehicle.

Meanwhile, operations that require access to higher altitudes and speeds call for combustion-based rocket engines. Contrary to turbine engines, rocket engines carry fuel and oxidizer on board, allowing continued thrust generation even when the atmosphere is less dense. Combustion-based air-breathing engines are limited by the need to mix the fuel and maintain high stagnation pressures. On the other hand, rocket engines are limited by the need to carry fuel, reducing payload capabilities. All technologies listed thus far have been developed extensively and integrated into high-speed flight vehicles.

Table 1.1 lists a sample of the different high-speed flight vehicle programs and nominal Mach numbers and altitudes they achieved. During the 1960s, interest in flying faster than the speed of sound led to famous commercial and defense programs such as the Concorde supersonic airliner and SR-71 "Blackbird," which employed sophisticated afterburning turbojets [7, 8]. It was not until the turn of the century that scramjets succeeded in full scale flight tests with the X-43 and X-51 programs, for example, flying at speeds greater than Mach 5, commonly cited as the hypersonic regime's lower bound [9, 10]. In reality, what separates supersonic flight from hypersonic flight is the presence of real gas processes that affect the heating and composition of the vehicle's surface. At hypersonic Mach numbers, the flow's total enthalpy is high enough to dissociate oxygen and nitrogen molecules. Atomic oxygen is highly reactive and can significantly degrade standard aerospace-grade materials. Furthermore, as a gas passes through a strong shock, it can no longer be considered calorically perfect since the internal energy modes excite and relax relative to one another at different time scales comparable to the relatively short flow residence times. Thus, sophisticated thermodynamic models are necessary for accurately predicting heating rates [11, 12].

All of the systems included here operated at altitudes of 30 km and lower, except for the X-15 program, which flew to an altitude of 108 km [13]. Rocket engines enabled such high-altitude flight for the X-15 due to the advantages just mentioned. The other powerplants relied on air-breathing technologies and, thus, were bound to altitudes where the air was dense enough to generate thrust though combustion.

Earth's atmosphere can be divided into five distinct layers: the troposphere, stratosphere, mesosphere, thermosphere, and exosphere. The two layers closest to Earth's surface, the troposphere and stratosphere, extend to approximately 20 km and 50 km altitude, respectively. Most air-breathing hypersonic flight tests have occurred in the upper troposphere and lower stratosphere

Table 1.1: Notable vehicle programs and their engine systems.

Year	Aircraft	Mach No.	Altitude	Engine
1963	North American X-15	Mach 5.58	108 km	Rocket
1964	Lockheed Martin SR-71	Mach 3.3	25 km	Turbojet
1967	North American X-15	Mach 6.7	30 km	Rocket
1969	Aérospatiale/BAC Concorde	Mach 2	18 km	Turbojet
2004	NASA X-43A	Mach 9.68	33 km	Scramjet
2013	Boeing X-51	Mach 5.1	21 km	Scramjet

due to the constraints on combustion at high altitudes and thermo-structural loads at lower altitudes. The flight envelope between these two limits can be defined by the respective dynamic pressures, approximately 9.6 kPa (or 200 psf) and 96 kPa (or 2000 psf). The trajectory conditions between the air-breather limit and the dynamic pressure limit make up the *air-breathing corridor* [14, 15]. Vehicles with scramjets on board have been envisaged to operate single-stage-to-orbit (SSTO) missions within this air-breathing corridor. Figure 1.2 depicts the air-breathing corridor bounded by the 9.6 kPa and 96 kPa dynamic pressure limits. The region of altitudes above the air-breathing corridor is labeled *MHD Acceleration*, which will be discussed below. Other propulsion systems would be needed to accelerate an SSTO vehicle from Earth's surface to hypersonic speeds and to provide the final ascent into orbit.

Once in orbit or near orbit, smaller chemical thrusters or electric propulsion systems are used for station-keeping and attitude control. Chemical thrusters typically provide much more thrust than electric thrusters but with less specific impulse. Electric propulsion includes a variety of concepts that convert electrical power to thrust with applications to both air and spacecraft. These concepts include electrothermal, electrostatic, and electromagnetic thrusters that are differentiated by the mode in which they achieve propellant acceleration [16].

Electrostatic technologies such as gridded ion and Hall-effect thrusters have been used aboard satellites for decades because they are mass efficient (high specific impulse), and low thrust levels are adequate for the vacuum environment in space. Gridded ion thrusters apply a voltage drop across a series of grids that accelerate heavy ions out of the engine. The maximum thrust available

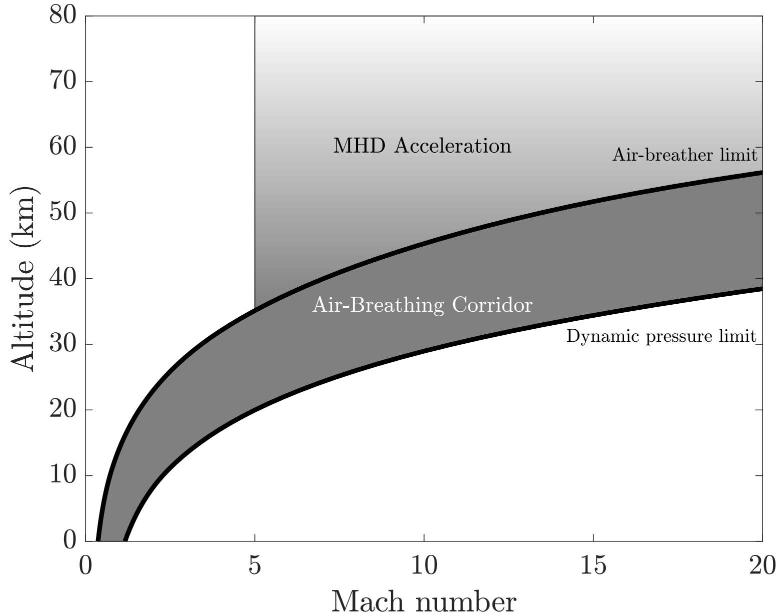

Figure 1.2: **Air-breathing corridor with corresponding limits and MHD acceleration region.**

for gridded-ion thrusters is subject to space charge limitations that offset the applied electric field strengths. On the other hand, Hall-effect thrusters can maintain plasma quasi-neutrality in the engine and deliver higher thrust per power [17].

Propulsion systems that rely on electromagnetic acceleration can deliver higher thrust densities while still achieving high specific impulses. In electrostatic thrusters, magnetic fields are commonly used to trap electrons to specific trajectories but are not used directly to accelerate the charged propellant. Electromagnetic thrusters convert electrical energy to kinetic energy via the Lorentz force through applied or induced crossed electromagnetic fields. The magnetoplasmadynamic thruster, which leverages current between an annular cathode and anode to induce a magnetic field configuration that yields thrust, has been studied for several decades due to its high thrust promise. However, the technology has yet to reach the level of technological maturation that gridded ion and Hall effect thrusters have due to the immense power requirements and electrode degradation issues [18]. Furthermore, applying electromagnetic forces to generate thrust with higher-density gases, such as those in Earth's atmosphere, has received much less development.

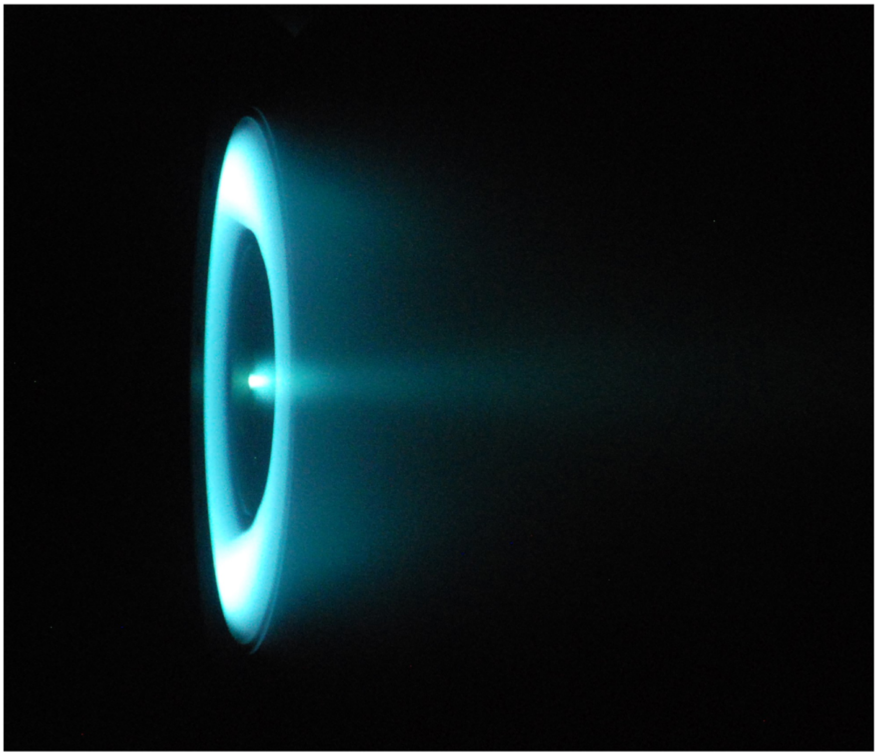

Figure 1.3: **The University of Michigan H9 Hall thruster in operation [3].**

The study of low-frequency processes in plasmas as continuous fluids can be classified by the field of magnetohydrodynamics (MHD) [19]. Engineers have studied using MHD body forces for aerodynamic purposes such as high-speed flow acceleration and power generation for several decades. MHD acceleration is advantageous to other airbreathing technologies because it is less constrained by the limited energy density of chemical fuel. Furthermore, it is unnecessary to mix the fuel with freestream air, nor must the air be compressed to the stagnation pressures appropriate for combustion. Alternatively, systems that use electric fields to generate thrust, such as MHD accelerators, avoid these issues yet they have seen less development in the past several decades due to the inherent engineering challenges they are associated with. However, as technology advances in the fields of material science and electromagnetic power generation among others, there has been a renewed interest in magnetohydrodynamic acceleration. As such, the need to model these systems and simulate their behavior is a critical task.

1.1 MHD Accelerators

In 1958, Resler and Sears highlighted the promise of using MHD to augment high-speed plasma flows. They introduced several potential applications of the technology and presented the fundamental theory that describes the behavior of the governing equations for these types of flows [20]. One such application is converting electromagnetic energy into kinetic energy of channel flows through electrodes in contact with the plasma. This concept first received engineering attention in the development of hypersonic wind tunnels. One critical challenge in hypersonic vehicle development is the lack of ground-based facilities that simulate all aspects of actual flight. For instance, in continuous blowdown facilities where a gas is pressurized and then expanded through a converging-diverging nozzle, it is possible to create relatively long-duration (seconds to minutes) high-speed flow environments over a test article at a total enthalpy much lower than flight. On the other hand, impulse facilities such as shock tunnels, which use unsteady shocks to heat a test gas before expanding, provide higher total enthalpies for shorter durations (milliseconds) [21].

In search of solutions for long-duration high enthalpy hypersonic wind tunnel facilities, engineers looked toward MHD flow augmentation, typically by using the Lorentz force to add energy to the working gas as it is expanding through the nozzle upstream of the test section. However, leveraging the Lorentz force in this manner requires sufficient electron populations. These programs typically seeded the working gas with vaporized alkali metals such as cesium, sodium, or potassium to achieve adequate electrical conductivity for MHD interaction due to their relatively low ionization potentials. The first ionization energy of cesium atoms is roughly 3.9 eV, compared to 15.6 eV for nitrogen molecules [22, 23]. However, these metals can contaminate the freestream and corrode the wind tunnel's walls and test sections.

Table 1.2 contains a list of some notable MHD accelerators conceived for improving hypersonic wind tunnel and propulsion performance and their nominal flow characteristics at the inlet to the MHD portion of the tunnel[1] . In the 1960s, the United States Air Force (USAF) Arnold

[1] Note that the data in this table is approximate and meant to provide a sense of the operating conditions for each application. For some of these tunnels, values such as Mach number and pressure could be varied. For others,

Engineering Development Center (AEDC) and the National Aeronautics and Space Administration (NASA) Langley Research Center (LaRC) spearheaded MHD wind tunnel development using seeded gas. Around the same time, General Electric Company (GE) developed an unseeded wind tunnel that circumvented the disadvantages of using alkali metals by relying on thermal ionization. The prospect of using unseeded airflows was revisited at the end of the century by MSE Technology Applications, Inc. during the Magnetohydrodynamics Accelerator Research Into Advanced Hypersonics (MARIAH) Project. As a result of this project, Adamovich et al. compared the performance of MHD accelerators using both unseeded and seeded airflows in the application of energy addition to high-speed wind tunnels [24]. In this study, they found that nonequilibrium ionization through electron beams was not feasible at high pressures due to significant decay in electron populations. However, at lower pressures (≤ 1 atm), it was found that electron beams were able to increase total flow enthalpy through MHD acceleration.

The outcomes of the MARIAH project are not just limited to comparing seeded and unseeded flows. Reference [25], the project's final report, also contains a more comprehensive account of past MHD accelerator attempts with various outcomes. Some programs were built and operated, while others did not make it out of the conceptual development phase. Among the more successful programs is the MHD wind tunnel at The Central Aerohydrodynamic Institute in Russia (TsAGI), which operated for several decades. Through the MARIAH project, engineers from MSE collaborated with Russian researchers and shared insights, such as the inevitable difficulties in achieving practical high-speed MHD acceleration.

The fate of several of the other programs was less operationally successful due to lack of funding. For example, the AEDC HiRHO program was shut down before a test facility could even be constructed. On the other hand, most of the projects generated valuable knowledge and literature that was passed down to future researchers. One of these programs, the Magnetohydrodynamic Augmented Propulsion Experiment (MAPX), evaluated the use of MHD augmentation on thermal

tunnels were never built, but analyses were performed at these nominal conditions. The values in the 'Year' column are associated with reports and articles detailing their efforts.

Table 1.2: MHD augmented hypersonic wind tunnel facilities.

Year	Facility	Gas	Seed	Mach No.	p (atm)	Refs.
1963	AEDC LoRho	Nitrogen	NaK	2.6	0.45	[26, 27, 28]
1963	GE	Air	-	2.6	30	[29, 30]
1964	NASA LaRC	Nitrogen	Cs	1.6	0.07	[31, 32, 33]
1969	Aerospace Corp.	Nitrogen	KN_3	3.8	5.5	[34]
1972	AEDC HiRho	Air	K_2CO_3	2.9	4.3	[27, 35]
1960s-90s	Russia TsAGI	Air	NaK	1.9	0.3	[25, 36]
1998	MSE MARIAH	Air	Cs	1.2	40	[25]
2003	NASA MAPX	Nitrogen	NaK	1.4	3.2	[37, 38]
2003	NASA EAST	N_2O-N_2	K_2CO_3	2.1	0.54	[6]
2008	MSE MARIAH II	Air	E-Beam	9.5	0.10	[25, 39, 40]
2018	TsAGI	Air	NaK	2.0	0.25	[41]

propulsion systems [37]. Although this project suffered from several programmatic delays, it led to several fruitful analytical, computational, and experimental analyses. Another notable example of successful MHD accelerator operation was for the Electric Arc Shock Tube (EAST) at NASA Ames [6]. Using a potassium-based seed and an air-like mixture, they were able to back out several valuable quantities, such as bulk electric conductivity, using back EMFs at unpowered electrodes. Finally, a follow-up to the MARIAH program included the Radiantly Driven Hypersonic Wind Tunnel (RDHWT) project, which introduced electron beams as a means of efficient ionization for MHD acceleration [25]. Reference [39] discusses the benefits of using electron beams as an external ionization mechanism. It should be noted here that each of these MHD channels is operating at higher pressures than might be seen in high-altitude flight since they are for wind tunnel applications. However, as will be seen, the low-pressure nature of the flows in this work will significantly impact the design and simulation of the technology explored in this work.

1.1.1 Plasma Fueled Engines

The hypersonic air-breathing propulsion system studied here is intended for high-hypersonic flight over a broad range of altitudes. This concept, named the plasma fueled engine (PFE), first ionizes the working gas with beams of high-energy electrons and then accelerates the newly formed plasma using crossed electric and magnetic fields. Figure 1.4 shows a cartoon of a PFE geometry where the applied electric field is generated mutually transverse to the magnetic field and the flow by a series of segmented electrodes. Segmentation aids in offsetting Hall currents that detract from the overall efficiency of the configuration. Additionally, segmentation allows for the separate conditioning of electrode pairs or sets of electrode pairs, increasing overall acceleration in the PFE.

The magnetic field, however, is generated by an external electromagnet, which would be contained in the vehicle's body. Generating magnetic fields that are strong enough for high-speed flow augmentation while also being low-weight has been a historically difficult challenge. However, as electromagnet technology continues to advance, carrying a powerful electromagnet on board an aircraft becomes an even more feasible endeavor. In this example PFE configuration, an electron beam region is placed upstream of the MHD accelerator portion of the channel. The beams are shot along the magnetic field lines to ensure the beam electrons travel across the channel.

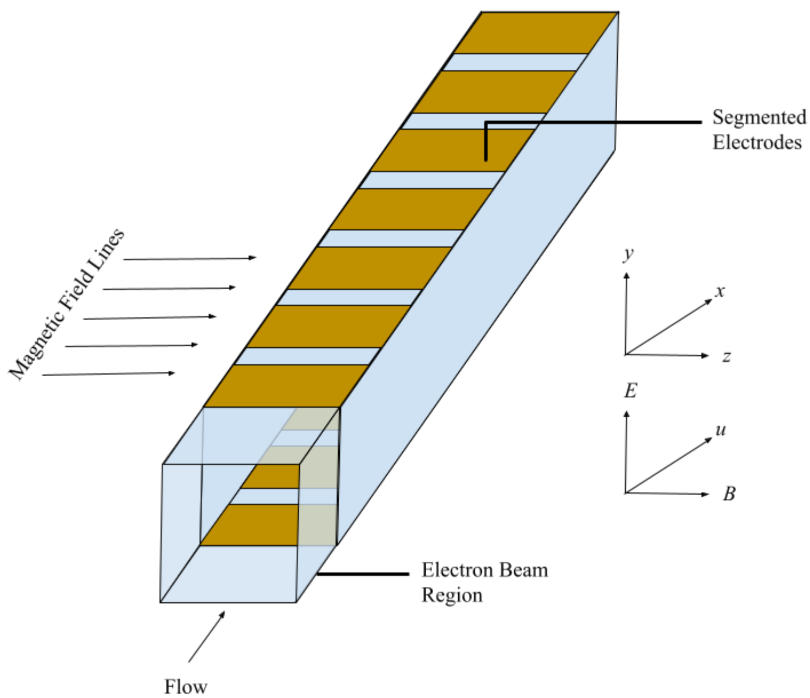

Figure 1.4: **Configuration of PFE model geometry in 3D.**

Determining the magnetic field strength, electrode configuration, and channel geometry for optimal performance at a given operating condition is challenging. Fortunately, analytical and numerical models already exist that can be leveraged to make discoveries regarding the design and operation of hypersonic MHD accelerators. With the scarcity of hypersonic ground testing facilities and the expense of flight testing, these models are integral to technological development.

A primary goal of the work in this thesis is to simulate flows in any given PFE configuration using computational fluid dynamics (CFD). Since the PFE uses electromagnetic fields to accelerate plasmas and achieve hypersonic propulsion, an interdisciplinary approach is necessary. These flows constitute a unique combination of high-speed aerodynamics, electromagnetics, and chemical kinetics. Namely, these hypersonic flows consist of weakly ionized plasmas in thermochemical nonequilibrium under applied electromagnetic fields. In order to study PFE flows in full detail, an array of advanced tools such as Navier-Stokes solvers, electromagnetic field solvers, along with high performance computing (HPC) resources are necessary.

To achieve the goal of simulating flows in the PFE and advancing the state-of-the-art modeling of MHD accelerators in general, it will first be necessary to identify and implement the appropriate physical and numerical models into the available research codes. Subsequently, analyses will be performed into the relative importance of these models on the final flow field solutions. Once the essential models have been identified, the fundamental physical processes present in the PFE will be investigated in detail. By gaining a deep understanding of the key physical processes and the relationships between them, it will ultimately be possible to define design guidelines and operating envelopes for future PFE prototypes.

1.2 Previous Modeling of MHD Accelerators

Engineers and scientists have been attempting to model the behavior of high-speed MHD channel flows since the AEDC and NASA LaRC wind tunnel programs in the early 1960s. The seminal work by Resler and Sears, *The Prospects for Magneto-Aerodynamics* [20], established the now abundant literature concerning magnetohydrodynamically augmented high-speed flows. This field encapsulates MHD generators, MHD accelerators, MHD deceleration for entry, descent, and landing (EDL) vehicles, and more. However, the modeling of MHD generators and accelerators, more specifically, began with a paper also by Resler and Sears that directly followed *Prospects* named *Magneto-Gasdynamic Channel Flow* [42]. In this paper, the authors elaborate more on channel flows subject to electromagnetic manipulation, which leads to the distinction of two closely related ideas, MHD generation and MHD acceleration. As their names suggest, MHD generation converts the kinetic energy of the oncoming flow into electrical power that can be extracted and used elsewhere. MHD acceleration is the opposite regime where electrical power adds kinetic energy to a flow.

The theory regarding MHD channel flows was advanced in 1964 in a paper by Culick [5], where the behavior for simplistic MHD augmented channel configurations was predicted using one-dimensional theory for any combination of inlet velocity and Mach number. The results from this work are very useful because it is shown that subsonic flows can become supersonic in constant area ducts while obeying the second law of thermodynamics. However, perhaps more relevant to this work, the behavior of any supersonic flow where acceleration is the goal is qualitatively illustrated. It turns out that only the inlet velocity and Mach number are needed to specify the electromagnetic configurations that permit acceleration of supersonic flows.

Throughout the 1960s, fundamental research into MHD generators and accelerators continued, especially in the one-dimensional setting. However, due to the lack of success in constructing a functional MHD accelerator facility and a decrease in hypersonic funding, interest in modeling these flows died out in the latter half of the twentieth century. Meanwhile, MHD generation continued to experience continued development to improve the efficiencies of steam power plants. These efforts lead to a much broader literature base for MHD generators than accelerators. However, many central concerns that apply to generators also apply to accelerators. The MHD acceleration analyses of the time, especially in the 1960s and early 1970s, used semi-analytic models to derive tunnel performance estimates using some of the insights from the references above and other seminal texts such as Refs. [43, 44, 45].

In the mid-1980s, investment in hypersonic technologies, such as high-speed air-breathing engines, began to experience a resurgence. A set of quasi-one-dimensional tools was used to solve the governing equations of MHD numerically accelerated flows by The University of Tennessee Space Institute (UTSI) [46]. This was one of the first examples of computational fluid dynamics (CFD) to be applied successfully to an MHD accelerator study. Using Ohm's law and an equilibrium conductivity calculator for alkali metal-seeded air, they were able to implement Lorentz force and Joule heating terms in their solvers and perform comprehensive trade studies of various MHD accelerator configurations for wind tunnel applications. Notably, UTSI had also constructed a three-dimensional software package for investigating the interactions between the electromagnetic and flow fields in MHD generators by this point [47].

Interest in using MHD generation and acceleration in hypersonic flight was reinvigorated in the early 1990s with the introduction of the Russian AJAX concept [48]. The AJAX hypersonic vehicle concept mainly consists of a hydrocarbon-fueled scramjet engine with an MHD generator upstream of the combustion region and an MHD accelerator downstream. This system, which gave birth to what is now known as the MHD-bypass scramjet, converts the kinetic energy of the freestream flow to electricity for on-board power supplies. Additionally, it decelerates and compresses the oncoming air for more optimal combustion downstream. Some of the energy extracted in the MHD generator can then be directed to the MHD accelerator downstream of the combustor for additional gains in thrust.

Near the turn of the century, the MARIAH II/RDHWT program pioneered research into electron-beam-driven MHD acceleration as it presented a promising mechanism for efficiently ionizing cold hypersonic flows. Consequently, Macheret et al. performed the first one-dimensional analysis of an electron-beam powered MHD accelerator [39]. The authors demonstrated that this technology indeed showed true potential in accelerating hypersonic flows. Their quasi-one-dimensional modeling consisted of the inviscid Euler equations for chemically reacting flows in thermal nonequilibrium between the vibrational and translational modes.

Inspired by the AJAX concept and the progress in modeling electron beam ionization, Macheret et al. also investigated using electron beams and electromagnetic fields to distort the shock structure in scramjet inlets [49]. Their two-dimensional inviscid modeling showed that the

MHD system could increase performance in off-design conditions. The two-dimensional model in this work consisted of the Euler equations for flows in thermochemical nonequilibrium. Electron-beam ionization was further studied in the quasi-one-dimensional and two-dimensional analyses by Parent et al. in their work on the magnetoplasma jet engine, which utilized MHD acceleration for hypersonic propulsion [50, 51].

Three-dimensional simulations, including viscous effects, were performed by Gaitonde in 2006 [52]. This work solved the Navier-Stokes equations under the low magnetic Reynolds number assumption for an MHD bypass scramjet geometry with electron beam ionization. It was shown that three-dimensional vortical structures due to shock-boundary layer interactions significantly affected the flow solution within the engine. The electrical conductivity profiles were assumed to follow modified Gaussian profiles across the engine. They included effects from combustion through a source term in the energy equation. Individual species were not tracked, and a single temperature was used.

One-dimensional analyses were also performed in the early 2000s, especially by researchers in Japan from Nagaoka University of Technology [53, 54, 55]. These studies solved the quasi-one-dimensional equations of motion under thermal and chemical equilibrium for seeded gases such as air and argon. Comparisons between working gases and channel configurations were performed to evaluate the performance of each at different operating conditions. Interestingly, these papers found behavior in their numerical simulations that can be described by the analytical theories of the 1960s. The work in Chapter 4 of this thesis concretely links the one-dimensional accelerator theory to numerical simulations using modern computational techniques and physical models.

In the 2000s, the MAPX program constructed a test facility to address the engineering challenges of MHD accelerators [37]. To support this effort, Turner et al. developed a three-dimensional MHD model that solved the parabolized Navier Stokes (PNS) equations [56]. In this work, they made significant updates to an already existing code, which allowed the simulation of general MHD generator/accelerator configurations. Namely, they performed parametric studies to determine an optimal design configuration for preliminary tests. Additionally, it was found that three-dimensional flow structures significantly impacted the flowfield.

More recently, Parent et al. have developed a coupled drift-diffusion and Navier-Stokes solver for plasmas with significant non-neutral and quasi-neutral regions [57, 58]. This solver uses Ohm's law to solve for the electric field instead of Gauss' law, which is commonly done in most drift-diffusion models. By doing so, they are able to integrate both sets of equations simultaneously. This differs from loosely coupled strategies in which the sets of equations are solved independently, as in Refs. [59, 60]. The drift-diffusion model is frequently used to study discharge applications where substantial regions of non-neutrality form around electrodes by solving the equations of motion for positively and negatively charged species [61, 62, 63].

The Navier-Stokes equations have also been modified to include source terms to examine the effect of applied electromagnetic fields on high-speed flows. These source terms range from phenomenological modes based on experiments [64] to coupled Gauss' and Ohm's law solvers [65, 66]. Scalabrin and other members of the Nonequilibrium Gas and Plasma Dynamics Laboratory (NGPDL) developed an unstructured finite volume code that solves the Navier Stokes equations [67]. This CFD code is intended for weakly ionized hypersonic flows in thermochemical nonequilibrium. Bisek later modified LeMANS to study MHD flow control approaches by implementing a finite volume generalized Ohm's law solver [68]. LeMANS-MHD is the code used in this work to develop the appropriate two-dimensional and three-dimensional models to study the PFE. Details of LeMANS-MHD are given in the next chapter.

Although the above provides a brief historical account of the research that has led up to the present work, it is not exhaustive. Magnetohydrodynamic devices have a broad range of applications in hypersonic flows. Although interest in developing these technologies has fluctuated over the decades, it remains crucial to the success of these systems that the state-of-the-art modeling methodologies are advanced.

1.3 Outline of This Dissertation

Answering every open question about the design and performance of low-pressure hypersonic MHD accelerator systems in a single self-contained document would be insurmountable. Thankfully, that is not the objective of this dissertation. Instead, the goal of this dissertation is to advance the state-of-the-art understanding and design of these systems through the use of numerical modeling. Simulating every physical process and interaction down to the atomic level would be intractable. Thus, various assumptions and physical models are needed in a numerical framework to achieve this goal. Although some information may be lost in these models, they can still provide valuable intuition about the behavior of these flows. For example, the bounds of feasibility can be explored, and opportunities for technological maturation can be identified. The rest of the thesis will attempt to do precisely that. The remaining five chapters are briefly summarized below.

Chapter 2 will begin by introducing at a very high level some fundamental physical concepts that need to be modeled when using numerical simulations to understand and inform hypersonic MHD accelerator design. Then, the governing equations of gas dynamics, followed by Maxwell's equations of electromagnetics, are presented. When plasmas are subjected to external electromagnetic fields, the trajectories of the charged particles are changed, thus affecting the bulk motion of the plasma. In doing so, the charged particles generate their own electromagnetic fields such that the macroscopic dynamics of the plasma alter the applied fields. This two-way coupling must be captured in the governing equations before numerical discretization. The coupling strategy, along with all necessary assumptions, is described and will be used to arrive at a set of magnetohydrodynamic equations for flows in thermochemical nonequilibrium. Finally, two numerical tools that will be used to solve these equations will be described in detail. The first of which is the previously mentioned LeMANS-MHD. The second code is a one-dimensional Euler equation solver with MHD source terms capable of running on a desktop computer in minutes. The benefits of LeMANS-MHD include obtaining a more detailed description of the flow physics in PFE systems. However, the gain in detail comes at the cost of computational expense. Due to fast characteristic timescales of chemical reactions, thermal relaxation, and MHD interaction, simulating these flows through complex geometries can require hundreds of thousands of CPU hours, if not more.

Conversely, with modern computational hardware available to everyday consumers, the one-dimensional PFE model can simulate these flows on time scales more applicable to engineering conceptual design and analysis. The results will guide problem setup parameters for higher-fidelity simulations, develop design intuition, and provide first-order performance predictions. Thus, these two tools will be employed hand-in-hand to achieve the goals of this dissertation. However, with the scarcity of high-quality experimental data relevant to this work, back-of-the-envelope calculations must first be performed to bestow confidence in the numerical simulations.

These back-of-the-envelope calculations can be found in Chapter 3. The presence of electromagnetic fields modifies the classical relations of compressible gas dynamics. These modifications are significant when considering channel flows, as the Mach number is no longer just a function of the cross-sectional area and heat addition. Fortunately, analytical solutions for quasi-one-dimensional channel flow with MHD augmentation were found over half a century ago. These seminal works summarized their findings and described the behavior of compressible MHD channel flows in a compact form under several assumptions, which have proven to be an integral piece of this research. The assumptions, such as scalar conductivity, were necessary to find closed-form solutions to the governing equations. However, as will be seen, anisotropic effects due to the magnetic field substantially impact PFE design, especially at mesospheric altitudes. Electrode placement and bias relative to the applied magnetic field differentiate several canonical MHD channel designs. First-order estimates of the charged particle collision frequency will be used to quantify the magnetic field effects and inform which mode of operation is most effective at a given flight condition. Finally, baseline power and ionization requirements will also be provided.

With the one-dimensional MHD channel theory in place, one-dimensional numerical simulations will be performed in Chapter 4. Several regimes of MHD flow acceleration will be probed to demonstrate the one-dimensional solver. From the analytical solutions to the governing equations, it is known that only the inlet Mach number, inlet velocity, electric field strength, and magnetic field strength are needed to predict the behavior of the one-dimensional solutions qualitatively. However, it will be seen how the boundary conditions impact the numerical solutions for various operating conditions by comparing them to the analytical solutions. Several assumptions will be gradually relaxed, such as constant cross-sectional area channels, electric field strengths, scalar conductivities, and electron populations. Plasma transport property and chemistry models are needed to address the two latter assumptions and will be provided for argon-based systems. Using these models, the importance of recombination will be quantified for various altitudes, which is necessary to know for electron beam placement. Additionally, one-dimensional simulations at a nominal operating condition will be performed that account for ionization, recombination, and magnetic field effects on conductivity. Performance predictions will be given for a range of operating conditions in the potential operating envelope of hypersonic MHD accelerators. Although the one-dimensional solver is valuable in understanding the balance between critical processes such as acceleration, heating, ionization, and recombination, it cannot capture several higher-dimensional effects.

Multidimensional results using LeMANS-MHD will be discussed in Chapter 5. Again, several assumptions are made initially to demonstrate the behavior of the solver. A simple two-dimensional test case is constructed that will facilitate a discussion of the boundary conditions and generic properties of both the flow field and the electromagnetic field. This test case consists of high-speed flow through two continuous electrodes. Then three-dimensional simulations will be performed for a segmented electrode MHD accelerator geometry based on the NASA EAST facility [6]. The three-dimensional structure of the electric field will be described in detail which highlights how nonuniform properties across the channel affect performance. Then, the flow field will be described and compared to the one-dimensional theoretical and numerical predictions. Additionally, a two-dimensional simulation that includes the Hall effect will be presented, and some of the design and simulation challenges for low-pressure hypersonic MHD acclerators will discussed.

Finally, Chapter 6 contains a set of conclusions that summarizes the findings from each chapter. Furthermore, suggestions are made for future work simulating low-pressure hypersonic MHD accelerator systems. As mentioned above, it is not in the scope of this dissertation to answer every open question regarding the behavior of these systems. In fact, by providing answers to some of the most pertinent and fundamental questions, it will be seen that more questions arise. This dissertation intends to provide a firm ground to launch future investigations using the numerical tools described herein. However, it is noted that the lessons learned herein will also be helpful to those using different toolboxes and methodologies since the analyses presented here are meant to be fundamental. Physical and numerical models not contained in this work may be necessary to match experimental data when it becomes available. However, the rudimentary intuition gained from these analyses should still be applicable when determining the overall feasibility and optimal design of PFE systems.

Chapter 2

Mathematical Formulation

When the original concepts of MHD augmented high-speed flows were originally being introduced, research was primarily restricted to experimental investigations, analytical analyses, and back-of-the-envelope calculations [42, 20, 43]. However, at the time and still today, access to ground testing facilities remains a rare and expensive resource. Sixty years later, computational power has increased dramatically, and detailed simulations can be carried out before technologies even reach the ground testing phase. Furthermore, with the development of high-performance computing (HPC) and computational fluid dynamics (CFD), early-stage design and analysis of MHD augmented flows can be performed to determine the feasibility of such systems with reduced risk to available resources.

Numerical simulation of MHD augmented flow technologies can be performed to predict the performance of ground-testing prototypes and eventually flight-test vehicles. However, the appropriate computational models must be identified, developed, and applied to the relevant CFD tools before simulations can even begin. This chapter introduces the models used in this research to analyze PFE systems. First, a brief description is provided of the most fundamental processes that must be captured for a high speed plasma under applied electromagnetic fields. Next, the baseline systems of equations that govern both the flow field and the electromagnetic field are provided. Then, the three-dimensional CFD code that will be used in this work, LeMANS, with the appropriate physical models to simulate high-speed, MHD-augmented, laminar flows is presented. Finally, a reduced one-dimensional inviscid MHD model is shown to provide design guidance and highlight the underlying theory of MHD accelerated channel flows at engineering analysis time scales.

2.1 Overview of Physical Processes in PFE

The complex interaction between electromagnetic fields and partially ionized plasmas is inherently challenging to model due to the many physical processes the individual particles experience. For example, the disparate masses of electrons and ions can lead to electron thermal velocities much greater than those of heavier ions and neutrals. This orders of magnitude difference in velocity leads to issues with standard integration techniques that attempt to solve the transport equations of each species independently. Furthermore, the governing equations can exhibit numerical stiffness for domains that have both non-neutral regions and quasi-neutral regions when the electric field is found via Gauss's Law [69, 57]. Furthermore, the flow field and electromagnetic field coupling is highly nonlinear, so numerical solutions are difficult to find, much less analytical.

For a numerical framework to have any level of predictability toward physical MHD accelerated hypersonic systems, it must encapsulate at least the most dominant microscopic and macroscopic processes. Below is a non-exhaustive list of such processes that charged particles experience in high-speed partially ionized plasma channel flows:

(1) elastic and inelastic collisions with other particles

(2) gas dynamic effects such as shocks and high-temperaure boundary layers

(3) drift due to the electric and magnetic fields

Particle collisions can be broadly classified into two main categories. The first are *elastic collisions*, where the particles' momentum and kinetic energy are exchanged. In this type of collision, the chemical structure of the particles is assumed to be unchanged. Conversely, in *inelastic collisions*, the second type of collision, the chemical structure of the colliding particles can change. Examples of these inelastic collisions include electronic excitation, molecular dissociation, and ionization. In the absence of electromagnetic fields, the particles of a gas can travel freely in between collisions. A particle's average distance traveled between collisions is called the *mean free path* [70]. The hard sphere mean free path, λ, may be written as a function of the particle's diameter, d, and the number density of the gas, n.

$$\lambda = \frac{1}{\sqrt{2}\pi d^2 n} \tag{2.1}$$

When the mean free path is small compared to some characteristic length scale of the flow, the fluid can be considered a continuum wherein macroscopic quantities such as temperature can be defined in an infinitesimal volume of many individual particles. Since the particles experience many collisions in a short period, they can equilibrate kinetic energies efficiently through elastic collisions. However, when an electric or magnetic field is present, whether applied externally or induced by the particles themselves, the paths between collisions may change substantially for charged particles.

2.1.1 Drift in Electric and Magnetic Fields

To first describe the influence of an electromagnetic field on a charged particle, we may turn to the Lorentz force law given in Eq. (2.2), where $\vec{F}$ is the force on the particle, q_s is the particle's charge, $\vec{E}$ is the electric field vector, $\vec{B}$ is the magnetic field vector, and $\vec{v}$ is the velocity of that particle.

$$\vec{F} = q_s \left(\vec{E} + \vec{v} \times \vec{B}\right) \tag{2.2}$$

The Lorentz force law states that the acceleration of a charged particle is the sum of the force in the direction parallel to the electric field and the force in the direction perpendicular to the magnetic field. Figure 2.1 shows a positively charged particle's path for several electromagnetic field configurations. The first is a constant magnetic field through the page with no electric field in the plane parallel to the page. In this case, the charged particle orbits around the magnetic field lines with radii proportional to the particle's mass. If there is an electric field parallel to the magnetic field, then the particle will travel along the magnetic field lines in helical orbits. Note

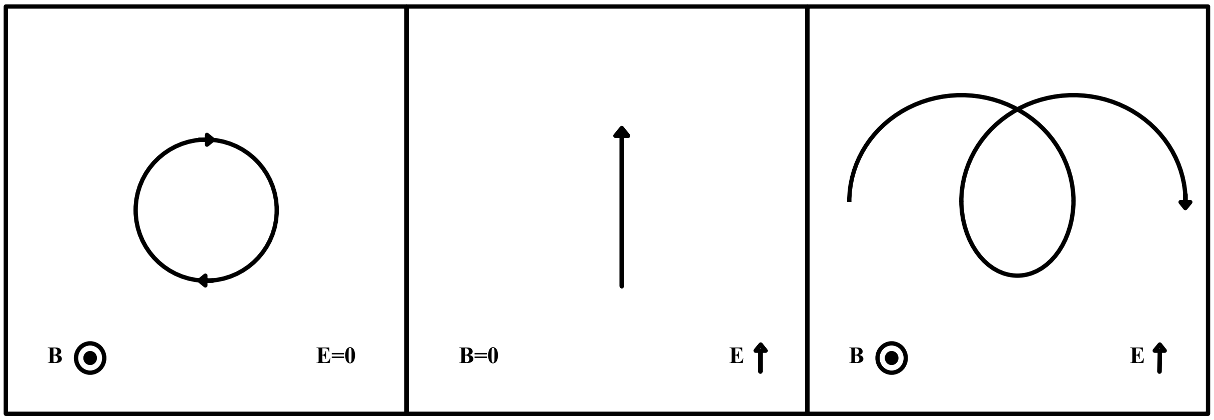

Figure 2.1: **Positively charged particle motion in a magnetic field, electric field, and crossed electric and magnetic fields.**

that a negatively charged particle orbits in the opposite direction.

In the next case, there is no magnetic but an electric field in the plane parallel to the page. Without the magnetic field, the positive charges drift in the direction of the electric field, while negative charges travel in the opposite direction. Finally, when there are crossed electric and magnetic fields, the particle gains energy in the half of its orbit that is in the direction of the electric field and loses energy in the other half. Due to this constant cycle between acceleration and deceleration, the particle then begins to drift in the direction normal to the electric and magnetic fields. Since negatively charged particles orbit and drift in the opposite directions than the positively charged particles, they gain energy in the same half of the orbit leading to a $\vec{E} \times \vec{B}$ drift in the same direction.

If the gas is dense enough, the charged particles will collide with other particles in the plasma. If the electromagnetic field is oriented in the appropriate direction, the charged particles deliver momentum to the neutral particles through these collisions, generating thrust by converting electromagnetic energy into kinetic energy [16]. To determine how the charged particles drift through the plasma and interact with the rest of the particles, the *collision frequency*, ν, and the *cyclotron frequency*, ω, must be known. The latter is a function of the magnetic field strength and particle mass, m.

$$\omega = \frac{q_e|\vec{B}|}{m} \tag{2.3}$$

If the cyclotron frequency is high and the charged particles undergo many revolutions around the magnetic field lines in between collisions, the drift will be entirely in the $\vec{E} \times \vec{B}$ direction. However, if the cyclotron frequency is sufficiently high enough for both positively and negatively charged particles, then $u_- = u_+$, and the current density will be zero. Conversely, if the cyclotron frequency is low relative to the collision frequency, then each orbit will be interrupted by a collision with another particle, and the drift will be primarily in the direction of $\vec{E}$. The ratio of cyclotron frequency to the collision frequency is called the Hall parameter, β_s, for each charged species, where ν_{sH} is the collision frequency of the charged species and heavy particles in the plasma.

$$\beta_s = \frac{\omega_s}{\nu_{sH}} \tag{2.4}$$

In practice, ν_{sH} is difficult to compute exactly, so the Hall parameter itself is typically calculated using the appropriate model for *mobility*. The Hall parameter for a species can be computed as the product of its mobility, μ_s, and the magnetic field strength.

$$\beta_s = \mu_s|\vec{B}| \tag{2.5}$$

Under the action of an electric field, mobility relates the drift velocity, $v_{d,s}$, of a charged species to the electric field strength. As the charged particle is accelerated by the electric field, it also loses energy through collisions with other particles until a finite drift speed is sustained. As such, the mobility is a function of primarily the gas composition, electric field strength, and density.

$$v_{d,s} = \mu_s|\vec{E}| \tag{2.6}$$

Consider a plasma made up of neutral particles, positive ions, and electrons. Due to the large mass disparity between the positive ions and the electrons, the mobility for electrons ends up being much greater than that of the positive ions [4]. Likewise, the electrons contribute the majority of the total electric current density. As such, both quantities will primarily be described by the electron values, i.e. $\beta = \beta_e$ and $\mu = \mu_e$.

Following the classification outlined in Ref. [4], there are four regimes in which a magnetized plasma exists. In all cases $\beta_i \ll \beta_e$. The first regime, is when both the ion and electron Hall parameters are very small, i.e. $\beta_i \ll \beta_e \ll 1$. In this case, both ions and electrons drift in the direction of the electric field. If the magnetic field strength increases such that $\beta_i \ll 1$ and $\beta_e \gtrsim O(1)$, then the ionic drift is unaffected by the magnetic field, but the electrons begin to drift in the direction normal to both the electric and magnetic fields. With further increase of the magnetic field strength, such that $\beta_e \gg 1$ and $\beta_i \lesssim O(1)$, then the electrons drift solely in the $\vec{E} \times \vec{B}$ direction. And finally, when both $\beta_e \gg 1$ and $\beta_i \gg 1$, then both ions and electrons drift in the $\vec{E} \times \vec{B}$ direction and the net current drawn goes to zero. These four regimes are illustrated in Fig. 2.2.

2.1.2 Electron Swarm Parameters

In addition to momentum transfer elastic collisions, inelastic collisions between particle plasmas will also significantly impact the behavior of MHD systems. Due to the high velocity of the low-mass electrons, many inelastic processes depend on the mean electron energy. For example, if the electric field is strong enough, the electrons will have enough energy to ionize the neutral particles, thereby releasing an additional electron which will subsequently gain energy in the electric field and create more electrons. This electron cascade will increase electrical conductivity but may lead to arcing between electrodes [63].

The Boltzmann equation for electrons can be used to solve for the most important transport properties and ionization rate coefficients in a plasma. Thankfully, several well-documented electron Boltzmann equation solvers are available to calculate these plasma properties. One remarkably easy-to-use and freely available software developed for precisely this purpose is BOLSIG+. The electron Boltzmann equation for a plasma is written as

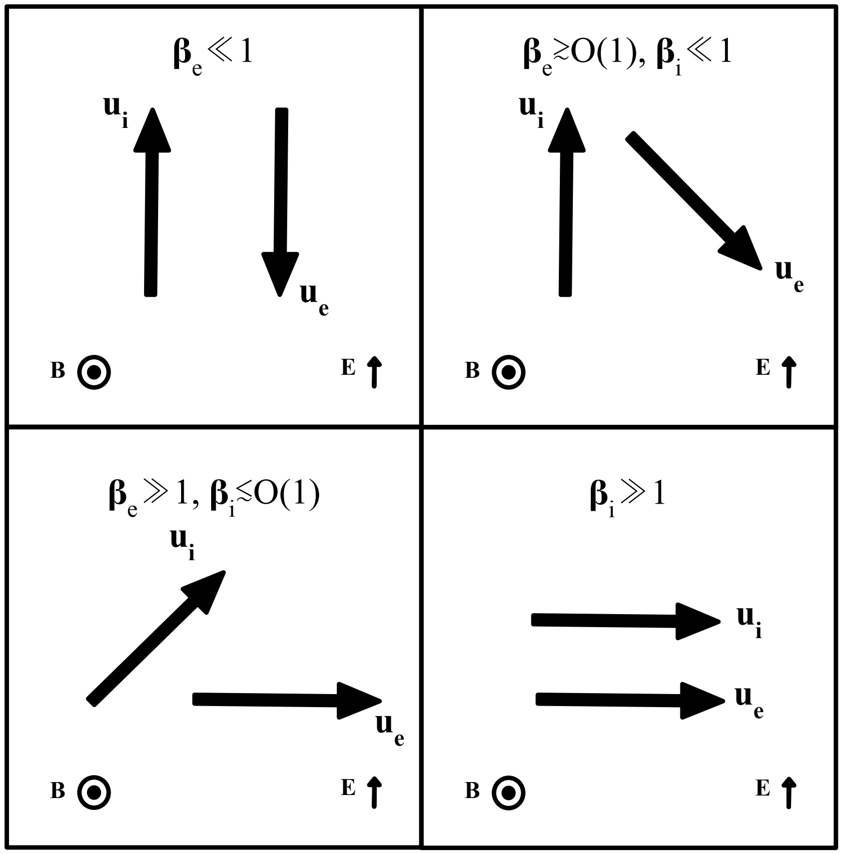

Figure 2.2: **Particle motion in crossed electric and magnetic fields for varying regimes of Hall parameter taken from the description given in Ref. [4].**

$$\frac{\partial f}{\partial t} + \vec{v} \cdot \nabla f - \frac{q_e}{m_e}\vec{E} \cdot \nabla_v f = C[f] \tag{2.7}$$

where f is the electron energy distribution function in three respective spatial and velocity coordinates, $\vec{v}$ is velocity, and $C[f]$ is the collision operator which takes account of the change in electron energy due to collisions. BOLSIG+ employs a two-term approximation in which f is split into an isotropic part and an anisotropic part. More details about the implementation of BOSLIG+ can be found in Ref. [71].

Several important quantities can be determined from the electron distribution function. The equations used by BOLSIG+ to compute some of the relevant properties to this work, such as mean electron energy, electron mobility, and ionization rate coefficients, are repeated below. The isotropic part, f_0, can be written in terms of the electron energy distribution function, denoted by F_0. Once F_0 is found by solving Eq. (2.7), the electron energy density, $\bar{\epsilon}$ can be computed as

$$\bar{\epsilon} = \int_0^\infty \epsilon^{3/2} F_0 d\epsilon \tag{2.8}$$

and electron mobility can be calculated as

$$\bar{\mu} = -\frac{1}{3N\bar{\epsilon}} \left(\frac{2q_e}{m_e}\right)^{1/2} \int_0^\infty \frac{\epsilon}{\tilde{\sigma}_m} \frac{\partial F_0}{\partial \epsilon} d\epsilon \tag{2.9}$$

where $\tilde{\sigma}_m$ is the effective momentum-transfer cross-section and N is the total gas density. Finally, rate coefficients, such as the ionization rate coefficient of a target species, are calculated by

$$k_r = \left(\frac{2q_e}{m_e}\right)^{1/2} \int_0^\infty \epsilon \sigma_r F_0 d\epsilon \tag{2.10}$$

where σ_r is the cross-section for collision process, r.

2.2 Three-Dimensional Governing Equations

Given the intricate coupling between charged particles, neutral particles, and the electromagnetic fields in a plasma, separately tracking each particle becomes a difficult, if not intractable, task for high-density flows. Methods such as Direct Simulation Monte Carlo (DSMC) and Particle-In-Cell (PIC) have proven successful at this task for rarefied gases and plasmas. For higher-density flows, methods that treat the fluid as a *continuum* offer alleviation from this burden. The Knudsen number can be used to determine when each of these approaches is appropriate. The Knudsen number, Kn, defined in Eq. (2.11), is the ratio of the mean free path to a characteristic length scale, L, of the problem of interest.

$$Kn = \frac{\lambda}{L} \tag{2.11}$$

Several options are available for defining the mean free path and characteristic length scale of a flow. For example, the freestream mean free path and characteristic vehicle land could be used for simulating a hypersonic vehicle. However, in hypersonic flows, the mean free path can vary drastically in different regions of the flow where the macroscopic properties also vary. Furthermore, employing a Knudsen number based on flow gradient length scales was found to better predict continuum breakdown than vehicle length-based Knudsen numbers [72]. DSMC methods have frequently been used to determine probabilistic solutions to the Boltzmann equation for rarefied hypersonic flows when the Knudsen number is large. In these methods, computational particles, representing many actual particles in a system, are directly tracked in a Lagrangian frame of reference. Interactions between walls and other particles are accounted for through corresponding physical models. Similarly, PIC methods also track particles in a Lagrangian frame of reference. However, with the added complexity, charged particles experience acceleration by applied and induced electromagnetic fields.

When the fluid of interest is dense enough, collisions are frequent such that the particle distribution functions in six-dimensional phase space are no longer needed. Instead, the velocity distribution function can be treated as Maxwellian at each point in space. In this case, the conservation equations of magnetohydrodynamics can be derived by taking a series of moments of the Boltzmann equations. The equations of magnetohydrodynamics have long been used to investigate the behavior of both laboratory and interstellar plasmas when the time scales of the flow are much greater than the plasma frequency time scales. The mathematical description of magnetohydrodynamic problems varies greatly from *ideal MHD*, where the plasma is assumed to be extremely electrically conductive, to *resistive MHD*, where the plasma has a finite resistance.

Furthermore, the plasma can be treated as a single bulk electrically conductive fluid or modeled as a combination of multiple fluids. A common multi-fluid approach is one where neutral particles, positive ions, negative ions, and electrons are all grouped separately. Identifying the appropriate set of governing equations and how to solve those equations is not a trivial task. A balance between physical fidelity and computational complexity is needed for studying most practical engineering problems of interest. With less physical fidelity, stronger assumptions are needed to find solutions. With greater physical fidelity, more computational resources are required.

The following sections outline the governing equations, assumptions, and the computational tools used to solve them in this work.

2.2.1 Fluid Dynamics Equations

Modeling flows in PFEs consists of two main parts. The first is the Navier-Stokes equations which govern multidimensional viscous flows. Since PFEs are intended for hypersonic flight and leverage nonequilibrium ionization through high energy electron beams, chemical reactions, ionization, and thermal nonequilibrium are expected. The effects of these processes on the conserved properties are captured via the appropriate source terms on the right-hand side of each governing equation. Below are the conservation of mass, momentum, and energy for a chemically reacting flow in thermal equilibrium.

$$\frac{\partial \rho_s}{\partial t} + \nabla \cdot \left(\rho_s \vec{u} + \vec{J}_s \right) = \dot{w}_s \tag{2.12}$$

$$\frac{\partial \rho \vec{u}}{\partial t} + \nabla \cdot \left(\rho \vec{u} \otimes \vec{u} + p\vec{\vec{I}} - \vec{\vec{\tau}} \right) = 0 \tag{2.13}$$

$$\frac{\partial \mathcal{E}}{\partial t} + \nabla \cdot \left((\mathcal{E} + p) \cdot \vec{u} - \vec{\vec{\tau}} \cdot \vec{u} + \vec{q} + \sum_s \vec{J}_s h_s \right) = 0 \tag{2.14}$$

In the above, ρ_s is the species mass density, and total mixture density is $\rho = \sum_s \rho_s$. The diffusion fluxes for each species are represented by $\vec{J}_s$, and the source term of species mass due to chemical reactions on the right-hand side is $\dot{w}_s$. The average bulk velocity of all species is the vector $\vec{u}$, and pressure, p, is computed using Dalton's law of partial pressures for an ideal gas,

$$p = \sum_s^{NS} \rho_s \frac{R_u}{\mathcal{M}_s} T \tag{2.15}$$

where R_u is the universal gas constant, $\mathcal{M}_s$ is the molecular mass of species s, T is temperature, and NS is the total number of species considered. The identity tensor is given by $\vec{\vec{I}}$. In Eq. (2.13), $\vec{\vec{\tau}}$ is the viscous flux tensor. In the conservation of total energy, $\mathcal{E}$, $\vec{q}$ is the heat flux due to thermal conduction, and h_s is species enthalpy.

For vehicles flying at hypersonic velocities, a bow shock forms around the body where the flow's kinetic energy is converted into several modes of internal energy. These internal modes can be divided into translational, rotational, vibrational, and electronic energy. Under strong nonequilibrium conditions where the flow's residence time is on the same order of magnitude as the characteristic time scales of chemical reactions and thermodynamic relaxation, a single temperature cannot be used to describe them all. As a gas passes through a strong shock, the translational and rotational modes are excited relatively efficiently through collisions and are commonly grouped into one temperature, T_{tr}. However, the vibrational, electronic, and electron translational energy modes need more collisions to reach equilibrium with the translational-rotational mode. Many important chemical reactions, such as the molecular dissociation of nitrogen and oxygen, depend on vibrational energy. The vibrational, electronic, and electron modes of internal energy can be determined from T_{vee}, the vibrational-electronic-electron temperature. This two-temperature model can be included in hypersonic CFD simulations by adding another conservation equation for the vibrational-electronic-electron energy, E_{vee} [73, 74, 75].

$$\frac{\partial \mathcal{E}_{vee}}{\partial t} + \nabla \cdot \left(\mathcal{E}_{vee} \cdot \vec{u} + \vec{q}_{vee} + \sum_s \vec{J}_s e_{vee,s} \right) = \dot{w}_{vee} \tag{2.16}$$

The heat flux of vibrational-electronic-electron energy is q_{vee}, and the vibrational-electronic-electron energy of species s per unit mass is $e_{vee,s}$. Finally, the change of vibrational-electronic-electron energy due to chemical reactions and translational-vibrational relaxation is given by $\dot{w}_{vee}$.

2.2.2 Electromagnetic Equations

The second part for PFE analysis is modeling the electromagnetic fields. PFEs consist of an applied electric field with an applied magnetic field in the transverse direction. Generally, the behavior of electromagnetic fields can be modeled using Maxwell's equations, which are given in differential form below.

$$\nabla \cdot \vec{E} = \frac{q_c}{\epsilon_0} \tag{2.17}$$

$$\nabla \cdot \vec{B} = 0 \tag{2.18}$$

$$\nabla \times \vec{E} = -\frac{\partial \vec{B}}{\partial t} \tag{2.19}$$

$$\nabla \times \vec{B} = \mu_0 \left(\vec{j} + \epsilon_0 \frac{\partial \vec{E}}{\partial t} \right) \tag{2.20}$$

Equation (2.17) is known as Gauss's law and relates the electric field, $\vec{E}$, to the charge density, q_c, where $\epsilon_0 = 8.854 \times 10^{-12}$ F·m^{-1} is the permittivity of free space. Equation (2.18) is Gauss's law for magnetism, which states that no magnetic monopoles exist where $\vec{B}$ is the magnetic field. Equation (2.19) is Faraday's law of induction and Eq. (2.20) is Ampère's circuital law, where $\mu_0 = 1.256 \times 10^{-6}$ N·A^{-2} is the permeability of free space and $\vec{j}$ is the electric current density.

2.2.3 Coupled Magnetohydrodynamic Equations

For an electrically conducting fluid, such as an ionized gas, the governing equations for fluid motion must be modified under the influence of electromagnetic fields. Furthermore, the action of the fluid's motion must be captured in the governing equations for the electromagnetic field. The generalized Ohm's law given in Eq. (2.21) is frequently used to relate current density to the flow of a plasma through a magnetic field.

$$\vec{j} = \sigma \left(\vec{E} + \vec{u} \times \vec{B} \right) \tag{2.21}$$

Equation (2.21) can be used to replace $\vec{j}$ in Ampère's circuital law, assuming the second term on the right-hand-side is small.

$$\nabla \times \vec{B} = \mu_0 \sigma \left(\vec{E} + \vec{u} \times \vec{B} \right) \tag{2.22}$$

The evolution of the magnetic field can be found by rearranging Eq. (2.22) to have an equation for $\vec{E}$ and taking the curl of both sides [76, 4].

$$\frac{\partial \vec{B}}{\partial t} = \nabla \times \left[\vec{u} \times \vec{B} - \frac{\nabla \times \vec{B}}{\mu_0 \sigma} \right] \tag{2.23}$$

The first and second term describe the evolution of the magnetic field as the sum of the induction and the diffusion of the field. The magnetic Reynolds number, given in Eq. (2.24), measures the relative importance of the induced magnetic field to the imposed magnetic field, where u is a characteristic velocity, L is a characteristic length scale, and σ is the electrical conductivity.

$$Re_m = uL\mu_0\sigma \propto \frac{induced\, magnetic\, field}{imposed\, magnetic\, field} \tag{2.24}$$

When the magnetic Reynolds number is small, i.e. $Re_m << 1$, induction is negligible and thus the magnetic induction equation is no longer necessary for describing the magnetic field. Considering a microscopic fluid element with many particles, the Lorentz force law can be rewritten as in Eq. (2.25) to obtain the force per unit volume.

$$\vec{f} = q_c\vec{E} + \vec{j} \times \vec{B} \tag{2.25}$$

The conservation of momentum in Eq. (2.13) can be modified to include the acceleration caused by the electromagnetic fields. The first term in Eq. (2.25) is the electrostatic force, which can be neglected when the flow is quasi-neutral (i.e., $q_c \approx 0$). The second term is the Lorentz force, which occurs when the motion of charged particles is deflected by the magnetic field, thereby delivering kinetic energy to the bulk plasma.

$$\frac{\partial \rho\vec{u}}{\partial t} + \nabla \cdot \left(\rho\vec{u} \otimes \vec{u} + p\vec{\vec{I}} - \vec{\vec{\tau}} \right) = q_c\vec{E} + \vec{j} \times \vec{B} \tag{2.26}$$

Since the electromagnetic forces are doing work on the fluid, the appropriate source term must also be added to the energy balance in Eq. (2.14).

$$\frac{\partial \mathcal{E}}{\partial t} + \nabla \cdot \left((\mathcal{E} + p) \cdot \vec{u} - \vec{\vec{\tau}} \cdot \vec{u} + \vec{q} + \sum_s \vec{J}_s h_s \right) = \vec{j} \cdot \vec{E} \tag{2.27}$$

Physically, as the charged particles move through the fluid in the form of electrical current, they transfer energy to the heavy particles, such as ions and neutrals, through collisions. This mechanism, known as Joule heating, is accounted for in the right-hand-side of Eq. (2.27) by noting that the electrical current can be found using the generalized Ohm's law in Eq. (2.21).

When the charged particles collide with the heavy particles, the energy is transferred to the various internal modes of the gas. For example, in the two-temperature approximation, where translational-rotational energy can be described using T_{tr}, and the vibrational-electronic-electron energy can be described using T_{vee} the amount of energy that is distributed to both modes can be quantified using an energy partitioning constant, η_{vee}. This constant is a scalar that varies from 0 to 1 and appears below in the conservation of vibrational-electronic-electron energy.

$$\frac{\partial \mathcal{E}_{vee}}{\partial t} + \nabla \cdot \left(\mathcal{E}_{vee} \cdot \vec{u} + \vec{q}_{vee} + \sum_s \vec{J}_s e_{vee,s} \right) = \dot{w}_{vee} + \eta_{vee} \vec{j} \cdot \left(\vec{E} + \vec{u} \times \vec{B} \right) \tag{2.28}$$

Note that the generalized Ohm's law in Eq. (2.21) can be rewritten to give the electric field strength in terms of the conductivity, current density, velocity, and magnetic field strength.

$$\vec{E} = \vec{\vec{\sigma}}^{-1} \cdot \vec{j} - \vec{u} \times \vec{B} \tag{2.29}$$

Substituting Eq. (2.29) into the right-hand-side of Eq. (2.28), it can be seen that the electromagnetic energy is deposited into the vibrational mode via Joule heating in addition to the translational mode.

$$\frac{\partial \mathcal{E}_{vee}}{\partial t} + \nabla \cdot \left(\mathcal{E}_{vee} \cdot \vec{u} + \vec{q}_{vee} + \sum_s \vec{J}_s e_{vee,s} \right) = \dot{w}_{vee} + \eta_{vee} \vec{\vec{\sigma}}^{-1} \cdot \vec{j} \cdot \vec{j} \tag{2.30}$$

2.3 LeMANS-MHD

In this work, the nonequilibrium hypersonic CFD code, LeMANS, is used to compute the flow fields inside of PFEs. LeMANS is a multidimensional, parallelized, unstructured, finite-volume code developed primarily for investigating fundamental physical processes around hypersonic vehicles

[67, 77]. However, LeMANS has been previously modified by Bisek to account for MHD effects [68, 1].

The MHD effects are included in the governing equations via source terms and are modeled using the low magnetic Reynolds number assumption in which the induced component of the magnetic field is negligible [45]. Instead, the magnetic field is prescribed and kept constant with respect to time. The conservation equations then can be expressed as follows

$$\frac{\partial \vec{Q}}{\partial t} + \nabla \cdot \left(\vec{\vec{F}} - \vec{\vec{F}}_v \right) = \vec{S} \tag{2.31}$$

where the conserved variables, inviscid and viscous fluxes, and source terms are

$$\vec{Q} = \begin{bmatrix} \rho_1 \\ \cdot \\ \cdot \\ \cdot \\ \rho_{ns} \\ \rho \vec{u} \\ \mathcal{E}_{tot} \\ \mathcal{E}_{vee} \end{bmatrix}, \qquad \vec{\vec{F}} = \begin{bmatrix} \rho_1 \vec{u}^{\intercal} \\ \cdot \\ \cdot \\ \cdot \\ \rho_{ns} \vec{u}^{\intercal} \\ \rho \vec{u} \otimes \vec{u} + p \vec{\vec{I}} \\ (\mathcal{E}_{tot} + p) \vec{u}^{\intercal} \\ \mathcal{E}_{vee} \vec{u}^{\intercal} \end{bmatrix},$$
$$\vec{\vec{F}}_v = \begin{bmatrix} -\vec{J}_1^{\intercal} \\ \cdot \\ \cdot \\ \cdot \\ -\vec{J}_{ns}^{\intercal} \\ \vec{\vec{\tau}} \\ \left(\vec{\vec{\tau}} \cdot \vec{u} \right)^{\intercal} - \vec{q}_{tr}^{\intercal} - \vec{q}_{vee}^{\intercal} - \sum\limits_s \vec{J}_s^{\intercal} h_s \\ -\vec{q}_{vee}^{\intercal} - \sum\limits_s \vec{J}_s^{\intercal} e_{ves,s} \end{bmatrix}, \; \vec{S} = \begin{bmatrix} \dot{w}_1 \\ \cdot \\ \cdot \\ \cdot \\ \dot{w}_{ns} \\ \vec{j} \times \vec{B} \\ \vec{j} \cdot \vec{E} \\ \dot{w}_{vee} + \eta_{vee} \vec{j} \cdot \left(\vec{E} + \vec{u} \times \vec{B} \right) \end{bmatrix} \tag{2.32}$$

Total mixture density can be found by summing across all species densities, i.e. $\rho = \sum_s \rho_s$. Equation (2.15) is modified when the two-temperature model above is used to find an ionized gas's pressure where electrons are present.

$$p = \sum_{s \neq e}^{NS} \rho_s \frac{R_u}{\mathcal{M}_s} T_{tr} + \rho_e \frac{R_u}{\mathcal{M}_e} T_{vee} \tag{2.33}$$

The total energy is the sum of all internal energy modes, the kinetic energy, and species enthalpy of formation,

$$\mathcal{E}_{tot} = \sum_{s \neq e} \rho_s C_{V_{tr,s}} T_{tr} + \frac{1}{2} \rho \left(u^2 + v^2 + w^2\right) + \sum_s \rho_s h_s^\circ + \mathcal{E}_{vee} \tag{2.34}$$

where $C_{V_{tr,s}}$ is the translational specific heat at constant volume, h_s° is the species enthalpy of formation at 0 K, and u, v, and w are the velocity components in the x-, y-, and z-directions. The vibrational-electronic-electron energy can be computed by summing each component of energy for each species where $e_{v,s}$ is the vibrational energy and $e_{el,s}$ is the electronic energy.

$$\mathcal{E}_{vee} = \sum_{s \neq e} \rho_s (e_{v,s} + e_{el,s}) + \frac{3}{2} \frac{R_u}{\mathcal{M}_e} T_{vee} \tag{2.35}$$

LeMANS employs a second-order finite volume discretization in space and integrates the above governing equations in time using either an explicit, point implicit, or line implicit scheme. The numerical fluxes are calculated using a Steger-Warming Flux Vector Splitting scheme. LeMANS uses the mesh partitioning software METIS to divide the computational domain across multiple central processing units (CPUs) [78]. Then, flowfield data is passed between CPUs using the Message Passage Interface (MPI) communication protocol to leverage the parallel computational performance of state-of-the-art HPC systems. Several validation studies have been performed with LeMANS [77].

2.3.1 Source Terms

The nonequilibrium and electromagnetic phenomena that occur in high-speed, MHD augmented flows are captured in the governing equations via the source terms in Eq. (2.32). Namely, the chemical reaction source terms in the species conservation equations, the Lorentz force in the momentum equations, the electromagnetic deposition term in the energy equations, and the thermochemical source terms in the vibrational-electronic-electron energy equation encapsulate all those effects. The following sections will describe how each process is modeled and LeMANS-MHD, but the specific implementation details can be found in Refs. [67, 68].

2.3.1.1 Thermochemical Source Terms

First, chemical reactions are modeled using a finite-rate chemistry model for any gas mixture. Generally, these reactions include dissociation and association, ionization and recombination, and various exchange processes. The following equation can describe all reactions,

$$\sum_s \nu'_s[S] \rightleftharpoons \sum_s \nu''_s[S] \tag{2.36}$$

where ν'_s and ν''_s are stoichiometric coefficients and $[S]$ is the concentration of some species s. The following equation describes the source terms for each species' mass production/destruction rate due to a single reaction r.

$$\dot{w}_{sr} = (\nu''_{sr} - \nu'_{sr}) \left[k_{fr} \prod_j \left(\frac{\rho_j}{\mathcal{M}_j} \right)^{\nu'_{jr}} - k_{br} \prod_j \left(\frac{\rho_j}{\mathcal{M}_j} \right)^{\nu''_{jr}} \right] \tag{2.37}$$

The total source term for each species is calculated by summing the reaction-specific rate across all reactions.

$$\dot{w}_s = \mathcal{M}_s \sum_r \dot{w}_{sr} \tag{2.38}$$

The forward and backward reaction rates in Eq. (2.37) are usually pulled from the vast chemical kinetic literature for the relevant mixtures and conditions. Typically, these rates are provided as Arrhenius curve fits using a controlling temperature, T_c.

$$k_{fr} = C_{fr} T_c^{\eta_r} \exp(-\theta_r / T_c) \tag{2.39}$$

In the hypersonic community, Park's two-temperature model is commonly used to compute the reaction rate under thermodynamic nonequilibrium [79]. However, more recently, improved models have been developed using *ab-initio* quantum chemistry data to account for the preferential dissociation of highly excited molecules in 5 species air mixtures [80, 81]. Regardless, the forward rates are typically computed using some combination of T_{tr} and T_{vee}.

The backward reaction rates can be computed for some processes once the forward rates are known using the equilibrium constant, K_{eq} at a separate controlling temperature $T_{c,b}$.

$$k_{br} = \frac{k_{br}(T_{c,b})}{K_{eq}(T_{c,b})} \tag{2.40}$$

The equilibrium constants can be found either via curve fits in Ref. [11] or minimizing Gibb's free energy.

Finally, the source of vibrational-electronic-electron energy due to various nonequilibrium effects can be represented by $\dot{w}_{vee}$.

$$\begin{aligned} \dot{w}_{vee} = -p_e \nabla \cdot \vec{u} + \sum_s \dot{w}_s (D'_s + e_{el,s}) + \frac{\rho C_{V_{vee}}}{\tau}(T - T_{vee}) \\ +3R_u \rho_e (T - T_{vee}) \sqrt{\frac{8 R_u T_{vee}}{\pi \mathcal{M}_e}} \sum_{r \neq e} \frac{\rho_r N_A}{\mathcal{M}_r^2} \sigma_{er} + \sum_{s=ions} \mathcal{M}_s \dot{w}_s \hat{I}_s \end{aligned} \tag{2.41}$$

The terms in Eq. (2.41) are from left to right: work done on electrons by the electron pressure gradient, the change in vibrational-electronic-electron energy due to reactions, the relaxation between the translational-rotational and vibrational-electronic-electron modes, the energy exchange between heavy particles and electrons, and the energy removed from free electrons from impact ionization reactions. D'_s is the energy lost due to dissociation and is typically some fraction of the average vibrational energy. τ is the mixture relaxation time given by Park [11]. σ_{er} is the collision cross section between electrons and heavy particles, and $\hat{I}_s$ is set to 1/3 of the first ionization energy.

2.3.1.2 Electromagnetic Source Terms

To find the Lorentz force, $\vec{j} \times \vec{B}$, and the total energy deposition term, $\vec{j} \cdot \vec{E}$, the current density, magnetic field, and electric field must be determined. The low magnetic Reynolds number assumption is assumed to be valid in the PFE, so the magnetic field is prescribed throughout the entire domain [45].

Starting from the generalized Ohm's law in Eq. (2.21), Amperè's circuital law in Eq. (2.20) can be used under the assumption that the displacement current term is negligible relative to the conduction current, i.e.

$$\nabla \times \vec{B} = \mu_0 \vec{j}. \tag{2.42}$$

By taking the divergence of both sides of Eq. (2.42) and noting that the divergence of the curl of any quantity is zero, it is observed that the divergence of current density is zero everywhere.

$$\nabla \cdot \vec{j} = 0 \tag{2.43}$$

Additionally, Faraday's law of induction can be used to note that the curl of the electric field is zero when the applied magnetic field strength is constant in time, i.e.

$$\nabla \times \vec{E} = \vec{0}. \tag{2.44}$$

The Helmholtz decomposition of the electric field separates the field into two components. The first term is the irrotational vector field, which can be described using the electric potential scalar, ϕ. The second term is the divergence-free field, described using a vector potential $\vec{A}$.

$$\vec{E} = -\nabla\phi + \nabla \times \vec{A} \tag{2.45}$$

However, since the electric field is irrotational due to Eq. (2.44), the second term in Eq. (2.45) must also be zero since the curl of the gradient of any quantity is always zero. Therefore, the electric field is simply the gradient of the electric potential, ϕ.

$$\vec{E} = -\nabla\phi \tag{2.46}$$

By taking the divergence of Eq. (2.21) and noting that the right-hand side must be equal to zero due to Eq. (2.43), and substituting Eq.(2.46) in for the electric field vector, the following equation can be solved to find the electric field potential everywhere in the domain.

$$\nabla \cdot \left[\vec{\vec{\sigma}} \cdot \left(-\nabla\phi + \vec{u} \times \vec{B}\right)\right] = 0 \tag{2.47}$$

In LeMANS-MHD, the main Navier-Stokes solver solves for the bulk flow velocity, $\vec{u}$, while the magnetic field strength $\vec{B}$ is prescribed everywhere in the domain during initialization. The electrical conductivity is typically solved as a function of flow field quantities, such as plasma density and temperature. However, it can also be a function of the electric field strength itself. Once the electric potential is known, the electric field strength is computed using Eq. (2.46), and the current density is found using the generalized Ohm's law in Eq. (2.21). Equation (2.46) is solved via a second-order Finite Volume scheme for each cell in the domain. As such, to improve computational efficiency, the electric potential is not solved for and updated every iteration. Instead, it is solved every N iterations where N is some positive integer chosen by the user.

2.3.2 Transport Properties

Transport property coefficients are needed to calculate the viscous stresses. Namely, diffusion coefficients for mass diffusion in the conservation of mass equations, viscosity is needed for the viscous fluxes, thermal conductivity for the heat fluxes, and electrical conductivity is needed for the Ohm's law calculation.

2.3.2.1 Mass Diffusion Fluxes

Mass diffusion is calculated using modified Fick's law, where D_s is the diffusion coefficient, and Y_s is the mass concentration [82].

$$\vec{J}_{s\neq e} = -D_s\rho_s\nabla Y_s - Y_s\sum_{r\neq e} -\rho D_r\nabla Y_r \tag{2.48}$$

The second term in Eq. (2.48) is needed to ensure the sum of all fluxes sums to zero. To ensure ambipolar diffusion, where positive ions and electrons diffuse together, the electron diffusion flux is calculated using Eq. (2.49).

$$\vec{J}_e = -\frac{1}{q_e}\sum_{s\neq e} q_s\vec{J}_s \tag{2.49}$$

2.3.2.2 Viscous Fluxes

The viscous fluxes are found assuming a Newtonian fluid and using Stokes' hypothesis, where μ is the mixture viscosity.

$$\vec{\vec{\tau}} = \mu\left(\nabla\vec{u} + (\nabla\vec{u}^{\intercal})\right) - \frac{2}{3}\mu\left(\nabla\cdot\vec{u}\right)\vec{\vec{I}} \tag{2.50}$$

The viscosity coefficients for air species are commonly computed for hypersonic flows using a curve fit due to Blottner, as given below, where A_s, B_s, and C_s are constants for each separate species [83].

$$\mu_s = 0.1\exp\left[(A_s\ln(T_{tr}) + B_s)\ln(T_{tr}) + C_s\right] \tag{2.51}$$

Since most gases of practical interest are mixtures, a mixing rule is needed to average the species' viscosity coefficients into a bulk viscosity coefficient. Wilke's mixing rule is commonly employed alongside Blottner's viscosity model [84].

$$\mu = \sum_s \frac{X_s\mu_s}{\phi_s} \tag{2.52}$$

where X_s is the molar fraction of species s, and the scaling factor is

$$\phi_s = \sum_r X_r\left[1 + \sqrt{\frac{\mu_s}{\mu_r}}\left(\frac{\mathcal{M}_r}{\mathcal{M}_s}\right)^{1/4}\right]^2\left[\sqrt{8\left(1 + \frac{\mathcal{M}_s}{\mathcal{M}_r}\right)}\right]^{-1} \tag{2.53}$$

The Wilke/Blottner formulation for viscosity works well for hypersonic conditions where the maximum temperature remains less than 10,000 K [85, 86, 87]. Conversely, another model for viscosity by Gupta was explicitly developed for weakly ionized flows that occur for higher speed flows. Under this model, viscosity is calculated as

$$\mu = \sum_{s \neq e} \frac{m_s \gamma_s}{\sum_{r \neq e} \gamma_r \Delta^{(2)}_{s,r}(T_{tr}) + \gamma_e \Delta^{(2)}_{s,e}(T_{vee})} + \frac{m_e \gamma_e}{\sum_r \gamma_r \Delta^{(2)}_{e,r}(T_{vee})} \tag{2.54}$$

where $\Delta_{s,r}$ are collision terms evalutated at temperature T_{tr} or T_{vee}, and γ_s is the molar concentration of species, s [88].

$$\gamma_s = \frac{\rho_s}{\rho \mathcal{M}_s} \tag{2.55}$$

The collision terms are calculated as

$$\begin{aligned} \Delta^{(1)}_{s,r} &= \frac{8}{3}\left[\frac{2\mathcal{M}_s\mathcal{M}_r}{\pi R T(\mathcal{M}_s + \mathcal{M}_r)}\right]^{(1/2)} \pi\bar{\Omega}^{(1,1)}_{s,r} \\ \Delta^{(2)}_{s,r} &= \frac{16}{5}\left[\frac{2\mathcal{M}_s\mathcal{M}_r}{\pi R T(\mathcal{M}_s + \mathcal{M}_r)}\right]^{(1/2)} \pi\bar{\Omega}^{(2,2)}_{s,r} \end{aligned} \tag{2.56}$$

where $\pi\bar{\Omega}^{(1,1)}_{s,r}$ and $\pi\bar{\Omega}^{(2,2)}_{s,r}$ are collision integrals that depend on the species of the particles interacting [88, 89].

2.3.2.3 Thermal Conduction Fluxes

In the two-temperature model, the translational-rotational and vibrational-electronic-electron heat fluxes are both given by Fourier's law of heat conduction, where the mixture thermal conductivity is given by κ_{tr} for the former and κ_{vee} for the latter.

$$\vec{q}_{tr,vee} = -\kappa_{tr,vee} \nabla T_{tr,vee} \tag{2.57}$$

Similar to Eq. (2.52), mixture thermal conductivity can be calculated from the individual species' thermal conductivities and Wilke's mixing rule, where the scaling factor, ϕ_s, is defined in Eq. (2.53) [84].

$$\kappa = \sum_s \frac{X_s \kappa_s}{\phi_s} \tag{2.58}$$

Each mode's individual species' thermal conductivities are calculated using Eucken's relation [70].

$$\begin{aligned} \kappa_{tr,s} &= \frac{5}{2}\mu_s C_{V_{t,s}} + \mu_s C_{V_{r,s}} \\ \kappa_{vee,s} &= \mu_s C_{V_{vee,s}} \end{aligned} \tag{2.59}$$

In conjunction with the Wilke/Blottner model above, Eucken's relation for the thermal conductivities is usually employed and denoted as the Wilke/Blottner/Eucken formulation. Alternatively, Gupta also provides models for the thermal conductivities, which are given below for the translational, rotational, vibrational-electronic, and electron modes, where $k_B = 1.38 \times 10^{-23}$ J/K is the Boltzmann constant [88].

$$\kappa_t = \frac{15}{4} k_B \sum_{s \neq e} \gamma_s \left[\sum_{r \neq e} a_{s,r} \gamma_r \Delta^{(2)}_{s,r}(T_{tr}) + 3.54 \gamma_e \Delta^{(2)}_{s,e}(T_{vee}) \right]^{-1} \tag{2.60}$$

$$\kappa_r = k_B \sum_{s=mol} \gamma_s \left[\sum_{r \neq e} \gamma_r \Delta^{(1)}_{s,r}(T_{tr}) + \gamma_e \Delta^{(1)}_{s,e}(T_{vee}) \right]^{-1} \tag{2.61}$$

$$\kappa_{ve} = k_B \frac{C_{V_{ve}}}{R} \sum_{s=mol} \gamma_s \left[\sum_{r \neq e} \gamma_r \Delta^{(1)}_{s,r}(T_{tr}) + \gamma_e \Delta^{(1)}_{s,e}(T_{vee}) \right]^{-1} \tag{2.62}$$

$$\kappa_e = \frac{15}{4} k_B \gamma_e \left[\sum_r 1.45 \gamma_r \Delta^{(2)}_{e,r}(T_{vee}) \right]^{-1} \tag{2.63}$$

In Eq. (2.60), $a_{s,r}$ is defined by the following equation

$$a_{s,r} = 1 + \frac{[1 - (m_s/m_r)][0.45 - 2.54(m_s/m_r)]}{[1 + (m_s/m_r)]^2}. \tag{2.64}$$

2.3.2.4 Coefficients of Mass Diffusion

In the absence of collision cross-section data, the diffusion coefficients in Eq. (2.48) for the Wilke/Blottner/Eucken formulation can be defined using the Lewis number, Le, and the coefficient of thermal conductivity for the mixture. Instead of species-specific diffusion coefficients, an average mixture coefficient is defined using the weighted average in Eq. (2.58).

$$D = \frac{\kappa_{tr} Le}{\rho C_{P_{tr}}} \tag{2.65}$$

Using the collision cross-section data and Gupta's model, the binary coefficient for one species s, diffusing into another r, can be calculated using the following equation.

$$D_{s,r} = \frac{k_B T_{tr}}{p \Delta^{(1)}_{s,r}(T_{tr})} \tag{2.66}$$

Likewise, the diffusion coefficient for electrons can be calculated using T_{vee} and the electron-specific collision term $\Delta_{e,r}$.

$$D_{e,r} = \frac{k_B T_{vee}}{p \Delta^{(1)}_{e,r}(T_{vee})} \tag{2.67}$$

The species-specific diffusion coefficient can be defined by assuming the mixture comprises one species s, and all other species are lumped into a separate second species.

$$D_s = (1 - X_s) \left(\sum_{r \neq s,e} \frac{X_r}{D_{s,r}} \right)^{-1} \tag{2.68}$$

2.3.2.5 Electrical Conductivity

Finally, a physical model for the electrical conductivity tensor, $\vec{\vec{\sigma}}$, is needed. Accurately modeling the electrical conductivity is critical to the success of simulating MHD augmented systems. Electrical conductivity directly controls the magnitude of the rate of momentum transfer to the plasma by the applied electromagnetic fields and the total heating. In addition, the Hall and ion slip effects can also be described by the electrical conductivity tensor [90, 91].

$$\vec{\vec{\sigma}} = \frac{\sigma}{B^2(1+\beta^2)} \begin{bmatrix} B^2+\beta^2 B_x^2 & \beta(\beta B_x B_y - B B_z) & \beta(\beta B_x B_z + B B_y) \\ \beta(\beta B_y B_x + B B_z) & B^2+\beta^2 B_y^2 & \beta(\beta B_y B_z - B B_x) \\ \beta(\beta B_z B_x - B B_y) & \beta(\beta B_z B_y + B B_x) & B^2+\beta^2 B_z^2 \end{bmatrix} \tag{2.69}$$

In Eq. (2.69), B is the magnetic field magnitude, and β_s is the Hall parameter defined in Eq. (2.4). Noting that this equation for mobility can be rewritten for a plasma with only singly charged ions as

$$\mu_s = \frac{q_e}{m_s v_{sH}} \tag{2.70}$$

and scalar conductivity can be defined as

$$\sigma = \sum_s \frac{q_e^2 n_s}{m_s v_{eH}} \tag{2.71}$$

By combining these two equations, the conductivity can be found in terms of mobility using Eq. (2.72).

$$\sigma = \sum_s \mu_s q_e n_s. \tag{2.72}$$

By comparing Eqs. (2.69), (2.4), and (2.72), it is clear that the tensor conductivity can be found once electrical mobility has been modeled. Consider an electric field applied in the z-direction, with a magnetic field in the y-direction and flow velocity in the x-direction. Ignoring ion slip [4], generalized Ohm's law can be decomposed into each of its three components. Due to the Hall effect, the overall electron current will be in the x- and z-directions.

$$\begin{aligned} j_x &= \frac{\sigma_e \beta_e}{1+\beta_e^2}(E_z - uB_y) \\ j_z &= \frac{\sigma_e}{1+\beta_e^2}(E_z - uB_y) \end{aligned} \tag{2.73}$$

Note that the Hall effect has two impacts on the total current density. The first is that the x-component, which is parallel to the flow velocity, will be greater than the z-component, which is in the electric field direction, when $\beta > 1$. The second is that the total conductivity will be reduced by a factor of $1 + \beta_e^2$. To visualize the magnitude of this effect, Fig. 2.3 illustrates the electron current density versus the electron Hall parameter.

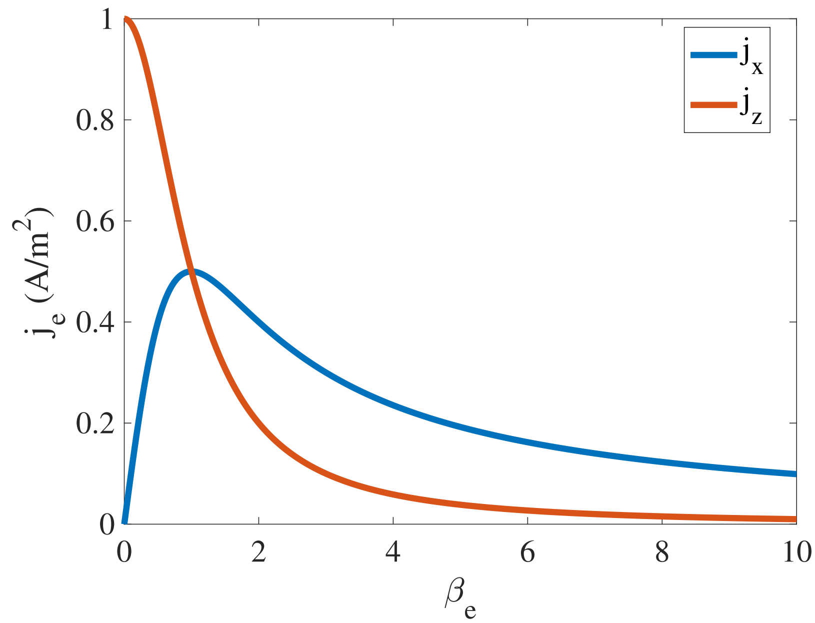

Figure 2.3: **Component-wise current density versus electron Hall parameter.**

For very low Hall parameters, $\beta_e << 1$, the current is primarily in the electric field direction. However, this component quickly decreases, and the flow-direction component increases until they are equal in magnitude at $\beta_e = 1$. Then as the Hall parameter is further increased, both components decrease due to the $1 + \beta_e^2$ scaling. Thus, it is imperative to have an accurate prediction for the electron Hall parameter before simulations can take place as the mode of acceleration is very sensitive to its magnitude.

2.4 One-Dimensional PFE Model

As part of this work, three-dimensional simulations of basic PFE configurations are performed using LeMANS-MHD. However, due to the complicated nature of these flows and the large computational resources needed to perform a single three-dimensional simulation, a simplified one-dimensional model has been developed. This one-dimensional model, written in MATLAB, is able to provide valuable insight into the fundamental physical processes present in the PFE and can be run on a desktop computer on the order of minutes as opposed to days. This model can quickly predict engine performance parameters, which in turn will guide future three-dimensional simulations in the design of PFE prototypes.

Other one-dimensional analyses have been performed for various MHD thruster applications, as in Refs. [92, 24, 39, 50, 93, 53]. The model outlined in this section will facilitate similar analyses for low-density, hypersonic MHD accelerators such as the PFE. Assumptions are made such as that the magnetic Reynolds number is low enough to couple the fluid equations with the electromagnetic field through the appropriate source terms. Additionally, viscous effects are neglected and the plasma is considered quasineutral throughout the entire domain.

A one-dimensional model can be used to investigate the fundamental characteristics of an MHD accelerator such as the PFE. In this model, the axial direction is the only spatial direction that is considered. However, the cross-sectional area of the channel is allowed to vary as a function of axial distance. The MHD source terms to the governing equations are modeled using the low magnetic Reynolds number assumption in which there is no induced component of the magnetic field [45]. Instead, it is prescribed and kept constant with respect to time.

$$\frac{\partial \rho_s}{\partial t} + \frac{\partial}{\partial x}(\rho_s u) = \dot{w}_s - \frac{\rho_s u}{A}\frac{\partial A}{\partial x} \tag{2.74}$$

$$\frac{\partial \rho u}{\partial t} + \frac{\partial}{\partial x}(\rho u^2 + p) = jB - \frac{\rho u^2}{A}\frac{\partial A}{\partial x} \tag{2.75}$$

$$\frac{\partial \mathcal{E}}{\partial t} + \frac{\partial}{\partial x}\left((\mathcal{E} + p)u\right) = jE - \frac{u(\mathcal{E} + p)}{A}\frac{\partial A}{\partial x} \tag{2.76}$$

$$j = \sigma(E - uB) \tag{2.77}$$

Equation (2.74) describes the conservation of mass where ρ_s is the mass density of species s. Next, Eq. (2.75) is the conservation of momentum in the axial direction with the Lorentz force on the right hand side. Finally, Eq. (2.76) is the conservation of total energy with a total energy deposition term due to the electric field on the right hand side. The last term in Eqs. (2.74-2.76) represent the source terms due to the change in cross-sectional area. The current density in the source terms for both the momentum and energy equations is calculated via the generalized Ohm's law in Eq. (2.77). This work implicitly assumes that the applied electric and magnetic fields are in the direction that generates a corresponding Lorentz force in the flow's direction. Correspondingly, the electric field and resulting current density are applied in the z-direction (or y-direction), and the magnetic field is assumed to be solely in the y-direction (or z-direction).

First-order numerical fluxes are chosen to solve the one-dimensional equations because of their simplicity and robustness and the fact that solution convergence can be achieved using very fine computational meshes in the one-dimensional setting. A first-order forward or backward Euler method marches the solution forward in the time domain. It is important to note here the treatment of the boundary conditions at the inlet and outlet of the domain. Total temperature and mass flux are used to define the boundary conditions at the inlet for subsonic conditions since these quantities are conserved over a normal shock. Otherwise, the inlet is set based on freestream conditions of the flow. If the flow is subsonic at the outlet, then the freestream pressure is set at the boundary. However, if the flow is supersonic at the outlet, a zero-flux boundary condition is set such that no information propagates back into the domain.

2.4.1 Numerical Accuracy of One-Dimensional Solver

The accuracy of the numerical solver is tested by comparing numerical solutions in the velocity versus Mach number plane to exact solutions given in Ref. [5]. The relationship between Mach number and velocity for a constant area, constant electric field, and constant magnetic field channel is given in Eq. (19) of that paper. It is reproduced below in Eq. (2.78). The constant, c, determines where in velocity versus Mach number space the solution exists. Velocities from the numerical solver are used to compute the Mach number using Eq. (2.78), and those values are compared to Mach numbers computed by the 1D model.

$$M^2 = \frac{\frac{u}{u_3}\left(\frac{u}{u_1} - 1\right)}{c + (\gamma - 1)\frac{u}{u_1}\left(1 - \frac{u}{2u_3}\right)} \tag{2.78}$$

To compare the Mach numbers directly, c is chosen such that the inlet Mach number and velocity satisfy Eq. (2.78). For Mach 10 flight at 50 km freestream conditions that undergoes deceleration through two oblique shock waves, the inlet velocity and Mach number are approximately 2900 m/s and 4.95, respectively. Therefore, c equals -0.6763, and errors between the numerical and exact solutions are computed on three different grids using Eq. (2.79).

$$error = \sqrt{\frac{1}{\#ofcells}\sum\left(M_{exact} - M_{num}\right)^2} \tag{2.79}$$

The numerical errors for grids with 100, 500, and 1000 cells are shown in Fig. 2.4. Additionally, a first-order slope is provided to compare the convergence to the nominal rate. By comparing the numerical error as the mesh is refined to the first-order slope provided, it is concluded that the one-dimensional model is achieving the expected rate of convergence.

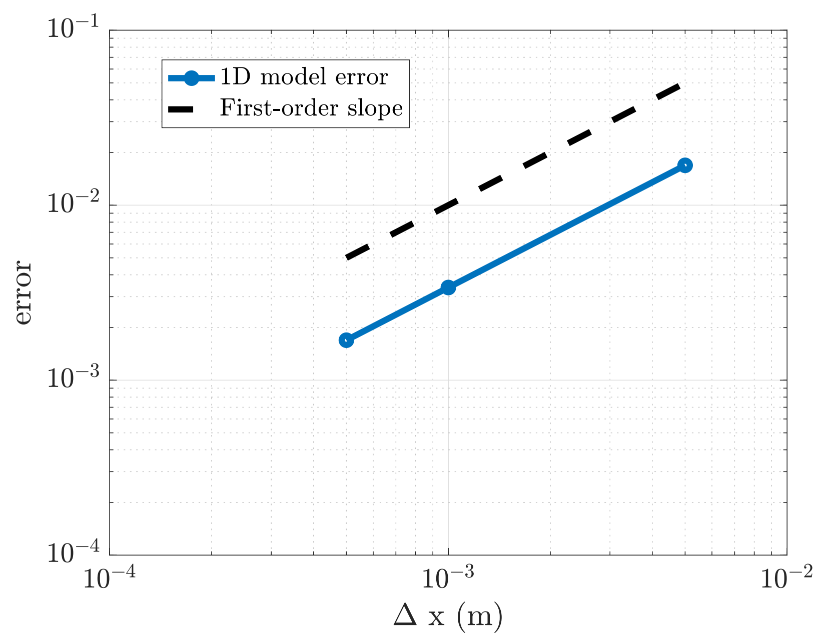

Figure 2.4: **Numerical error versus grid refinement of one-dimensional model.**

2.5 Summary

In conclusion, this chapter has provided a brief summary of the behavior of charged particles subject to crossed electromagnetic fields. Furthermore, some of the fundamental plasma properties that are required for successful numerical simulation were identified. Namely, definitions for mobility, Hall parameter, ionization rate, and mean electron energy were given. Then the relevant governing equations of fluid dynamics, electromagnetics, and ultimately magnetohydrodynamics were provided. The three-dimensional nonequilibrium hypersonic code that will be used in this work to solve the governing equations, LeMANS-MHD, and some of the necessary physical models therein were detailed. Finally, a one-dimensional model was presented to aid in the guidance of three-dimensional simulations as well as to provide design insights of future PFE prototypes. The remaining chapters will define the requirements for successful PFE operation as well as use these computational tools to perform both one-dimensional and multi-dimensional simulations.

Chapter 3

Operating Envelope and Physical Constraints of Hypersonic MHD Accelerators

Chapter 2 introduced fundamental physical processes for partially ionized hypersonic plasmas and the mathematical models necessary to capture them in numerical simulations. Then, the physical models used in this work to analyze MHD accelerated hypersonic channel flows were described alongside two numerical tools for solving the governing equations. Namely, the three-dimensional CFD code with a generalized Ohm's law solver, LeMANS-MHD, was described as well as a one-dimensional model that neglects viscous effects. The simplified one-dimensional model allows users to simulate a wide range of flight regimes and operating conditions in minutes. However, the one-dimensional treatment cannot capture several multi-dimensional effects inherent to magnetized plasmas flowing through channels. Instead, those effects, such as viscous interactions near walls and the Hall effect, can only be understood in a two-dimensional and three-dimensional context. LeMANS-MHD is necessary for fully understanding how these systems behave.

However, before simulations can be performed using these numerical tools, describing the operating regimes in which the PFE may be successful and highlighting the physical limitations is essential. Without equivalent wind tunnel test data and flight data, this discussion will be used to develop intuition and reinforce confidence in the numerical models.

This chapter will outline the theoretical MHD accelerator theory and how it applies to developing efficient PFE designs. Furthermore, this discussion will define the physical requirements the PFE configurations must achieve to arrive at practical thrust generation. Much of this theory has been described in the pioneering works in Refs. [5, 44, 42], but very illustrative descriptions can also be found in Refs. [4, 16]. However, the following will focus on concepts for hypersonic vehicles flying through Earth's atmosphere. As such, the MHD accelerator theory will be extended to the physical conditions relevant to the PFE. Of foremost concern in designing MHD accelerators operating at high altitudes is the collisionality of the plasma. As the vehicle climbs in altitude, plasma collisions become more infrequent, changing how energy is transferred between the electromagnetic fields and the bulk plasma.

When much of the MHD accelerator theory was derived, many assumptions had to be in place to find analytical solutions. Many clever mathematical treatments were performed but for limited conditions where both flow field variables and electromagnetic fields were held constant. With the advantage of modern computational power, these assumptions can be lifted to arrive at more complicated solutions with increased physical fidelity. This chapter will employ first-principles analysis to compute charged particle gyrofrequencies and collision frequencies to arrive at first-order estimates of critical quantities such as the Hall parameter and required electric field strengths.

3.1 Operating Regime for a Hypersonic MHD Accelerator

In classical compressible gas dynamics theory, it is well known that flow through a duct can be accelerated or decelerated by the appropriate manipulation of the cross-sectional area or heat addition to the flow. For example, one can derive the area-velocity relation from the quasi-one-dimensional equations of isentropic flow, where A is the area of the duct, M is the Mach number, and u is the velocity [94].

$$\frac{dA}{A} = (M^2 - 1)\frac{du}{u} \tag{3.1}$$

This relation states that flow in a nozzle ($dA < 0$) will be accelerated if subsonic and decelerated if supersonic. Conversely, flow in a diffuser ($dA > 0$) will be decelerated if subsonic and accelerated if supersonic. Furthermore, the Mach number can be related to the area of the duct via the area-Mach number relation, where A^* is the area at the throat where $M = 1$, and γ is the ratio of specific heats.

$$\left(\frac{A}{A^*}\right)^2 = \frac{1}{M^2}\left[\frac{2}{\gamma+1}\left(1+\frac{\gamma-1}{2}M^2\right)\right]^{(\gamma+1)/(\gamma-1)} \tag{3.2}$$

These elementary equations of gas dynamics can be extended to encapsulate the effects of electromagnetic forcing. Thus, a third mechanism in which flow through a duct can be modified is introduced. In 1964, Culick found solutions to the one-dimensional and quasi-one-dimensional equations for inviscid flow through a channel with Lorentz force acceleration under steady-state conditions [5]. This analysis also assumed that the magnetic Reynolds number was much less than unity and that a scalar, σ, could represent electrical conductivity. Resler and Sears adopted the conventions used in classical compressible gas dynamics to rewrite the velocity-area relation for flows under the influence of electromagnetic fields [42],

$$\frac{1}{u}\frac{du}{dx} = \frac{1}{M^2-1}\left[\frac{1}{A}\frac{dA}{dx} - \frac{\sigma B^2}{up}(u-u_1)(u-u_3)\right], \tag{3.3}$$

where σ is the electrical conductivity, B is the magnetic field strength, and p is pressure. Assuming an electric field E, the characteristic velocities u_1 and u_3 are given by

$$u_1 = \frac{(\gamma-1)E}{\gamma B}, \tag{3.4}$$

$$u_3 = \frac{E}{B}. \tag{3.5}$$

Similarly, a Mach number-area relation can be derived for channel flows with a crossed electromagnetic field.

$$\frac{1}{M}\frac{dM}{dx} = \frac{1+\frac{1}{2}(\gamma-1)M^2}{M^2-1}\left[\frac{1}{A}\frac{dA}{dx} - \frac{\sigma B^2}{up}(u-u_2)(u-u_3)\right] \tag{3.6}$$

where the characteristic velocity, u_2, is given by

$$u_2 = \frac{(1+\gamma M^2)u_1}{2+(\gamma-1)M^2}. \tag{3.7}$$

Equations (3.3) and (3.6) are very convenient because they describe the evolution of velocity and Mach number as a function of axial distance, x for a given electric and magnetic field strength. However, the performance of any MHD energy converter can be easily understood in velocity-Mach number space. The variation of velocity versus Mach number highlights the balance between heating and acceleration in these devices through the following relation, where c is a constant that determines the curve in velocity-Mach number space in which the solution develops.

$$\frac{u}{M}\frac{dM}{du} = \left[1 + \frac{u_1}{2u}\frac{u}{A}\frac{dA}{du} + \frac{\gamma - 1}{2}M^2\right]\frac{u - u_3}{u - u_1} \tag{3.8}$$

Equation (3.8) can be integrated to yield the permissible solutions for variable area channels. The velocity-Mach relation can be further simplified by considering constant area cases where the electric field and magnetic field are prescribed and held constant.

$$M^2 = \frac{\frac{u}{u_3}\left(\frac{u}{u_1} - 1\right)}{c + (\gamma - 1)\frac{u}{u_1}\left(1 - \frac{u}{2u_3}\right)} \tag{3.9}$$

These one-dimensional solutions were then used to develop several informative figures, such as the one reproduced in Fig. 3.1, which displays how a constant area MHD accelerator with a constant electromagnetic field will perform for any combination of inlet velocity and Mach number [5]. The inlet conditions to the channel dictate the starting position in velocity versus Mach number space on this plot. The second law of thermodynamics governs which direction the solution moves with respect to axial distance, as indicated by the arrows.

There are several regions in this diagram that predetermine how the flow will develop as a function of the inlet Mach number, velocity, electric field strength, and magnetic field strength. Any region where the arrows point in the positive u/u_3 direction indicate MHD accelerator configurations, whereas the arrows that point in the negative direction indicate MHD generator configurations. The dashed lines each have their own significance. For example. the velocity at which a subsonic gas accelerates through Mach 1 is u_1, where u_3 is the velocity in which the electric field generated by the motion of the plasma through the magnetic field is equal to the applied electric

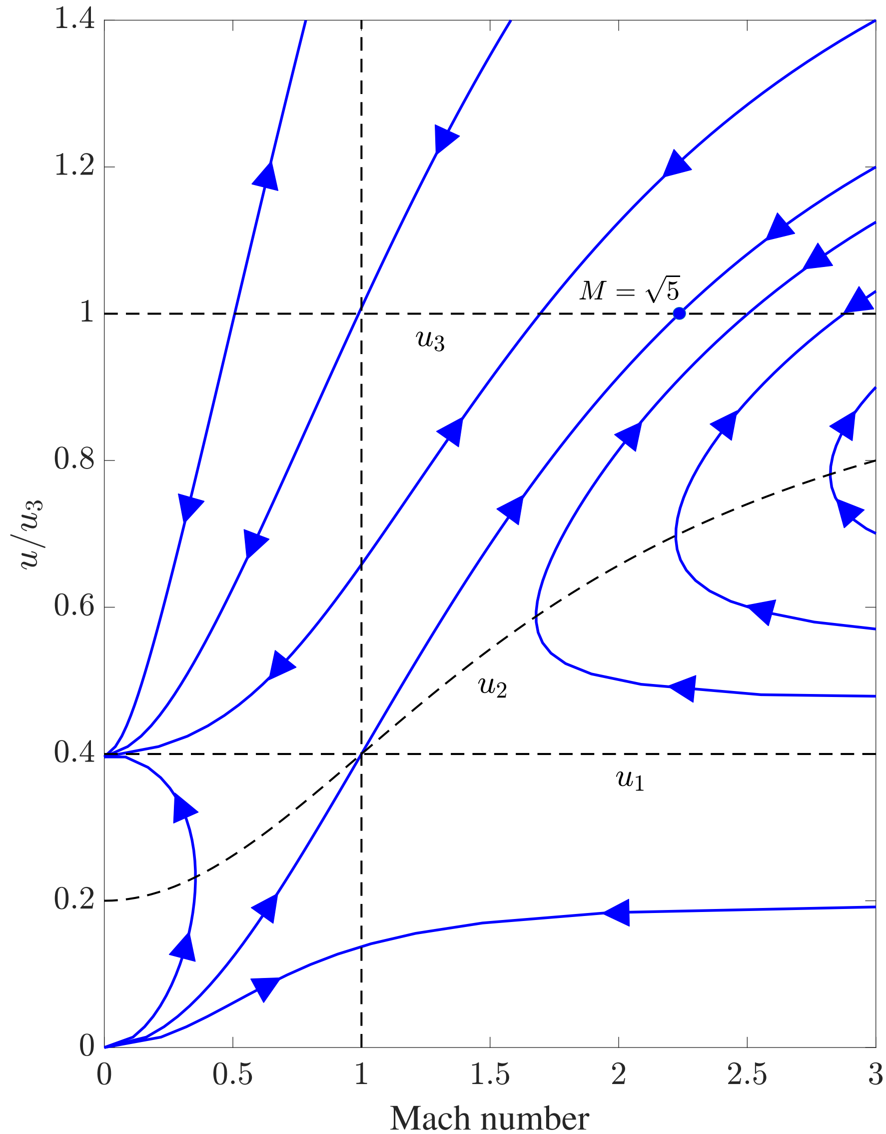

Figure 3.1: **Culick's velocity-Mach number diagram for a constant area channel with constant $\boldsymbol{E}$ and $\boldsymbol{B}$ fields [5].**

field. When this occurs, the plasma no longer experiences the Lorentz body force. For a monatomic gas such as argon, $u_1 = 0.4u_3$. The dashed vertical line in Fig. 3.1 represents Mach 1, so everything to the left of this line is subsonic, and everything to the right is supersonic. The inverse of the ratio u/u_3 is commonly known as the load factor.

For a plasma with a high enough freestream Mach number, the electromagnetic field will need to be chosen so that the plasma does not decelerate down the length of the channel. Deceleration occurs if the applied electric field is too large or too small for a given inlet velocity, Mach number, and magnetic field strength. Instead, tuning the electromagnetic field so that the Lorentz force accelerates the plasma to the desired exit velocity for different combinations of inlet conditions is necessary.

With the appropriate electromagnetic fields, a flow can accelerate from subsonic at the inlet to $M = \sqrt{5}$ downstream, indicated in Fig. 3.1 by the curve that begins in the bottom left region, travels through Mach 1 at $u/u_3 = 0.4$, and accelerates to Mach $\sqrt{5}$ at $u/u_3 = 1$. However, for a supersonic flow at the inlet, the characteristic velocity u_1 demarcates the electromagnetic field selection in which a flow either decelerates or accelerates with axial distance. Thus, the applied electric field cannot be arbitrarily high to achieve acceleration. For a fixed magnetic field strength, the electric field must be chosen such that u_1 is not greater than the inlet velocity.

Similarly, the applied electric field strength must be larger than the field generated by the motion of the plasma through a magnetic field, or the Lorentz force will oppose the oncoming flow. In that case, where the electromagnetic field selection causes the characteristic velocity u_3 to be less than the inlet velocity, the MHD channel would act as an MHD generator wherein the system converts the flow's kinetic energy into electrical power.

Since the PFE is intended for hypersonic flow regimes, the left side of the plot, where the flow is either partially or entirely subsonic, will not be considered for design of PFEs. The region of interest for MHD acceleration of supersonic flows is bounded by the Mach 1 line on the left and the characteristic velocities u_1 and u_3 at the bottom and top, respectively. The characteristic velocity, u_2, is the velocity at which the Mach number begins to increase with increased acceleration. Thus, to mitigate heating while still achieving significant acceleration, the electromagnetic field should be chosen such that the inlet velocity-Mach number combination lies between the u_2 and u_3 curves. Electromagnetic fields that cause the inlet velocity to lie in this region limit total acceleration, but with the benefit of maintaining high overall efficiencies. As the load factor approaches unity, so does the efficiency. Finally, it should be noted that the behavior of these curves changes when considering variable area channels. If the channel is allowed to expand, the flow will accelerate faster with an increase in Mach number for a fixed electromagnetic field strength, leading to improved performance. To see more details about this plot and the theory of one-dimensional MHD-augmented flows, see Ref. [5].

3.2 Estimates of the Hall Parameter in PFE Operation

The preceding analysis was performed under the assumption of scalar conductivity. However, it was suggested in Chapter 2 that tensor conductivity is necessary to capture the anisotropy caused by the Hall effect. Scalar conductivity is a suitable assumption when the magnetic field does not significantly alter the plasma particle trajectories. It is when there are strong magnetic fields and low gas densities that the Hall effect is exacerbated. This relationship becomes apparent when returning to the definition of the Hall parameter, β_s, in Eq. (2.4), where q_s is the particle's charge, $|\vec{B}|$ is the magnitude of the magnetic field, m_s is the mass of the charged particle, and ν_{sH} is the heavy particle collision frequency.

$$\beta_s = \frac{q_s|\vec{B}|}{m_s\nu_{sH}} \tag{3.10}$$

The cyclotron frequency can be computed for various ionized species as a function of the magnetic field strength. Since the particle's angular speed around the magnetic field lines is inversely proportional to mass, electrons orbit much faster than the heavier ions. Fig. 3.2 shows the cyclotron frequencies for electrons and various ions relevant to this work. That is, argon ions, atomic nitrogen ions, and molecular nitrogen ions. The electron cyclotron frequencies are four to five orders of magnitude larger than those of the positively charged ions.

Cyclotron frequencies are straightforward to compute. However, estimating the collision frequencies between particles is also necessary to compute the Hall parameter, which is not as trivial. A collision frequency model is necessary to estimate the Hall parameter for different thermodynamic conditions at several altitudes. Atmospheric conditions (temperature, pressure, and density) for altitudes ranging from sea level to 50 km are taken from the 1976 Standard Atmosphere model and

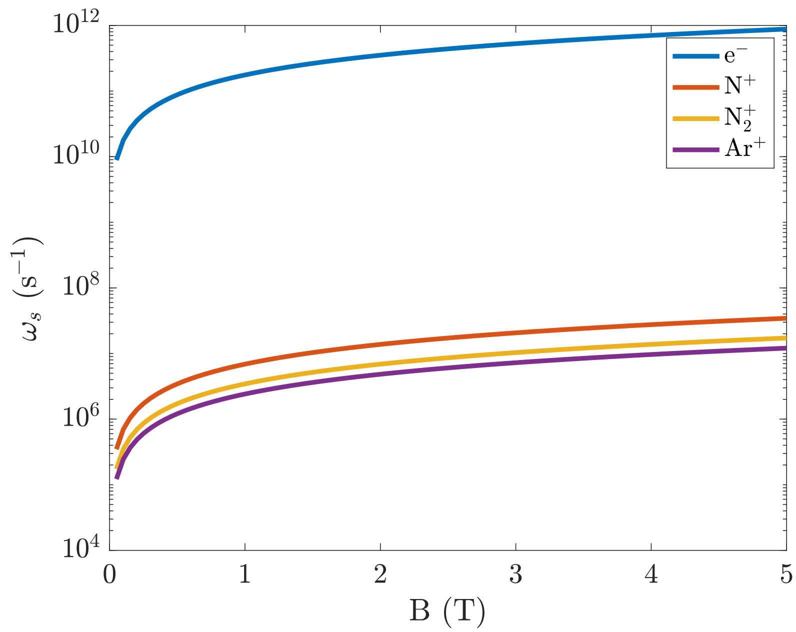

Figure 3.2: **Cyclotron frequency versus magnetic field for various charged species.**

are tabulated in Table 3.1 [95].

Table 3.1: Atmospheric conditions for altitudes ranging from 0 km to 40 km.

Alt. (km)	T (K)	p (Pa)	ρ (kg/m^3)
0	288.2	1.013×10^{5}	1.225×10^{0}
10	223.2	2.644×10^{4}	4.127×10^{-1}
20	216.7	5.475×10^{3}	8.803×10^{-2}
30	226.7	1.172×10^{3}	1.801×10^{-2}
40	251.1	2.775×10^{2}	3.851×10^{-3}
50	270.7	7.594×10^{1}	9.775×10^{-4}

The collision frequency between electrons and heavy particles is computed as a function of the electron energy, heavy particle density, and total elastic cross-section [74], as in Eq. (3.11), where k_B is the Boltzmann constant, T_e is the electron temperature, m_e is the mass of an electron, n_H is the number of heavy particles, and σ_{eH} is the electron-heavy particle collision cross-section.

$$\nu_{eH} = \sqrt{\frac{8k_BT_e}{\pi m_e}} n_H \sigma_{eH} \tag{3.11}$$

The collision cross-section for electrons and molecular nitrogen can be approximated as

$\sigma_{eN_2} = 1 \times 10^{-19}$ m^2. Although electron-heavy particle cross-sections are actually dependent on the electron energy, this approximation is adequate for electron energies between 1 eV and 10 eV [96, 97]. The collision frequency can be calculated using the following Coulomb cross-section for collisions between electrons and ions, such as N_2^+.

$$\sigma_{eN_2^+} = \frac{8\pi}{27}\frac{q_e^4}{k_B^2 T_e^2}\ln\left[1 + \frac{9k_B^3 T_e^3}{4\pi n_e q_e^6}\right] \tag{3.12}$$

In Eq. (3.12), q_e is the elementary charge, k_B is the Boltzmann constant, T_e is the electron temperature, and n_e is the number density of electrons. Caution must be exercised when using Eq. (3.12) because q_e and k_B are commonly given in cgs units, so the appropriate conversion factors must be employed to arrive at a cross-section in m^2. Assuming the atmosphere is solely made up of N_2 and the only ionized species is N_2^+, the collision frequency can be computed as a function of the degree of ionization for various altitudes. As the degree of ionization increases, the probability of Coulomb interactions also increases. Conversely, the electron-heavy collision frequency decreases as the electrons gain energy in the electric field. This effect is illustrated in Fig. 3.3 for $T_e = 300$ K, $T_e = 1$ eV, and $T_e = 5$ eV.

The electron-ion momentum transfer rate is negligible compared to the electron-neutral rate when the plasma is very weakly ionized ($\alpha \leq 1 \times 10^{-6}$), When the plasma is highly ionized ($\alpha \approx 0.1$), the Coulomb collisions become at least as dominant as the electron-neutral collisions, especially for the "cold" and "hot" electrons. In fact, when $T_e = 300$ K, $\nu_{eN_2^+} > \nu_{eN_2}$ for most of the degrees of ionization considered here. However, the collision rate varies drastically with the total number density, N, so the collision frequency decreases by several orders of magnitude between 0 km and 50 km. Since the electrons will be excited by the electric field in an MHD accelerator, it is unlikely that they will remain in equilibrium with the heavier gas at 300 K. Instead, a state of thermal nonequilibrium will exist between the electrons and heavy particles that depends on the properties of the gas and electric field strength.

The corresponding Hall parameters can be estimated now that the cyclotron and collision frequencies are known for various magnetic field strengths, altitude conditions, degrees of ionization, and electron temperatures. Figure 3.4 shows electron Hall parameters for altitude conditions from 0 km to 50 km and for degrees of ionization from $\alpha = 1 \times 10^{-6}$ to $\alpha = 1 \times 10^{-1}$ when the magnetic

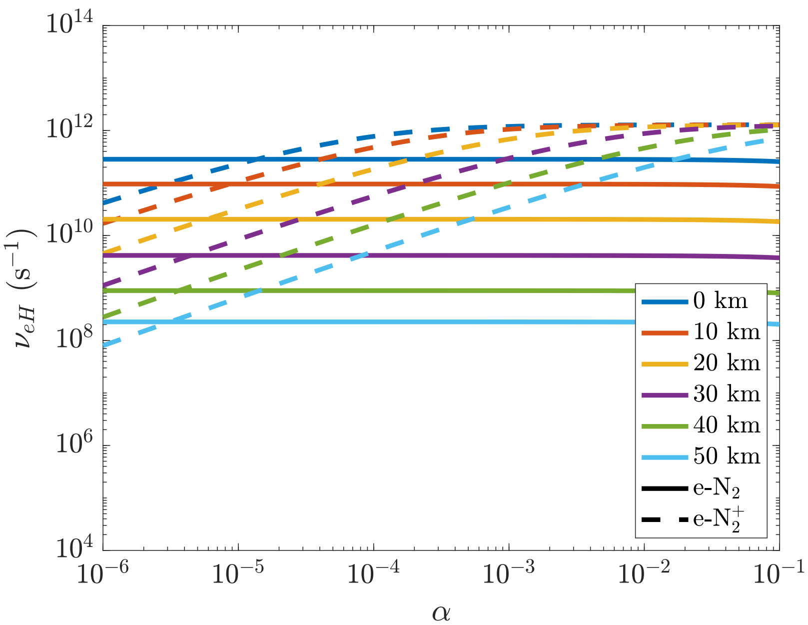

(a) **"Cold" electrons (T_e=300 K).**

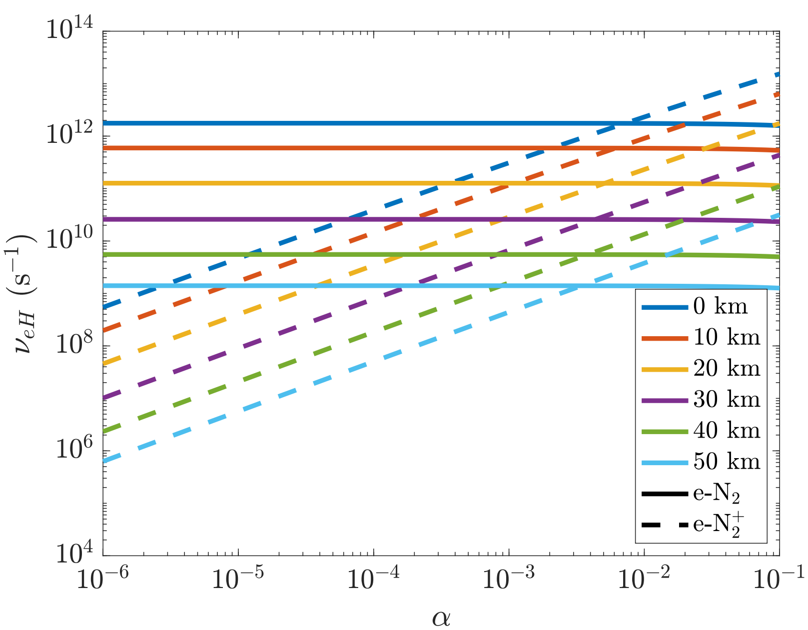

(b) **"Hot" electrons (T_e=1 eV).**

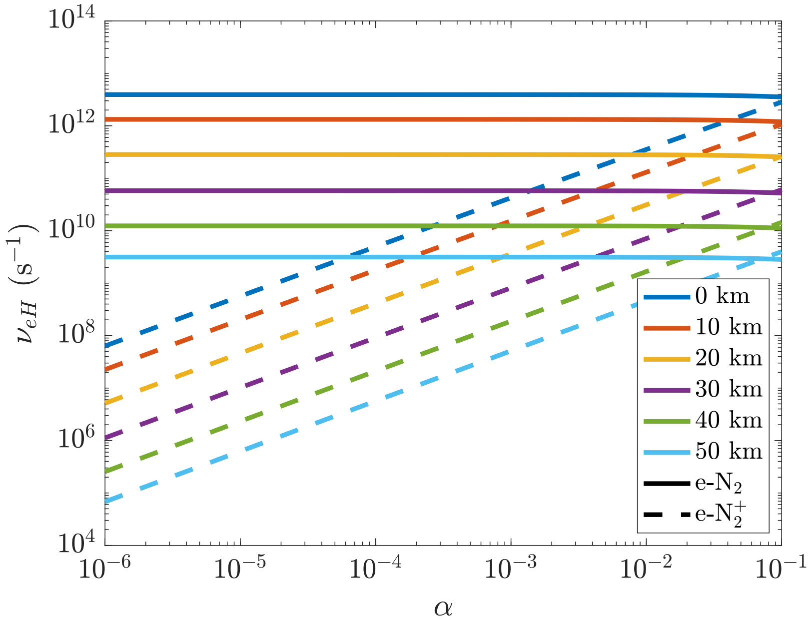

(c) **"Very hot" electrons (T_e=5 eV).**

Figure 3.3: **Electron-heavy particle collision frequency for a range of ionization levels and freestream conditions.**

field strength is $B = 1$ T.

The degree of ionization has the strongest effect on the Hall parameter order of magnitude when the electrons are relatively cool. As the degree of ionization increases, the Hall parameter also decreases due to the presence of Coulomb collisions. However, as altitude increases and freestream density decreases, the Hall parameter increases significantly. For altitudes above 30 km, the electron Hall parameter is at least on the order of $\mathcal{O}(10)$ for $\alpha = 1 \times 10^{-6}$. At these altitudes, maintaining a high degree of ionization not only ensures high electrical conductivity but also allows for improved efficiencies by limiting the Hall effect. Although the deleterious effects of the magnetic field could also be alleviated by using weaker magnets, that approach would also decrease the momentum transfer to the plasma.

Although strong magnetic fields lead to a greater Lorentz force term in the conservation of momentum equation, the applied electric field necessary to generate thrust also increases. This issue can be readily observed by recalling that the maximum velocity a hypersonic plasma can reach in a constant-area channel is the characteristic velocity, $u_3 = E/B$. Furthermore, stronger magnetic fields require heavier electromagnets and thus reduce payload capabilities.

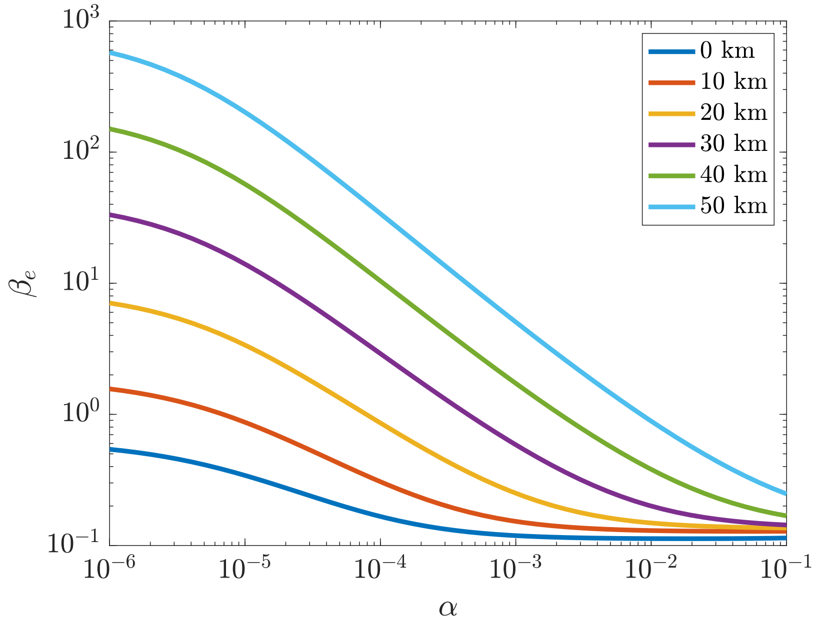

(a) **“Cold” electrons (T_e=300 K).**

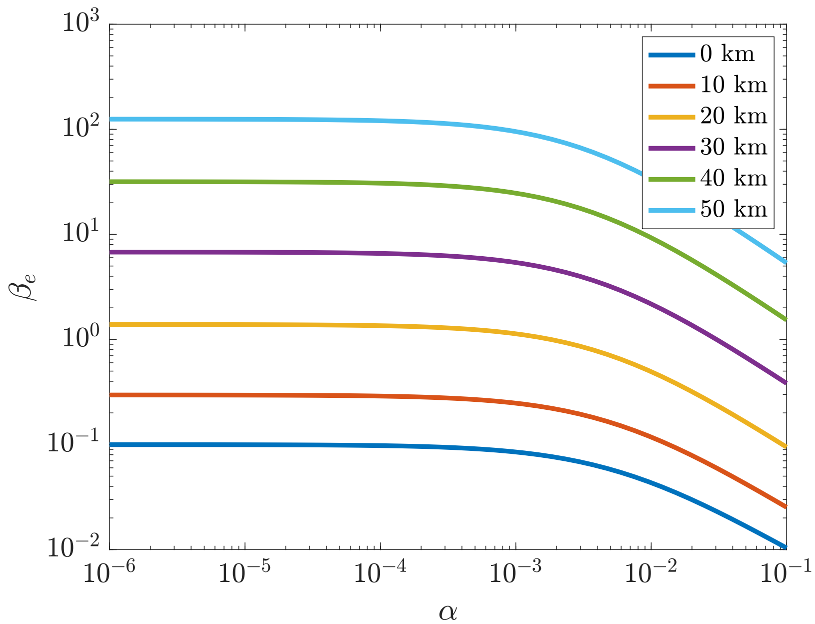

(b) **“Hot” electrons (T_e=1 eV).**

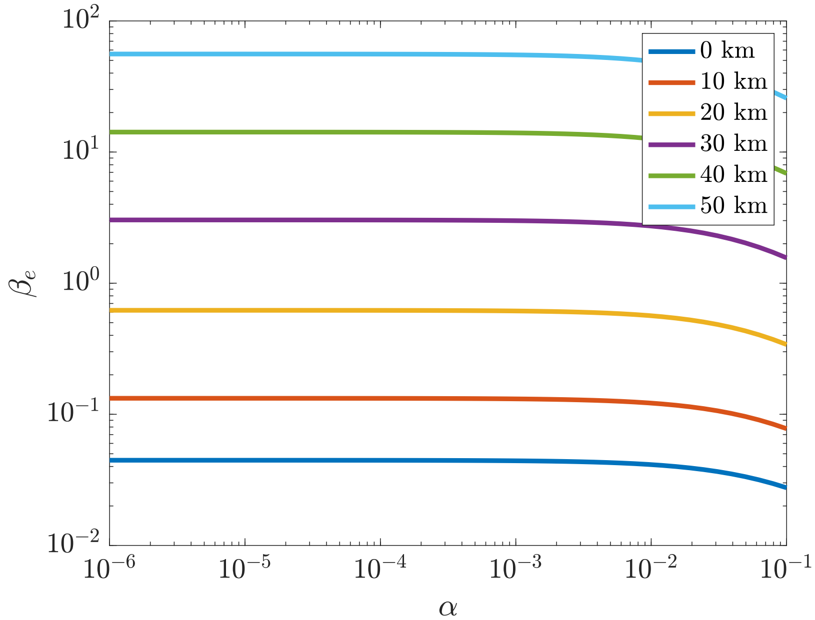

(c) **"Very hot" electrons (T_e=5 eV).**

Figure 3.4: **Electron Hall parameters versus degree of ionization and freestream conditions - B = 1 T.**

3.3 Overview of MHD Energy Converter Configurations

Many early attempts at designing and creating effective MHD converter devices centered around MHD generation. These attempts built upon existing technologies using liquid and solid metals to generate electrical power via motion through a magnetic field. MHD generation was seen as an attractive alternative to turbogenerators because of the material limitations in the mid-20th century. However, many of the insights discovered in those works are still directly applicable to MHD accelerators. For example, to arrive at the optimal MHD conversion performance, electrode placement decisions must be made so that the applied electric field interacts optimally with the moving fluid and magnetic field.

Consider an MHD channel where the flow moves in the positive x-direction and the magnetic field is in the positive y-direction. Under the assumption of scalar conductivity, without the Hall effect or ion slip, an applied electric field in the *negative* y-direction generates a Lorentz force in the flow's direction. In this case, the generalized Ohm's law in Eq. 2.21 is adequate. However, as was demonstrated in the preceding analysis, the Hall effect may be significant for flight conditions relevant to the PFE. Furthermore, ion slip might also be significant for higher altitude conditions when the plasma collisionality is low, and the magnetic field is strong. For weakly ionized plasmas, ion slip occurs when the current component from ions is greater than the electron component in the electric field direction. A simple expression for this is when the ion slip factor, s, is greater than unity.

$$s = \beta_e \beta_i B_y^2 \tag{3.13}$$

Ion slip modifies the effective electrical conductivity by a factor of $1 + s^2$ in the denominator. When the Hall parameters are near unity, an electric field in the x-direction is necessary to ensure the current density produces a Lorentz force in the flow direction. The generalized Ohm's law can then be reduced to the following equations for the current components in the electric field direction and the Hall direction.

$$\begin{aligned} j_x &= \frac{\sigma_e}{1+\beta_e^2}(E_x + \beta_e(E_z + uB_y)) \\ j_z &= \frac{\sigma_e}{1+\beta_e^2}(-\beta_e E_x + E_z + uB_y) \end{aligned} \tag{3.14}$$

Two categories of MHD channels arise out of the consequences of the Hall effect. The first category is the *Faraday configuration* in which the applied electric field is transverse to the flow and magnetic fields. Faraday configuration MHD channels are optimal when the Hall parameters are very small, $\beta_e \ll 1$. A subset of Faraday configuration channels are *segmented Faraday* configurations in which the electrodes do not span the entire length of the channel. Instead, many sets of individually biased electrodes are placed along the channel. In order to enforce that the axial currents disappear in segmented Faraday channels, the electrodes must be thin with respect to the channel's length. Furthermore, complications still arise with segmented electrodes when the Hall effect leads to a concentration of current near the edges of the electrodes.

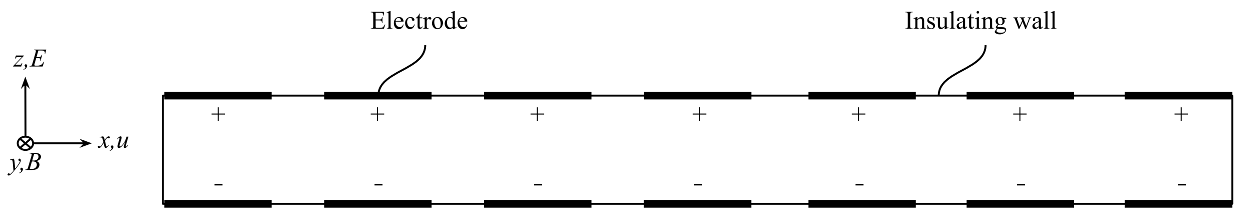

Figure 3.5: **Segmented Faraday configuration MHD accelerator.**

The second category of MHD channels is the *Hall configuration* in which the applied electric field is generated by a potential difference driven by electrodes placed on the ends of the channel. When the Hall parameter is greater than unity, this electric field configuration sends electrons to the walls as if the Hall parameter was small and the electric field was applied in the Faraday configuration. However, a transverse component of the electric field arises due to the motion of the plasma through the magnetic field lines, which in turn induces a Hall current in the flow direction. This current can be minimized by simultaneously applying a transverse field that is equal to, or near equal to, the induced field, i.e., $E_z \approx uB_y$. In this case, an axial current will still form but at a strength of $1/\beta_e$ of the transverse component.

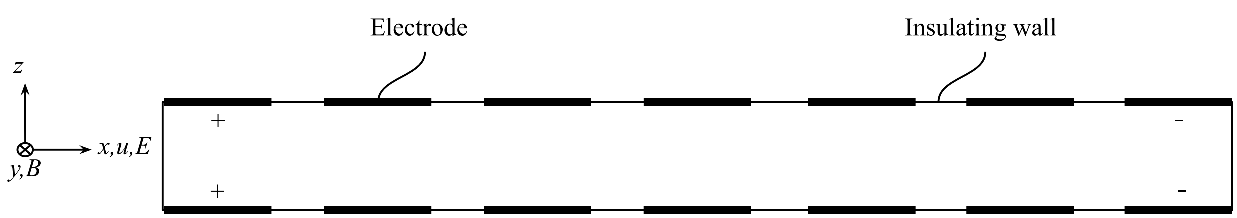

Figure 3.6: **Hall configuration MHD accelerator.**

Thus, segmented electrodes offer an advantage for both Hall and Faraday configuration MHD channels. By independently biasing each pair of electrodes, any combination of electric field geometries can be applied to the plasma to create an optimal forcing. It is not trivial, however, to design such configurations a priori without knowing how the plasma reacts to the applied electromagnetic fields. Numerical simulations offer assistance in answering these open questions for a range of general conditions.

3.4 Electric Field and Ionization Requirements for PFE Operation

Now that Hall parameter estimates have been made for a full range of altitude conditions relevant to the PFE and the two basic MHD converter configurations have been presented, analyses will be performed to assess requirements for successful MHD acceleration. Namely, minimum electric field requirements will be defined for a range of altitudes and Mach numbers when the Hall effect is expected to play both a minor and a significant role in hypersonic MHD accelerator design. These requirements will help inform when an axial field is necessary for flow acceleration. Next, another dimensionless parameter will be introduced to quantify how effectively a given MHD channel configuration will produce flow field augmentation through the applied electromagnetic fields. It will be found that there is a baseline level of ionization that must be achieved in order to expect MHD interaction.

3.4.1 Electric Field Predictions

First, it is imperative to obtain predictions for how strong the electric field must be in both Faraday and Hall configuration MHD channels to achieve flow field acceleration. To do so, the electric field must be stronger than the induced field from the plasma moving through the magnetic field, as was highlighted in Section 3.1. Assuming a magnetic field strength of 1 T, the electric field is approximated as $E = u/B$. The corresponding electric field strengths are plotted in Fig. 3.7 for Mach numbers between 5 and 15 and altitudes between 0 km and 50 km. For Mach 5 flow, the minimum electric field strength is between 1500 V/m and 2000 V/m. As the Mach number doubles and triples, so does the electric field requirement.

The transverse magnetic field strongly affects the mobility of ions and electrons in an electric field. As the magnetic field strength increases, the charged particles tend to orbit more around the field lines such that the effective electric field strength is strongly affected in Faraday configuration channels. An *effective* electric field strength can be defined, which accounts for this effect.

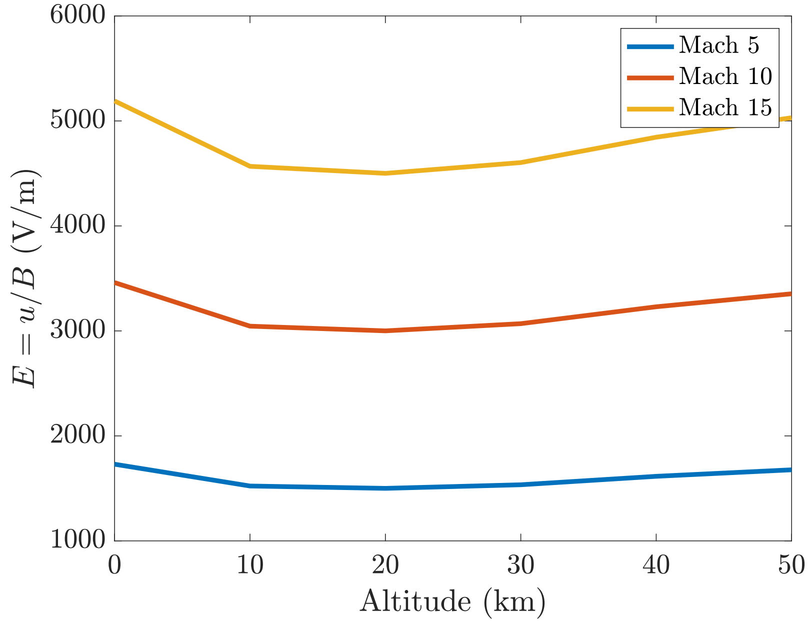

Figure 3.7: **Electric field strengths versus altitude for hypersonic Mach numbers.**

$$E_{eff} = \frac{E^2}{1 + \beta_e^2} \tag{3.15}$$

It is not straightforward to define an effective electric field strength without knowledge of the plasma it is interacting with since the Hall parameter depends on the magnetic field strength, the degree of ionization, and the freestream density. The effective electric field is plotted in Fig. 3.8 for the same altitude and Mach number conditions as Fig. 3.7, assuming the electrons have $T_e = 1$ eV and the degree of ionization is 1×10^{-3}.

For altitudes less than 20 km, the magnetic field strength does not strongly affect the effective electric field. However, as the altitude increases from 20 km, the magnetic field reduces the electric field substantially. By 50 km, the electric field strength is four orders of magnitude lower than its nominal value without the magnetic field.

For altitudes of 30 km and above, the high Hall parameters suggest that the Hall configuration is not only optimal but necessary for successful engine performance. By 50 km, the magnetic field reduces the conductivity in the electric field direction entirely. At these higher altitudes,

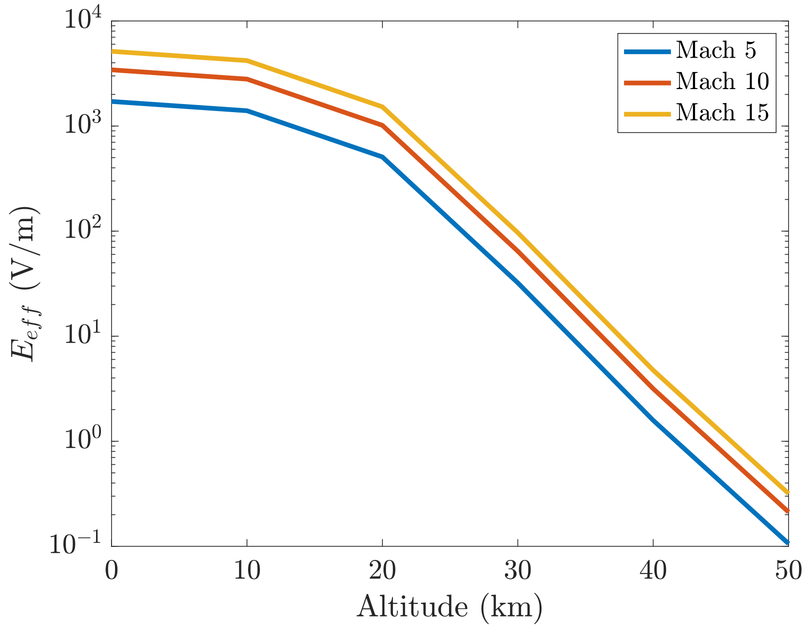

Figure 3.8: **Effective electric field strengths versus altitude for hypersonic Mach numbers.**

axial electric fields should be included when running numerical simulations. The constraint $E_x = -\beta_e(E_z + uB_y)$ can be used to ensure that the axial current is minimized. Otherwise, applying an electric field solely in the transverse direction will yield no acceleration. Axial and transverse electric field estimates can be made for Hall configuration MHD channels by again assuming the transverse field is equal to the induced field, $E = u/B$. Figure 3.9 shows the relative magnitudes of the transverse and axial electric field strengths.

For altitudes less than 20 km, the axial field is less than or equal in magnitude to the transverse field. However, as the Hall parameters increase, the necessary axial field also increases. The total electric field increases such that the axial field makes up most of the total field. At 50 km altitude, the axial field is two orders of magnitude stronger than the transverse field.

3.4.2 Magnetic Interaction Parameter

In Chapter 2, Ohm's law and the magnetic induction equation were used to derive a dimensionless constant known as the *magnetic Reynolds number*, which measures the relative importance

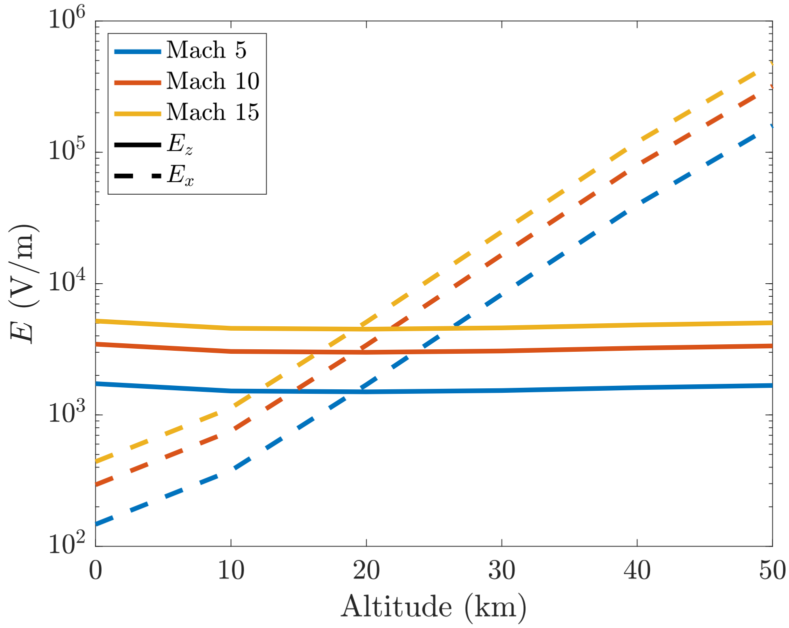

Figure 3.9: **Transverse and axial electric field strengths for Hall configuration MHD accelerators for a range of altitudes and Mach numbers.**

of magnetic induction to magnetic diffusion. Another helpful dimensionless number called the *magnetic interaction parameter* or *Stuart number* can be defined by comparing the advective term and the Lorentz force term in the conservation of momentum equation.

$$\frac{\partial \rho \vec{u}}{\partial t} + \underbrace{\nabla \cdot (\rho \vec{u} \otimes \vec{u})}_{\frac{\rho u^2}{L}} + \nabla \cdot (p\vec{\vec{I}} - \vec{\vec{\tau}}) = \underbrace{\vec{j} \times \vec{B}}_{\sigma u B^2} \tag{3.16}$$

By comparing the relative scales of the advective term, $\frac{\rho u^2}{L}$, and the Lorentz force term, $\sigma u B^2$, the Stuart number can be defined as in Eq. 3.17 below.

$$S = \frac{\sigma B^2 L}{\rho u} \tag{3.17}$$

The electrical conductivity can be estimated from the electron-heavy particle collision frequency estimates above by using Eq. (2.71). Then, the Stuart number can be estimated based on the MHD channel configuration of interest. First, however, the characteristic length scale, L, the flow velocity u, and the freestream density, ρ, must be defined. For this analysis, the vehicle is

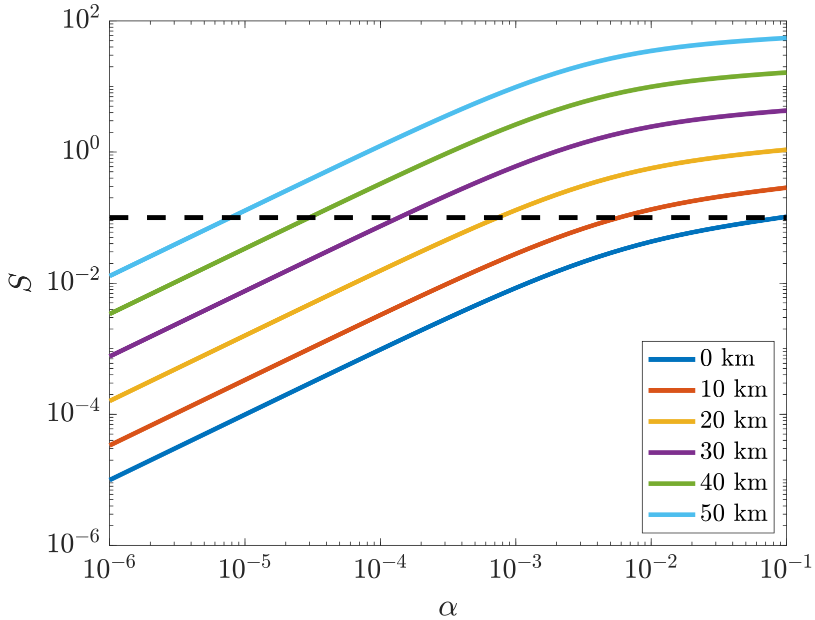

Figure 3.10: **Magnetic interaction parameter, or Stuart number, versus degree of ionization for a range of altitudes.**

assumed to be flying at Mach 10 at the freestream conditions listed in Table 3.1. Furthermore, a nominal characteristic length scale of $L = 0.1$ m is used, the magnetic field strength is $B = 1$ T, and the electrons are assumed to be at $T_e = 1$ eV. Using these definitions, the Stuart number is plotted in Fig. 3.10 for altitudes between 0 and 50 km and degrees of ionization between 1×10^{-6} and 1×10^{-1}.

In Fig. 3.10, the black dashed line corresponds to a magnetic interaction parameter of $S = 0.1$. With a notional magnetic forcing of only 10% of the inertial forces, it is unlikely that a practical MHD channel could substantially augment the bulk flow. For example, from these calculations, it is clear that regardless of the degree of ionization, MHD interaction is difficult to obtain for the hypersonic flow conditions at 0 km, magnetic field strength, and characteristic channel length given here. Longer channels and stronger magnetic fields would be necessary for these higher-density applications. Similarly, at 10 km and 20 km altitude conditions, the degree of ionization would need to be approximately 1×10^{-2} and 1×10^{-3}, respectively, to ensure adequate collisions between electrons and neutrals. However, it should be made explicit here that low-altitude high-

Mach number flight suffers from a much more restrictive limitation due to the extreme thermal and structural loads a vehicle would experience in those flight regimes.

As the altitude increases, the degree of ionization requirements lessen as the inertial forces become easier to overcome with the applied electromagnetic forces. Similarly, for each altitude, the momentum transfer from the electrons to the neutrals is more frequent as the degree of ionization increases, improving efficiency.

3.5 Conclusion

In this chapter, theoretical and back-of-the-envelope analyses were performed to highlight the operating conditions and requirements for successful hypersonic thrust generation. The one-dimensional MHD equations have been solved analytically to illustrate the performance of any MHD energy conversion device. Namely, these solutions illicit a very informative discussion in the context of velocity versus Mach number space since these two quantities alone provide information regarding both the Joule heating and Lorentz force acceleration. Several regions in this space dictate how any plasma flow will react to the applied electromagnetic fields. One region, in particular, defines the acceleration of supersonic plasmas between two characteristic electromagnetic field strengths. The solutions to the governing equations in this region can and will be used to design PFE configurations and understand their performance for the relevant operating regimes.

Next, the cyclotron and collision frequencies for various conditions were considered. Namely, the collision frequencies were calculated for a wide range of altitudes, electron energies, and degrees of ionization. Although these calculations were first-order estimates, they serve as a baseline for understanding and guiding PFE design. Electron Hall parameters were computed using these predictions as a function of the magnetic field strength. It was found that high Hall parameters ($\beta_e > 1$) are to be expected for altitudes greater than 20 km. High Hall parameters result in a current component that is transverse to the magnetic and electric fields.

Two canonical classifications of MHD devices were presented. The first classification is Faraday configurations, which apply an electric field transverse to the magnetic field and the flow's velocity. This configuration can be improved by segmenting the electrodes such that Hall currents are mitigated. However, Faraday mode channels suffer from inefficiencies when the Hall parameter is very large. The second classification of MHD devices is known as Hall configuration channels. Hall configuration channels apply an electric field that is along the flow direction. However, the magnetic field acts to send the charged particles to the walls such that the Lorentz force still transfers momentum from the electrons to the bulk neutrals.

The Hall parameter estimates were used to determine the approximate electric field strengths for a few representative cases. First, minimum transverse electric field strengths were defined based on the Mach number of the flow and the freestream conditions corresponding to altitudes from 0 km to 50 km. Then, effective electric field strengths were computed, taking into account the magnetic field effects, for the same cases and a 1 T magnetic field. This analysis highlighted that the Faraday mode of operation would be highly inefficient for altitudes above 20 km. Below this altitude condition, the electric fields are on the order of $\mathcal{O}(1 \times 10^3 - 1 \times 10^4)$ V/m. The same calculations were made for Hall configuration accelerators. For altitudes below 20 km, the applied axial electric field would be less than or equal to the transverse field. Above 20 km, the axial fields necessary for acceleration become much larger than the transverse, leading to fields on the order of $\mathcal{O}(1 \times 10^5 - 1 \times 10^6)$ V/m.

Finally, the degree of ionization must be adequately high to ensure that the applied electromagnetic energy gets transferred to the bulk plasma neutrals. Using the magnetic interaction parameter, or Stuart number, ionization requirements were defined for a flight regime of interest. For altitudes between 0 km and 10 km, the mean degree of ionization must be very high, i.e $\alpha \approx 1 \times 10^{-2}$, to arrive at marginal MHD interaction. If not, there will not be enough charged particles for the neutrals to collide with during their residence in the channel. As the freestream becomes less dense, the inertial forces also decrease, which weakens the requirements on baseline degree of ionization.

Although these analyses are very useful for defining the operating envelope of hypersonic MHD accelerators, their insights are limited for designing actual prototypes. Numerical simulations will be performed in the following chapters using the tools outlined in Chapter 2 to arrive at more predictive models. Furthermore, several decisions were made about the flow field quantities and channel design variables based on the applications relevant to this work. For example, assumptions were made regarding the flow's Mach number, the mean electron energy, the magnetic field strength, etc.. When considering other systems, these assumptions may need to change, however, it is recommended that analyses like the ones performed here should be carried out before simulations begin. Otherwise, the design and analysis processes may become unnecessarily tedious and unproductive.

Chapter 4

One-Dimensional Flow Modeling

This chapter will present solutions using the one-dimensional model from Chapter 2 to analyze the behavior of hypersonic MHD accelerator channels. First, numerical solutions for various inlet conditions will be discussed in the context of their theoretical counterparts from the preceding chapter. The simulations will be performed with several assumptions, such as constant conductivity, electric field, and cross-sectional area. The assumptions will gradually be relaxed in order to understand the impact of each one on the performance of PFE systems.

The one-dimensional numerical solutions reproduce the relationship between Joule heating and total acceleration for a given electromagnetic field configuration predicted by the one-dimensional MHD accelerator theory. Physical insights gained from these solutions and accompanying theory can be used to design effective PFE prototypes for future testing. For example, two strategies for improving channel performance will be explored to illustrate how acceleration can be improved while limiting the deleterious effects of Joule heating. However, the appropriate plasma chemistry models must be identified before the numerical simulations can provide any helpful intuition into how these systems operate. Once these models are implemented, ionization estimates can be made for various operating conditions. Then, one-dimensional numerical solutions, which include ionization, recombination, and the Hall effect, will be presented for a representative case. Finally, performance predictions are given for a range of freestream Mach number and altitudes relevant to PFE operation.

4.1 Exploring the Velocity Versus Mach Number Space Using the One-Dimensional Model

First, the one-dimensional model is used to probe the different regions in the velocity versus Mach number space that was described in Chapter 3. To do so, the governing equations are solved for various operating conditions by applying the appropriate boundary conditions and tuning the electric and magnetic field strengths. The results shown in this chapter are for partially ionized argon (Ar,Ar^+,Ar_2^+,e^-) due to its atomic structure in the neutral state and its simplified ionization kinetics. Furthermore, future wind tunnel tests in which these models can be validated may use argon.

In three-dimensional PFE simulations, an electric potential is set at the electrode boundaries, and the electric field is taken to be the gradient of that potential. In one spatial dimension, the electric field is prescribed throughout the entire domain of the PFE. For simplicity and preliminary design analysis, the electric field does not decrease in regions where insulating walls are expected. Although this may sometimes be the case for the three-dimensional electric field generated by segmented electrodes, this assumption does not detract from the insights gained from the one-dimensional model.

There are several design variables to consider when analyzing PFE configurations. Namely, the electric and magnetic field strengths can be tuned to find the appropriate operating regime in velocity versus Mach number space. Furthermore, cross-sectional area and electrode spacing can be adjusted to arrive at the optimal configuration for efficiently generating thrust in hypersonic flight.

The simplified model geometry in the following simulations comprises a Faraday configuration MHD channel with a square cross-section. The channel width and height are both 10 cm at the inlet, which is on the same order of magnitude as past MHD accelerator concepts [31][37], and the length is 50 cm. Larger channels may be expected in the future, but this geometry is amenable for model development and preliminary analysis. Based on the current electromagnet technology, the magnetic field strength is 1 T in all cases. The choice of the electric field in the PFE is then determined by inlet velocity and desired total acceleration. The electric field is prescribed in the channel based on the maximum centerline value in the three-dimensional channel. This value is approximately the electric potential prescribed at the electrodes divided by the width of the channel.

The following notation is presented to facilitate discussion regarding the design of electromagnetic fields for MHD channels. For an inlet velocity, u_{in}, inlet Mach number, M_{in}, ratio of specific heats, γ, and magnetic field strength, three characteristic electric fields dictate specific regimes of MHD channel operation, all of which are related to the characteristic velocities u_1, u_2, u_3. The first is the characteristic electric field, E_1, which is the electric field strength in which $u_{in} = u_1$.

$$E_1 = \frac{\gamma B u_{in}}{\gamma - 1} \tag{4.1}$$

For a supersonic plasma, E_1 can be seen as an upper limit to the electric field without causing severe heating. This can be seen in the lower right region of Fig. 3.1, where the applied electromagnetic fields cause a sharp decrease in Mach number. Meanwhile, the electric field should be greater than E_1 for subsonic plasmas to achieve acceleration, which can be seen in the lower left region of the same plot. Similarly, E_2 is the electric field in which $u_{in} = u_2$.

$$E_2 = \frac{\gamma B(2 + (\gamma - 1)M^2)u_{in}}{(\gamma - 1)(1 + \gamma M^2)} \tag{4.2}$$

Setting the electric field to E_2 can be seen as the "optimal" selection for supersonic plasmas, in the sense that this configuration achieves the greatest amount of acceleration while avoiding substantial heating. However, achieving acceleration with an increasing Mach number for a subsonic plasma occurs by setting $E > E_2$. Finally, E_3 is the electric field such that $u_{in} = u_3$.

$$E_3 = u_{in} B \tag{4.3}$$

4.1.1 Subsonic Acceleration

When $E < E_3$, the device acts as an MHD generator for a supersonic plasma. Theoretically, acceleration occurs when the inlet is subsonic and $E < E_3$. However, $\frac{dM}{dx}$ is positive but near zero in this regime. In subsonic one-dimensional simulations, a notion of the thermodynamic state of the gas just downstream of the boundaries is needed to compute the boundary conditions. In these simulations, density is extrapolated from the interior at the inlet, and a back pressure is specified downstream of the outlet. In the case where the electric field is weak, and the flow is initially subsonic, the plasma heats at the inlet. Since momentum and total temperature are being enforced at the inlet, the velocity at the inlet decreases. Meanwhile, if the back pressure is equal to the freestream pressure, a favorable pressure gradient forms down the channel that overwhelms the Lorentz force. However, as it was mentioned before, $\frac{dM}{dx}$ must remain small as the flow is accelerating and cooling due to this expansion. As a result, the solution does not travel far along its curve in velocity versus Mach number space. Instead of the flow developing along the prescribed path, as will be seen in the subsequent test cases, it is actually the inlet boundary condition that changes, in this case, such that inlet conditions move closer to the $u_{in}/u_3 = 1$ line as the solution develops.

A more interesting situation arises when an electric field, $E > E_1$, is applied to a subsonic gas. As described above, prescribing the electric field to be less than E_3 results in minimal acceleration. Prescribing the electric field between E_2 and E_1 results in acceleration at the cost of heating such that u_1 is the maximum velocity achievable. However, for electric fields stronger than E_2, the plasma accelerates with increasing Mach number. There is even a case where the subsonic plasma can pass through the sonic line and accelerate to $M = \sqrt{5}$. The plasma reaches Mach 1 at the outlet for stronger electric fields but will not pass through it. The applied electromagnetic field will cause any perturbation at the outlet to return to the sonic condition.

Consider a Mach 0.8 argon plasma at sea level conditions entering an MHD channel with a magnetic field strength of $B = 1$ T as an illustrative example. The inlet velocity is $u_{in} = 253$ m/s and the characteristic electric fields are $E_1 = 623$ V/m, $E_2 = 742$ V/m, and $E_3 = 253$ V/m. If an electric field is applied, $E = 1000$ V/m, the flow is expected to accelerate while the Mach number tends toward Mach 1. Figure 4.1 shows the velocity and temperature profiles assuming a constant conductivity of 100 $\Omega^{-1}\text{m}^{-1}$ and 500 $\Omega^{-1}\text{m}^{-1}$.

For both values of electrical conductivity, the subsonic flow is both accelerated and heated from the inlet to the outlet. However, the total acceleration and heating are less for the lower conductivity case. Note that the inlet boundary conditions do not precisely match up with the velocity condition ($u_{in} = 253$ m/s) and the sea level condition ($T_{in} = 288$ K) stated above. Again, that is because, for subsonic inlet conditions, all of the primitive variables are not prescribed. Instead, total temperature and momentum are specified, and a single variable (density in this implementation) is extrapolated from the interior. Thus, waves can propagate out of the domain through the inlet and change the incoming velocity and temperature. This leads to transience in the solution as the characteristic electric field strengths in Eqs. (4.1-4.3) are effectively changed. The final solution then lies on a curve in velocity versus Mach number space that differs from the initial solution. Figure 4.2 shows the final solution in that space for the same conditions as Fig. 4.1.

The flow does not reach u_1 or Mach 1 for the case with lower electrical conductivity, $\sigma = 100$ $\Omega^{-1}\text{m}^{-1}$. However, the initially subsonic gas can pass through Mach 1 with a high enough electrical conductivity and $E = 1000$ V/m. Using the inlet boundary conditions of constant momentum and total temperature, the solution automatically aligns with the curve in velocity versus Mach number space that passes through the point (Mach 1, u_1).

4.1.2 Supersonic Acceleration

Now consider a Mach 1.2 flow of argon at sea level conditions and two levels of electrical conductivity, $\sigma = 100$ $\Omega^{-1}\text{m}^{-1}$ and $\sigma = 500$ $\Omega^{-1}\text{m}^{-1}$. The inlet velocity is $u_{in} = 379$ m/s and the characteristic electric field strengths are $E_1 = 948$ V/m, $E_2 = 826$ V/m, and $E_3 = 379$ V/m. First, the case where $E > E_1$ will be examined.

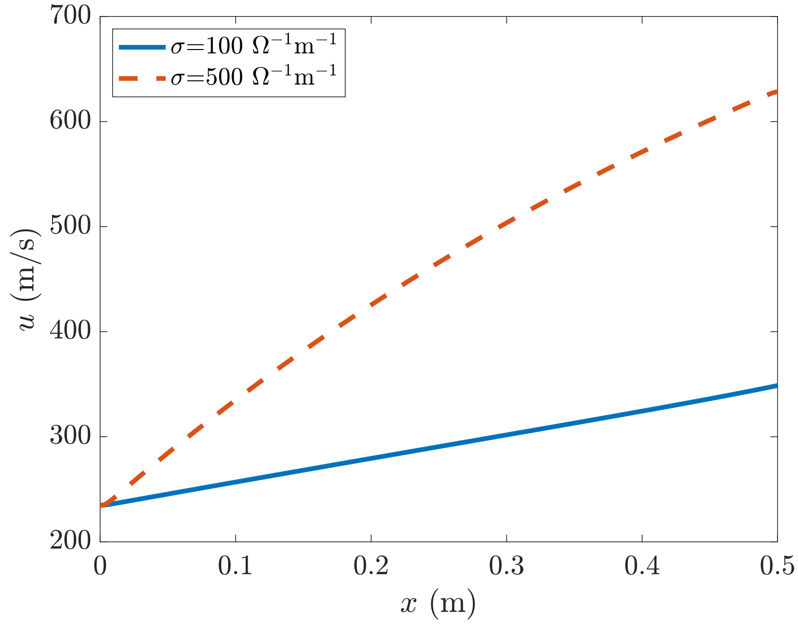

(a) **Velocity profiles.**

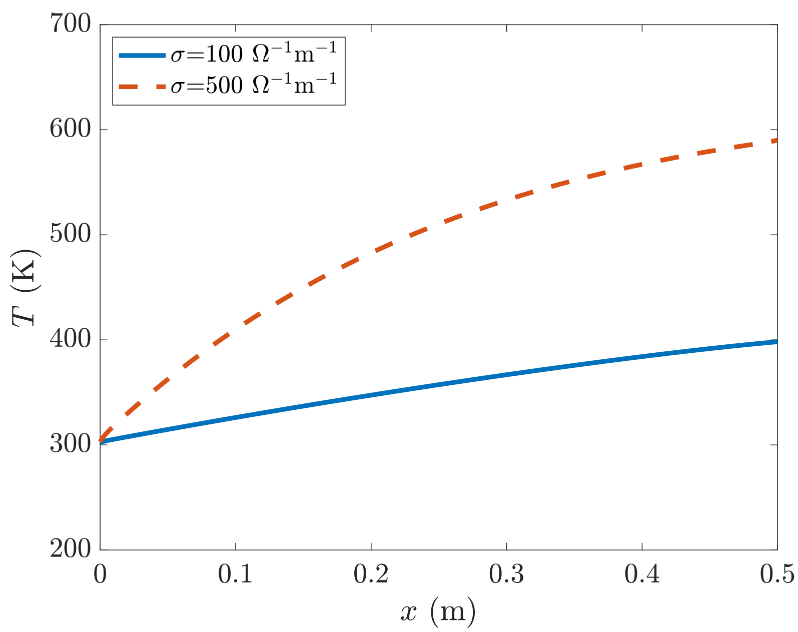

(b) **Temperature profiles.**

Figure 4.1: **Velocity profiles for an initially subsonic plasma with $E > E_1$.**

By prescribing an $E = 1500$ V/m electric field, an initial decrease in Mach number with slight deceleration is expected. When the flow reaches the sonic condition at the outlet boundary, the

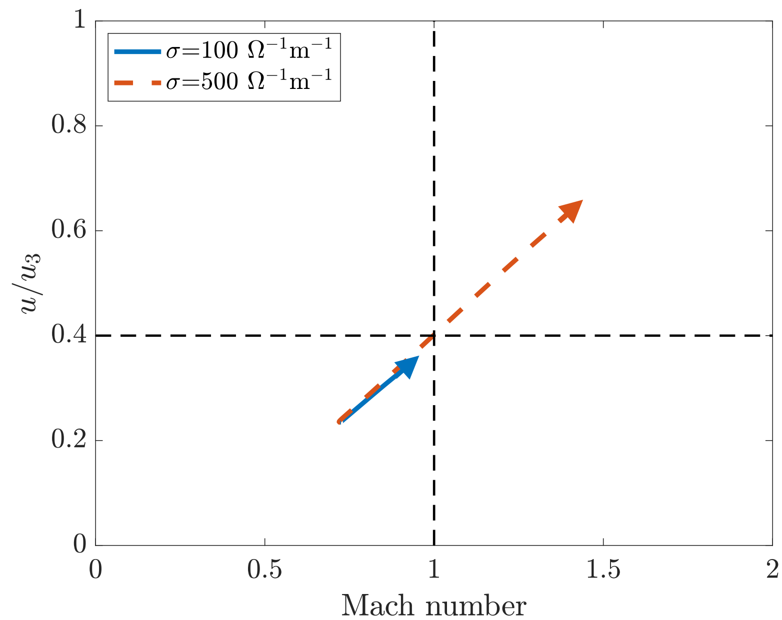

Figure 4.2: **Velocity versus Mach number curves for an initially subsonic plasma with $E > E_1$.**

balance between pressure gradients and electromagnetic forces will act to keep the flow there if the electromagnetic interaction is not strong enough. However, if the conductivity is high enough, the flow will pass through Mach one at the outlet, and Joule heating will cause a significant temperature rise and deceleration that act similar to a normal shock propagating upstream through the domain. Figure 4.3 shows the velocity and temperature profiles for these cases once the solution reaches a steady state.

Once again, it is noted that the final inlet conditions do not match the values given above for the flow moving at Mach 1.2 at sea level conditions. Similarly, both cases exhibit net acceleration and heating with the $\sigma = 500\ \Omega^{-1}\mathrm{m}^{-1}$ case leading to higher outlet velocity and temperature. By plotting both solutions in velocity versus Mach number space, which is done in Fig. 4.4, it is clear that the flow becomes subsonic at the inlet and only becomes supersonic again for the higher conductivity case near the outlet of the channel. Although the lower conductivity case gets close to returning to Mach 1 at the outlet, it does not fully return to that condition. It is concluded from this analysis that when the electric field is strong enough, the interaction between the subsonic boundary conditions and the applied electrodynamic forcing causes initially supersonic solutions to

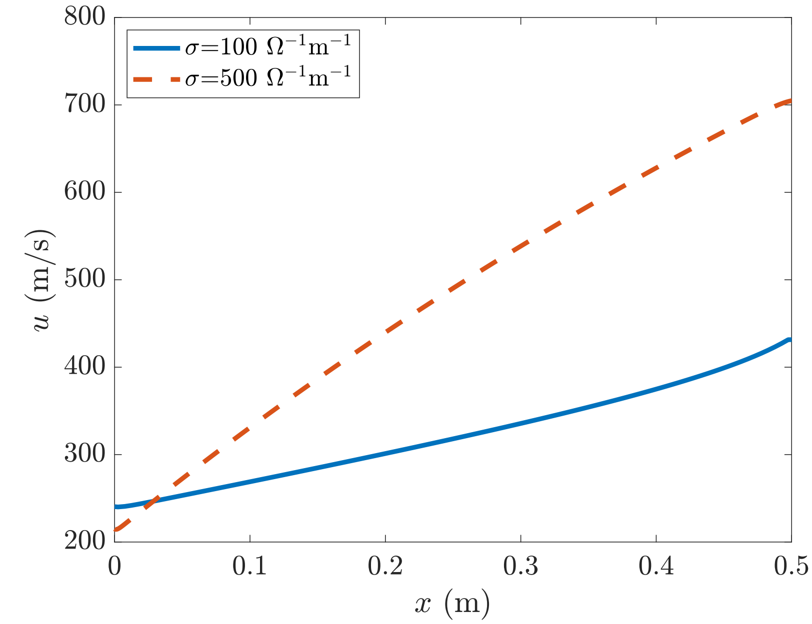

(a) **Velocity profiles.**

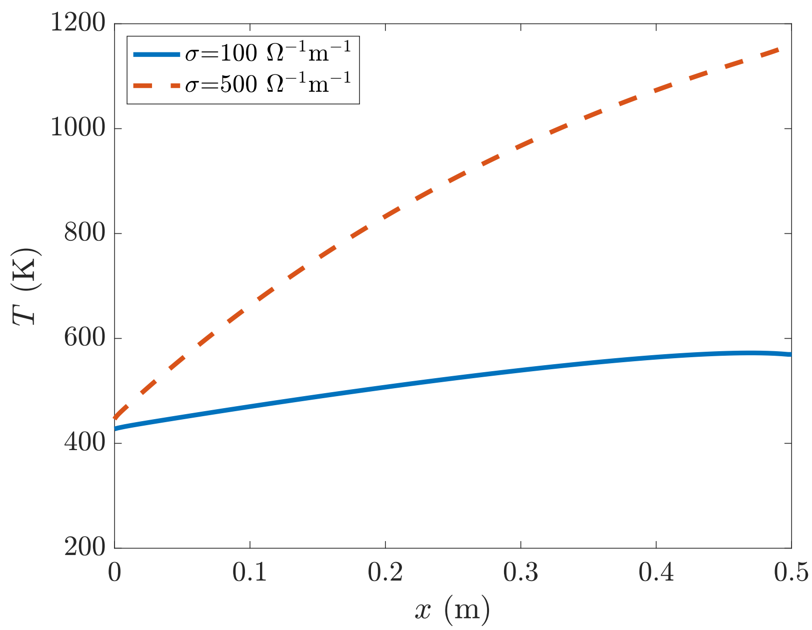

(b) **Temperature profiles.**

Figure 4.3: **Velocity profiles for an initially supersonic case with two electrical conductivities.**

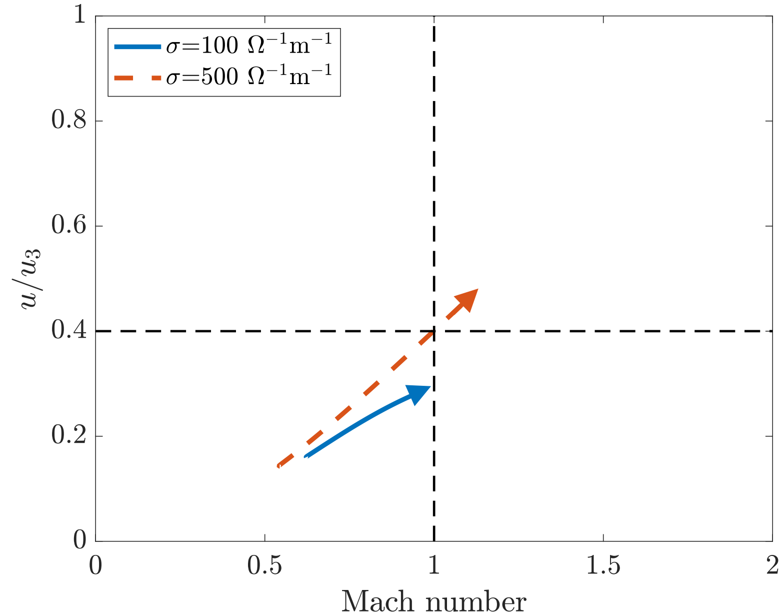

Figure 4.4: **Velocity versus Mach number curves for an initially supersonic case with two electrical conductivities.**

converge to the curve that smoothly passes through Mach 1 at $u = u_1$.

Strong Joule heating in the channel leads to transience in the solution such that the flow goes from entirely supersonic at the initial condition to entirely subsonic shortly thereafter. The Mach number is plotted at four different times during the simulation to visualize the temporal evolution of the flow. These times correspond to the initial condition, $\tau_0 = 0$ s, two times during the flow development, $\tau_1 = 0.5 \times 10^{-3}$ s and $\tau_2 = 1.3 \times 10^{-3}$, and then a time corresponding to when the flow reaches steady state, $\tau_3 = 3.8 \times 10^{-3}$.

The initial condition in the channel corresponds to the boundary conditions prescribed at the inlet, i.e., Mach 1.2 flow at sea level conditions. However, by τ_1, Joule heating has already caused the flow to become subsonic throughout most of the domain. A normal-shock-like structure forms near the inlet. Then, that structure is propagated upstream and through the boundary, which makes the inlet subsonic. Downstream in the flow, the outlet is temporarily transonic, and the applied Lorentz force is combatting an adverse pressure gradient. However, in this case, the plasma is electrically conductive enough to allow the applied electromagnetic field to impart acceleration

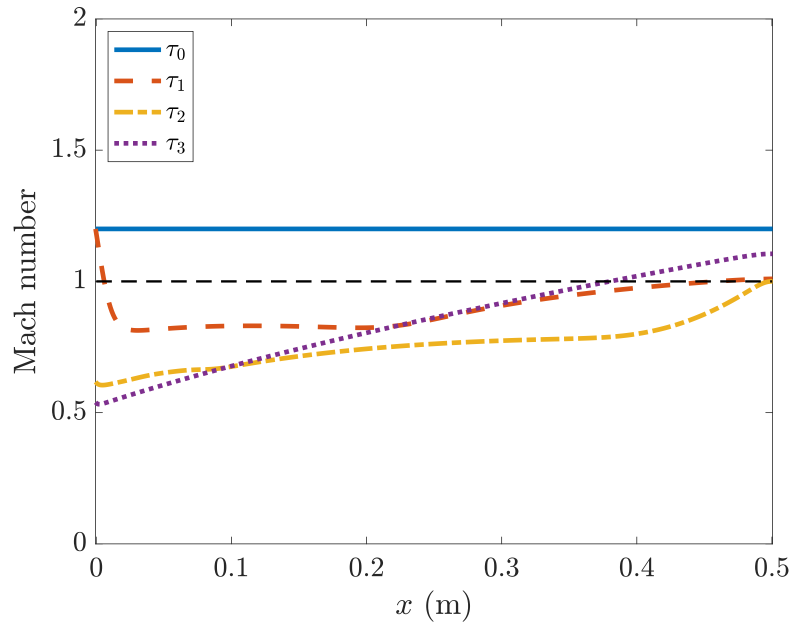

Figure 4.5: **Temporal evolution of Mach number.**

such that the flow passes through Mach 1.

4.2 Hypersonic MHD Accelerator Design

The applied electromagnetic field must be chosen carefully in a hypersonic MHD accelerator to control the balance between total acceleration and Joule heating. It was just shown that setting the electric field to be greater than E_1 for channels with initially supersonic inlets leads to inefficient performance. Although acceleration occurs in those cases, the flow first experiences deceleration and heating such that the flow becomes subsonic. Alternatively, smooth acceleration is desirable to improve engine efficiency. As such, based on the discussion provided in Chapter 3, the electric field should be set such that $E_3 < E < E_1$.

For a given inlet velocity and Mach number, the flow acceleration in the channel depends on the electrical conductivity and the electric and magnetic field strengths. To illustrate the behavior of the one-dimensional model in the hypersonic regime, the first results shown assume no ionization or recombination is occurring in the channel. To provide MHD interaction, the electrical conductivity is set to a constant $\sigma = 500\ \Omega^{-1}\mathrm{m}^{-1}$.

Following the discussion in Chapter 3, the magnetic interaction parameter will be low for hypersonic high-density flows (low altitudes). Thus, for the sake of this discussion, the inlet conditions are based on Mach 5 flight at a freestream temperature and number density corresponding to 20 km conditions. At these conditions, the Hall effect is not expected to significantly reduce the effective electric field strength. It is unlikely, however, that the vehicle's geometry would not alter the core flow in the MHD channel. The leading edges of the engine's inlet will form oblique shock waves such that the flow will experience deceleration as it passes through the inlet. Therefore, to calculate more realistic inlet conditions, the flow is assumed to pass through two oblique shock waves generated by 7° wedges. Using these assumptions, the boundary conditions used at the inlet of the MHD accelerator are $M_{in} = 3.26$ and $u_{in} = 1285$ m/s. These choices are meant to reflect realistic hypersonic vehicle geometries and provide more physically accurate inlet conditions. However, changes in these assumptions do not alter the conclusions made from the following analyses.

Suppose the magnetic field strength is set to $B = 1$ T throughout. In that case, any supersonic MHD accelerator's target electric field strength must lie between $E_3 = 1.28$ kV/m and$E_1 = 3.20$ kV/m, as dictated by the characteristic velocities outlined in Section 3.1. To begin this discussion, the electric field strength and cross-sectional area are held constant for the entire channel length to highlight the phenomenological behavior of MHD accelerated hypersonic channel flows.

Figures 4.6a and 4.6b show several velocity and temperature profiles for electric field strengths in the range between E_1 and E_3. Smooth acceleration occurs for each electric field strength, but total acceleration increases with increasing electric field strength. However, for the strongest electric field shown, $E = 3000$ V/m, it can be seen that the acceleration in the first half of the channel is less than that for the other electric field strengths. Instead, the flow is significantly heated to just under 4500 K, and the Mach number decreases until it approaches approximately Mach 1.5. For the $E = 1500$ V/m case, the velocity only increases by 100 m/s but also experiences virtually no heating, highlighting that electric fields near E_3 are efficient but ineffective at generating thrust.

Figure 4.6b shows the high temperatures resulting from this heating, especially for the larger electric fields. In the present analysis, the energy added to the flow via the applied electric fields either accelerates the flow or excites the translational energy of each species. Thus, when the flow is not accelerating, the entire electromagnetic deposition term is directed toward the heating mode, leading to high temperatures. The partition of the total energy spent on Joule heating can also be seen on the right-hand side of Eq. (2.76) and noting that it can be rewritten with Eq. (2.77).

$$jE = \frac{j^2}{\sigma} + ujB \tag{4.4}$$

The first term in Eq. (4.4) is known as Joule heating, and the second is the energy added or removed through the work done by the Lorentz force. Thus, it is noted that these two mechanisms affect the total energy of a flow through an MHD accelerator to a varying degree, depending on the operating conditions. The Lorentz efficiency which is defined later in this chapter describes the balance of the two. Joule heating typically leads to an adverse pressure gradient that counteracts the Lorentz force acceleration and decreases total acceleration, especially in the upstream region of the channel. Figure 4.6c shows the pressure profiles for each electric field strength. The adverse pressure gradient formed in the $E = 3000$ V/m cases illustrates how electric fields near E_1 decrease Lorentz efficiency by depositing more energy into Joule heating than acceleration.

The velocity-Mach number contours in Fig. 4.6d illustrate the qualitative relationship between heating and acceleration. For each case except for the $E = 1500$ V/m case, the Mach number initially decreases due to Joule heating. Then the flow accelerates with an increasing Mach number in qualitative agreement with the theoretical predictions above. However, since the $E = 1500$ V/m case is very close to the characteristic electric field $E_2 = 1555$ V/m, the flow is accelerated without the initial heating. Thus, when designing a hypersonic MHD accelerator prototype such as the PFE, it is crucial to consider the total heating in addition to acceleration. It becomes increasingly difficult to achieve high thrust without Joule heating as the Mach number increases in a constant-area, constant-electric field channel.

Joule heating can be seen as an inevitable consequence of using strong electromagnetic fields to accelerate a hypersonic flow. However, exceedingly high temperatures should naturally be avoided. Otherwise, not only would the heat fluxes at the walls be extreme, but the electron

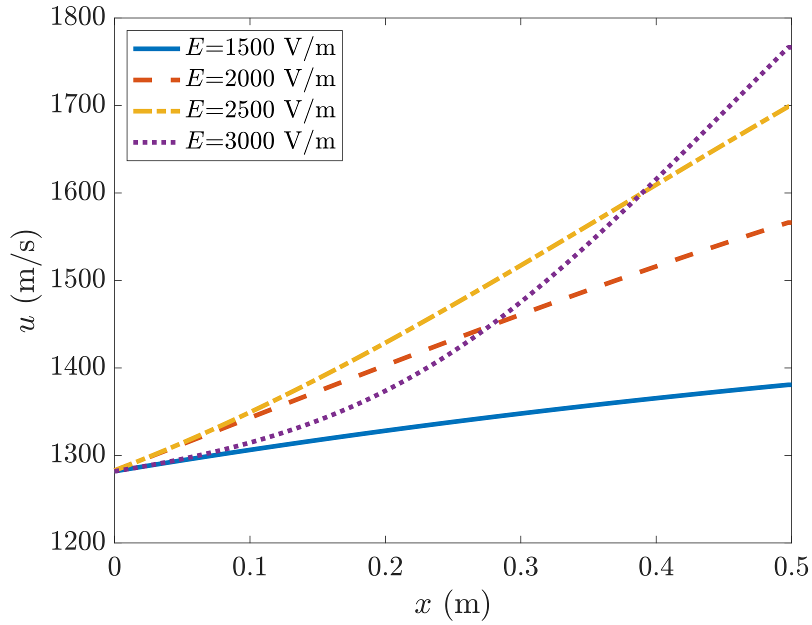

(a) **Velocity profiles.**

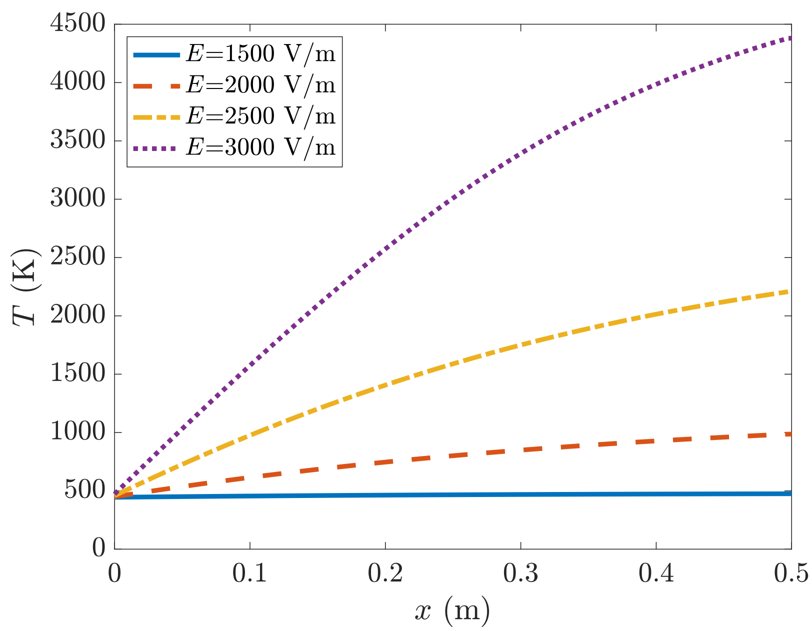

(b) **Temperature profiles.**

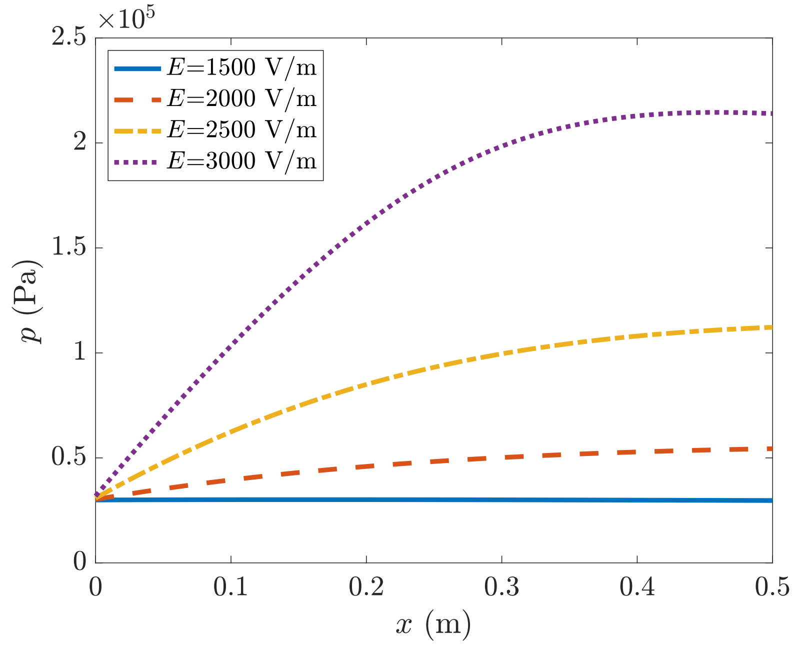

(c) **Pressure profiles.**

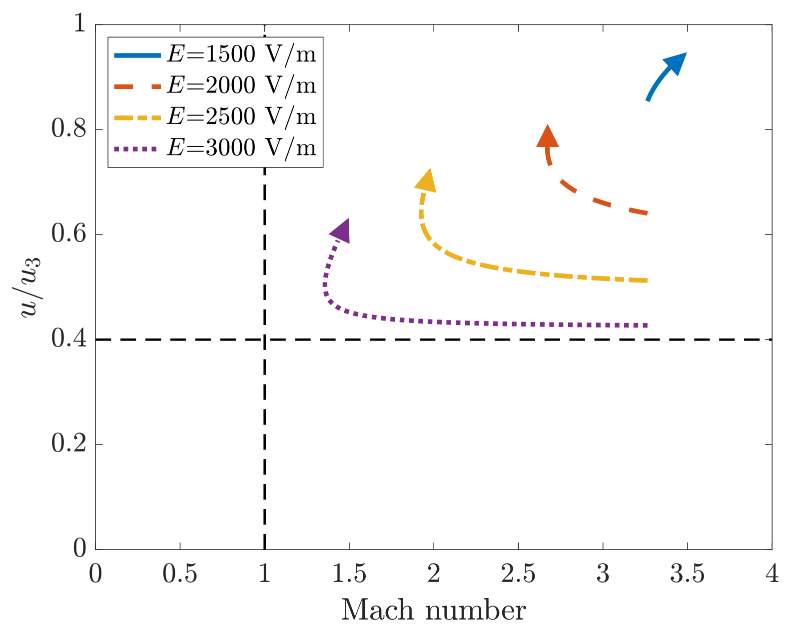

(d) **Velocity versus Mach number diagram.**

Figure 4.6: **One-dimensional constant area PFE flow solutions.**

populations would no longer be primarily controlled by the electron beam region, causing large conductivities in the boundary layers if the temperatures were high enough to cause thermal ionization. The results here qualitatively illustrate the consequence of Joule heating and suggest that any realistic PFE design needs to consider the high temperatures that may occur.

Two main approaches can be used to combat the high temperatures in a hypersonic MHD accelerator. The first is by increasing the cross-sectional area as the flow travels downstream. The second involves using variable electric fields and, by doing so, keeping the applied field near the characteristic E_3 value.

The advantages of the first approach are shown in Fig. 4.7 for various degrees of expansion angles of the duct, θ, in degrees. The $\theta = 0°$ case represents the constant cross-sectional area case. As the cross-sectional area increases, the flow is allowed to expand, leading to improved acceleration and lower temperatures. Although the present model does not account for boundary layer separation and subsequent oblique shock formation, this study shows the qualitative relationship between cross-sectional area divergence to peak temperatures at a constant electric field strength. The operating conditions are chosen to be the same as above, Mach 5 flight at freestream conditions equivalent to 20 km altitude. Again, the flow is assumed to decelerate due to a series of oblique shock waves upstream of the inlet to the computational domain. The $E = 2500$ V/m case is chosen as the baseline case, and only the channel expansion angle varies from solution to solution.

Velocity profiles in Fig. 4.7a show the effect of flow expansion on total acceleration. As the channel expands more rapidly, the total acceleration increases. For the highest expansion angle, $\theta = 15°$, the velocity approaches the upper limit for this electromagnetic field configuration, $u_3 = 2500$ m/s. It is noted that expanding the channel by 5° increases the outlet velocity by over 300 m/s compared to the constant-area case.

Temperature profiles are given in Fig. 4.7b. The temperature gradient in the upstream portion of the channel is nearly identical for each geometry. This is because the flow must go through a heating phase before acceleration occurs for this electric field strength, which implies that the electric field at the start of the channel is too high for optimal performance at this particular condition. However, the length of the heating region decreases with increasing expansion angle. Similarly, the peak temperatures decrease with more expansion. The most drastic change can be seen between the $\theta = 0°$ and the $\theta = 5°$ cases, where the peak temperature decreases by approximately 600 K. Peak temperatures of 2000 K may be high for design considerations, depending on the material properties of the walls and electrodes, but they are still within the range of temperatures that occur in scramjet operation [98]. These solutions show how performance can be improved by allowing the cross-sectional area to increase.

The increase in total acceleration for the expanding channels is primarily due to the decrease in adverse pressure gradients formed by Joule heating. Figure 4.7c shows the decreasing pressure gradients as a function of channel expansion. In fact, the pressure gradient even becomes favorable with respect to flow acceleration for the higher expansion cases. Again, the most significant changes between the $\theta = 0°$ and $\theta = 5°$ cases show that modest expansions could lead to appreciable benefits in PFE performance.

Finally, Fig. 4.7d shows the velocity versus Mach number diagrams for each geometry. The discussion above regarding the relationship between Joule heating and acceleration is clear when inspecting the behavior of the flow solutions in Mach number versus velocity space. As the channel expands more rapidly, the total heating and thus decrease in Mach number is decreased. Therefore, the flow can accelerate earlier in the channel for increasing cross-sectional areas.

In addition to increasing cross-sectional areas, variable electric fields can increase total acceleration while minimizing total heating. Namely, by setting the electric field at the inlet just greater than E_3 and strengthening it as the flow accelerates down the channel, PFE efficiency can be increased. From the engineering perspective, this can be achieved by separately conditioning electrodes or sets of electrodes such that the transverse electric field increases with axial distance.

The effect of using both a diverging channel and an increasing electric field can be observed in Figs. 4.8 and 4.9 which show velocity, Mach number, temperature, and pressure profiles. These solutions are for a channel with an expansion angle of $\theta = 10°$ and the same inlet conditions as used for the cases plotted in Figs. 4.6 and 4.7. The inlet velocity due to the assumed oblique shocks upstream of the inlet is approximately 1281 m/s, so the electric field at the inlet is prescribed to be 1500 V/m. Since a constant electric field at this value would lead to a low total acceleration, the electric field must be increased downstream. In this analysis, the electric field is linearly increased from 1500 V/m at the inlet to 3000 V/m at the outlet.

Figure 4.8 shows the velocity profile on the left axis and the Mach number profile on the

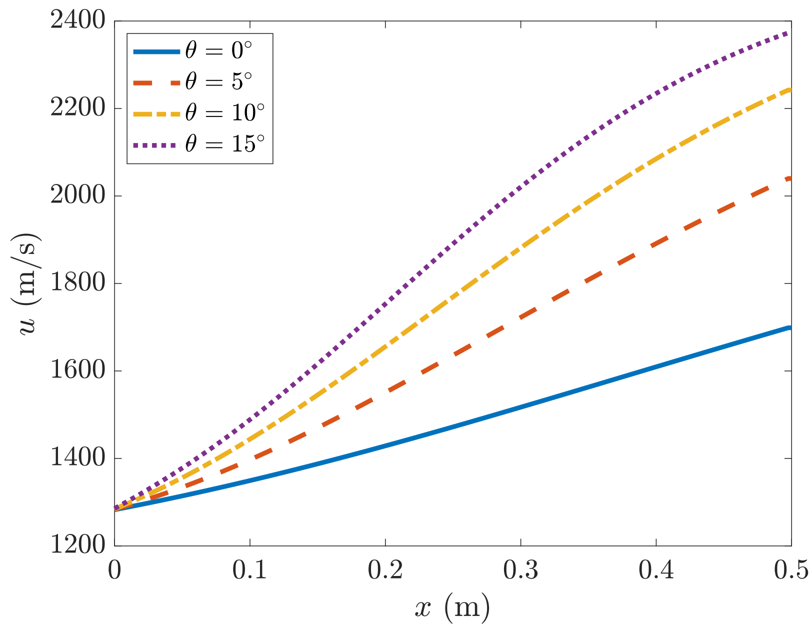

(a) **Velocity profiles.**

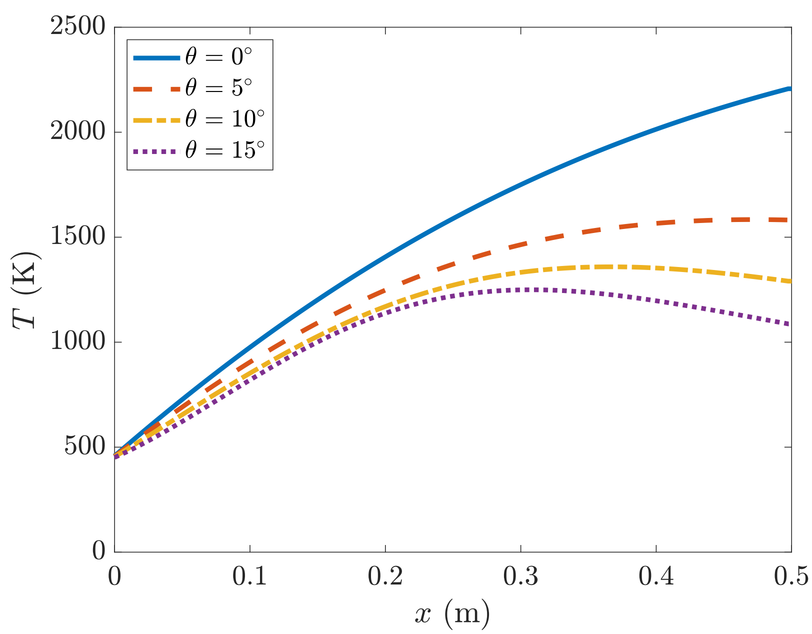

(b) **Temperature profiles.**

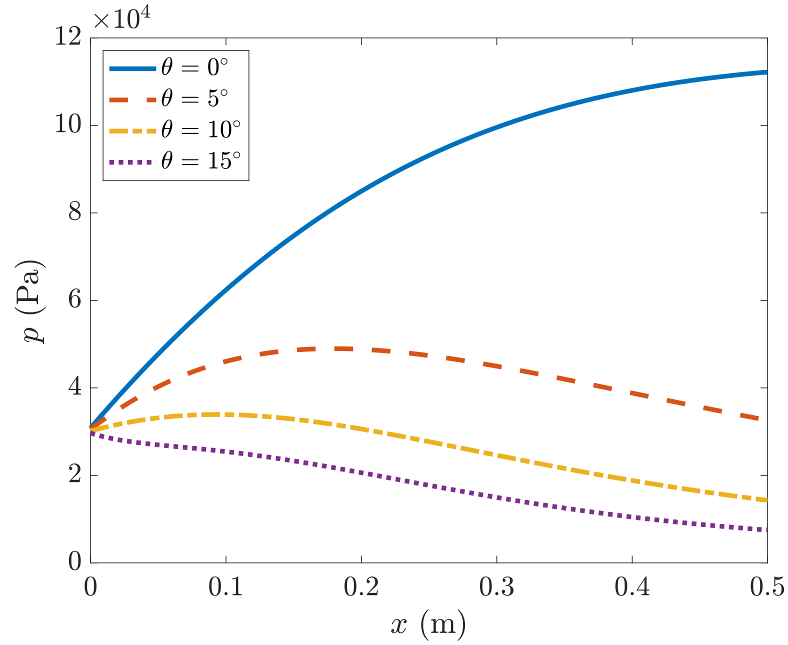

(c) **Pressure profiles.**

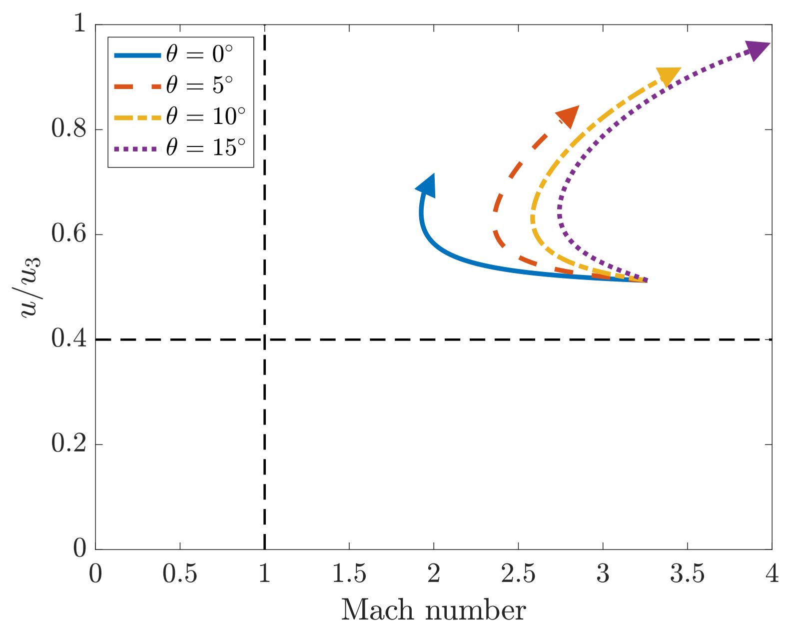

(d) **Velocity versus Mach number diagram.**

Figure 4.7: **One-dimensional variable area PFE flow solutions.**

right axis. The velocity increases by more than 70% from the inlet to the outlet. Meanwhile, the Mach number shows an initial increase due to flow acceleration and cooling, followed by a decrease

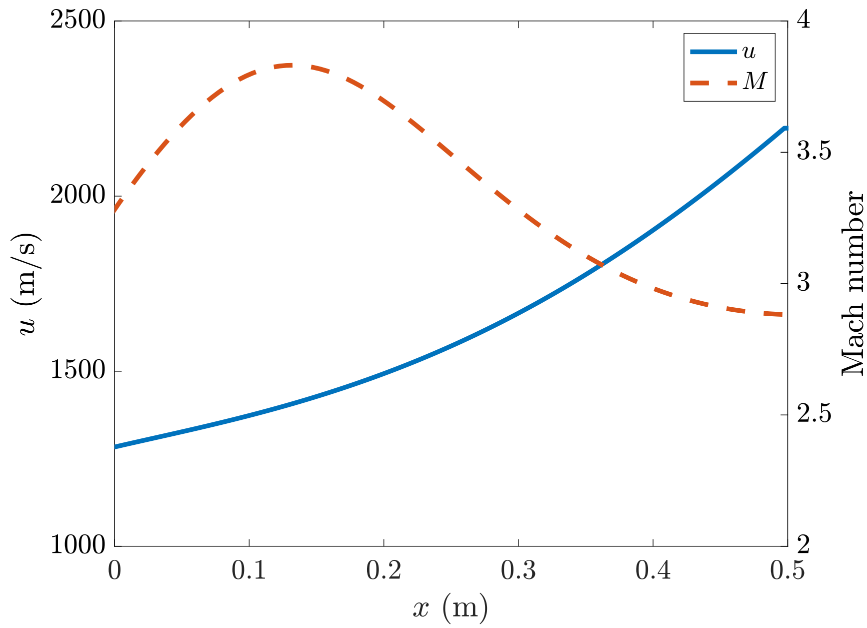

Figure 4.8: **Velocity and Mach number profiles with a variable electric field.**

to Mach 2.9 at the outlet, even though the flow continues to accelerate.

Figure 4.9 shows the expanding channel's corresponding temperature and pressure profiles with a ramped electric field. With this selection of channel geometry and electric field configuration, a greater acceleration is seen than for the constant-area and 3000 V/m case in Fig. 4.6b while keeping the peak temperature near 1500 K showing how performance and efficiency can be improved through these two design strategies.

The pressure profile reveals that while the flow initially expands with a favorable pressure gradient, a slight pressure rise is seen downstream due to Joule heating. This behavior indicates that the electric field selection could be improved for these conditions to achieve higher Lorentz efficiencies. By comparing the velocity, Mach number, temperature, and pressure profiles, it can be discerned that the electric field is increased too rapidly for optimal performance. By ramping the electric field strength more gradually, the heating could be reduced while maintaining thrust. Finally, it is noted that continued acceleration could be achieved through thermal expansion downstream of the MHD accelerator portion of the engine by adding a nozzle.

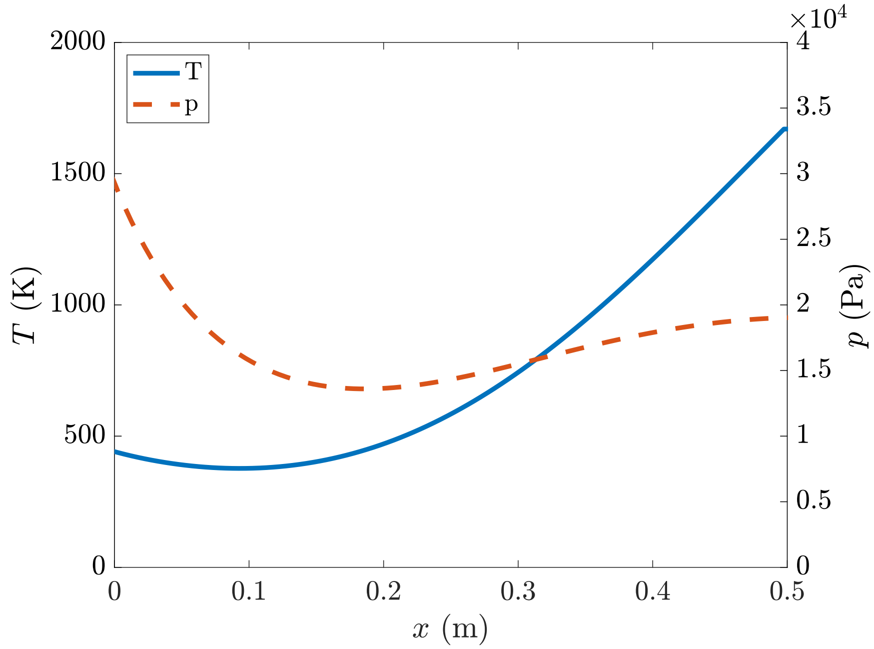

Figure 4.9: **Temperature and pressure profiles with a variable electric field.**

More optimal PFE configurations are likely attainable. However, a complete design optimization study is beyond the scope of this work. Instead, a constant area duct with a constant electric field was used to illustrate the fundamental behavior of flows in the MHD accelerator portion of a PFE. Namely, as the electric field strength increases for a fixed inlet velocity and inlet Mach number, more of the applied electromagnetic energy is deposited into the heating mechanism relative to the acceleration mechanism. Then, it was shown that significant acceleration could be achieved using an MHD accelerator onboard a hypersonic vehicle while keeping peak temperatures manageable by leveraging variable area ducts and variable electric fields.

4.3 Plasma Chemistry and Transport Property Modeling for Argon

The discussion thus far has illuminated the relationship between the applied electromagnetic field and the macroscopic flow behavior in an MHD accelerator. However, several limiting assumptions have been made, such as constant electrical conductivity and small Hall parameters. While a Hall parameter $\beta_e \leq 1$ may be reasonable for conditions corresponding to 20 km and lower provided that the electrons are kept sufficiently hot, constant ionization is not.

The results from the one-dimensional model in Section 2 agree with the theoretical predictions made by Culick and Resler and Sears, as was shown in [99]. However, before the one-dimensional theory can produce valuable insight for PFE design, it is critical to understand how including additional physics, such as nonuniform conductivity, thermal nonequilibrium, external ionization, and the Hall effect, affects the results predicted by the theory.

A model is presented here for the electron mobility of the plasma, μ_e, which can be used to calculate electrical conductivity and electron Hall parameters. The curve fits for mobility are derived from solutions to the Boltzmann equation using BOLSIG+ [71]. Typically, electron mobility is a function of electron temperature. However, in this model, the electron mobility is assumed to be solely a function of the reduced electric field, $\frac{E'}{N} = \frac{|E-uB|}{N}$, since the system of equations in the one-dimensional model does not explicitly compute mean electron energy. Along with collision cross-section data, BOLSIG+ requires plasma temperature, density, and degree of ionization. For a gas temperature of $T = 300$ K, number density of $N = 1 \times 10^{25}$ m^{-3}, and degree of ionization of $\alpha = 1 \times 10^{-3}$, electron mobility and mean electron energy are computed as a function of reduced electric fields ranging between 0.001 Td and 300 Td and are shown in Fig. 4.10.

Note that BOLSIG+ outputs the reduced mobility, $\mu_e N_0$, where N_0 is the total number density used in the calculations. Then, to find the mobility for a different density, N, the electron mobility is computed as $\mu_e = \mu_e N_0/N$. Thus, the mobility and energy curves in Fig. 4.10 can be interpreted as the values at $N = 1 \times 10^{25}$ m^{-3}. For these conditions, there is a discontinuity in electron mobility that occurs at approximately 0.4 Td. At this reduced electric field strength, the mean electron energy is $\epsilon \approx 0.23$ eV, which corresponds to the Ramsauer-Towsend minimum, that occurs for low energy electrons in noble gases [100]. At this electron energy, the collision-cross section reaches a minimum, meaning that the probability of collisions with argon atoms is at its lowest. Unfortunately, this means that two curve fits are needed to arrive at an electron mobility model. The first curve fit is for 0.001 Td to 0.4 Td, and the second is from 0.4 Td to 300 Td.

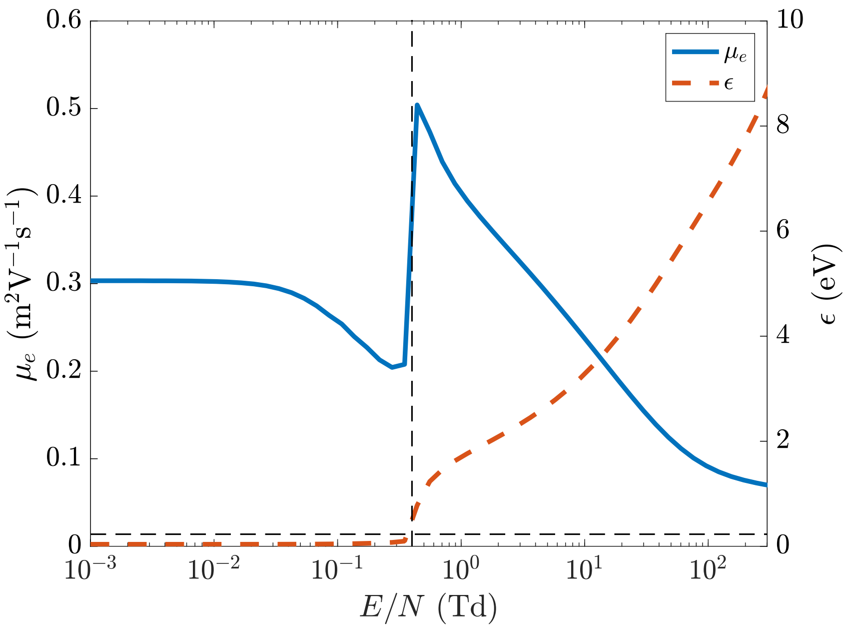

Figure 4.10: **Electron mobility and mean electron energy as a function of reduced electric field.**

$$\mu_e N_0 = C_1 \exp\left(C_2 \frac{E'}{N}\right) + C_3 \exp\left(C_4 \frac{E'}{N}\right) \tag{4.5}$$

The coefficients in Eq. (4.5) are given in Table 4.1 for reduced electric fields between 0.001 Td and 0.4 Td and between 0.4 Td and 300 Td[1] . The Normalized Root Mean Square Error (NRMSE) is 4.87% for the former curve fit and 0.81% for the latter, where NRMSE is defined in Eq. (4.6).

$$NRMSE = \frac{1}{\bar{y}} \sqrt{\sum_{i=1}^{n} \frac{(\hat{y} - y)^2}{n}} \tag{4.6}$$

Since electrical conductivity and electron Hall parameters are functions of electron mobility, it is a crucial variable to model accurately. Electrical conductivity, given in Eq. (4.7), is directly proportional to the electron mobility and the electron number density of the plasma.

$$\sigma_e = q_e n_e \mu_e \tag{4.7}$$

[1] The coefficients in Table 3.1 are as follow: ^{a}m^{-1}V^{-1}s^{-1} / ^{b}Td^{-1} / ^{c}cm^{3}s^{-1}Td$^{-0.18}$ / ^{d}Td / ^{e}Td^{2} / ^{f}Td^{3} / ^{g}eV^{1}Td$^{-0.2072}$ / ^{h}Td^{4}

Table 4.1: Curve fit coefficients for plasma chemistry models.

Eq.	C_1	C_2	C_3	C_4	C_5	C_6
(4.5): 0.001-0.4 Td	2.308×10^{24} [a]	-0.136 [b]	1.919×10^{24} [a]	-0.008 [b]		
(4.5): 0.4-300 Td	3.096×10^{24} [a]	-2.074 [b]	2.085×10^{22} [a]	9.56 [b]		
(4.13)	6.36×10^{-10} [c]	0.18	-281.15 [d]	1.54×10^{-3} [e]	-4.94×10^{-3} [f]	
(4.14)	1.7227 [g]	0.2072	3.9087 [d]	-15.2098 [e]	20.978 [f]	-10.0568 [h]

In this work, ion mobility is expected to be much lower than electron mobility since the plasma is collisionally dominated, and the ions are much more massive than the electrons. Consequently, only electron transport properties are considered, and ion slip is neglected. The electron Hall parameter is the second plasma transport property that is a function of electron mobility, shown in Eq. (4.8).

$$\beta_e = \mu_e B \tag{4.8}$$

For cases where the electron Hall parameter is much less than unity ($\beta_e << 1$), the scalar conductivity given in Eq. (4.7) is adequate since the Hall current is minimal. However, as the electron Hall parameter increases, the free electrons orbit around the magnetic field lines more frequently between collisions with the heavy particles. The generalized Ohm's law in Eq. (3.14) can then be used to give two current density components to account for the Hall effect.

$$j_x = \frac{\sigma_e}{1+\beta_e^2}(E_x + \beta_e(E_z - uB_y)) \tag{4.9}$$

$$j_z = \frac{\sigma_e}{1+\beta_e^2}(-\beta_e E_x + E_z - uB_y) \tag{4.10}$$

Equation (4.9) gives the axial component of current density, which is parallel to the bulk velocity. Equation (4.10) gives the transverse component, which is in the direction of the applied electric field. While the one-dimensional model does not account for the conservation of momentum in the z-direction, which accounts for the $j_x B_y$ Lorentz force, it is assumed that the electric field configurations will be designed such that $j_x < j_z$ in accordance with the discussion at the end of Chapter 3. While the set of governing equations is incomplete in this sense, it is also still very useful to gauge the Hall effect's impact on electrical conductivity and, thus, PFE performance. For moderate Hall parameters, Faraday configuration accelerators may be able to provide efficient thrust if the electrodes are properly segmented. However, details of electrode segmentation and non-axial thrust effects are left to a higher-dimensional analysis.

Although this chapter focuses on flows utilizing argon, the corresponding plasma chemistry models can be evaluated for other systems, such as air, using the appropriate coefficients in the curve fits. The freestream argon is ionized in the electron beam region according to the reaction given in Eq. (4.11)[2] .

$$\begin{gathered} Ar + e_b^- \rightarrow Ar^+ + e^- + e_b^- \\ k_{ebi} = \Omega_0 \left(\frac{\epsilon_0}{\epsilon_b}\right)^a \frac{j_b}{q_e} \left[\frac{1}{s}\right] \end{gathered} \tag{4.11}$$

The ionization rates in the electron beam region upstream of the MHD accelerator portion of the PFE are a function of the electron beam energy ϵ_b, electron beam current density j_b, and number density of the gas. The electron beams are assumed to be of high enough energy that the beam electrons do not lose significant energy to the core flow and thus collect on the opposite side of the channel. According to this assumption, the electron beam electrons are not tracked as a separate species, nor is an additional equation solved for the electron beam energy. See Table 4.2 for the constants used in Eq. (4.11). Additionally, energy from the electron beam is deposited into the system equal to the ionization energy for every new argon ion created and is accounted for using a source term in Eq. (2.76).

Table 4.2: Electron beam ionization constants in Eq. (4.11).

Ω_0	ϵ_0	a
8.6×10^{-17} cm^2	1 keV	0.9

In the main PFE channel, the free electrons are accelerated via the applied electric field and generate new ion-electron pairs through collisions with neutral atoms. An effective electric field is

[2] The electron beam ionization models in this section were graciously generated and provided by the Non-Equilibrium Thermodynamics Laboratory (NETL) led by Dr. Igor Adamovich at The Ohio State University.

used to compute this ionization rate, accounting for the reduction in electric field strength by a transverse magnetic field, where $E_{\perp}$ is the electric field strength in the direction transverse to the magnetic field.

$$\frac{E'_{eff}}{N} = \frac{1}{N}\sqrt{\frac{E_{\perp}^2}{1+\beta_e^2}} \tag{4.12}$$

The external field ionization rate is also taken as a function of the electric field strength and is given in Eq. (4.13). Similarly to Eq. (4.5), BOLSIG+ curve fit coefficients can be found in Table 4.1 for effective reduced electric fields between 1 Td and 300 Td.

$$Ar + e^- \rightarrow Ar^+ + e^- + e^-$$
$$k_{exi} = C_1 \left(\frac{E'_{eff}}{N}\right)^{C_2} \exp\left(\frac{C_3}{\left(\frac{E'_{eff}}{N}\right)} + \frac{C_4}{\left(\frac{E'_{eff}}{N}\right)^2} + \frac{C_5}{\left(\frac{E'_{eff}}{N}\right)^3}\right)\left[\frac{cm^3}{s}\right] \tag{4.13}$$

Electron recombination is assumed to occur as a function of the local electron temperature. Since the conservation of electron energy equation is not included in this model, an equation for electron temperature is given below as a function of the effective reduced electric field in Eq. (4.14) [71][3] . The coefficients in Eq. (4.14) are listed in Table 4.1 for reduced electric fields between 1 Td and 300 Td.

$$T_e = C_1 \left(\frac{E'_{eff}}{N}\right)^{C_2} \exp\left(\frac{C_3}{\left(\frac{E'_{eff}}{N}\right)} + \frac{C_4}{\left(\frac{E'_{eff}}{N}\right)^2} + \frac{C_5}{\left(\frac{E'_{eff}}{N}\right)^3} + \frac{C_6}{\left(\frac{E'_{eff}}{N}\right)^4}\right)[eV] \tag{4.14}$$

Figure 4.11 shows electron temperature for reduced electric fields between 1 Td and 100 Td. For reduced electric fields less than 10 Td, the electron temperature increases rapidly to above $40,000$ K. When electron temperatures are high, the collision frequency with positively charged argon ions decreases, and recombination is slow. Conversely, when the free electrons are relatively cool, they will combine with the ions much faster. Three-body recombination is modeled using the reaction rate given in Eq. (4.15) [101].

[3] Courtesy of the Non-Equilibrium Thermodynamics Laboratory (NETL) led by Dr. Igor Adamovich at The Ohio State University.

$$\begin{gathered} Ar^{+} + e^{-} + e^{-} \rightarrow Ar + e^{-} \\ k_{3br} = 5 \times 10^{-27} \left(\frac{1}{T_e}\right)^{4.5} \left[\frac{cm^6}{s}\right] \end{gathered} \tag{4.15}$$

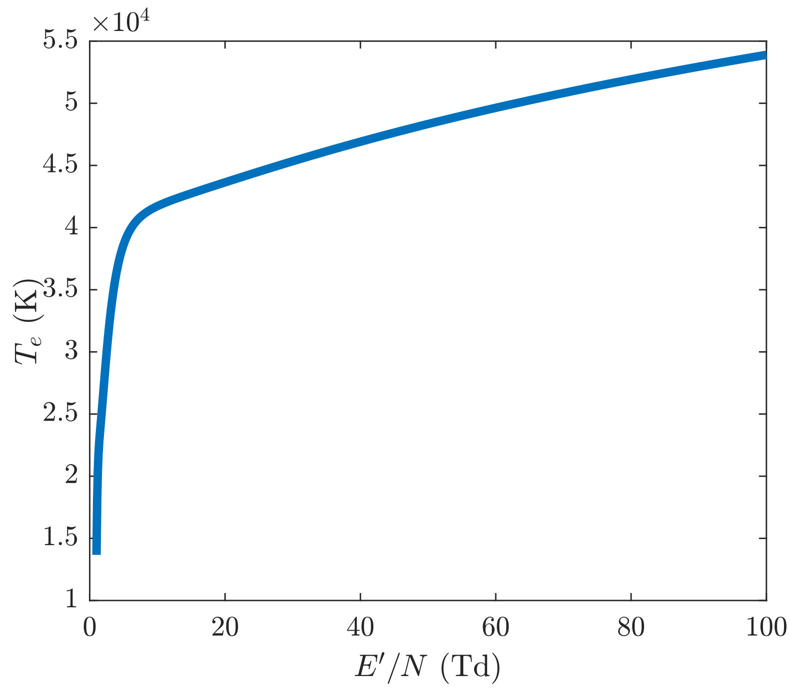

Figure 4.11: **Electron temperature as a function of reduced electric field.**

In addition to three-body recombination, argon ions and electrons recombine through the formation and subsequent dissociative recombination of molecular argon ions [102]. Ion conversion, the first step in this recombination mechanism, is modeled using Eq. (4.16) [103].

$$\begin{gathered} Ar^{+} + Ar + Ar \rightarrow Ar_2^{+} + Ar \\ k_{ic} = 2.5 \times 10^{-31} \left[\frac{cm^6}{s}\right] \end{gathered} \tag{4.16}$$

The second step, dissociative recombination of molecular argon ions, is modeled using Eq. (4.17) [104]. The two-step recombination process is expected to be the dominant pathway for electron-ion recombination for weakly-ionized plasmas when the electron number densities are low. Furthermore, dissociative recombination occurs rapidly once ion conversion has taken place, so the concentration of molecular argon is kept low relative to the atomic species.

$$
\begin{gathered}
Ar_2^+ + e^- \rightarrow Ar + Ar \\
k_{dr} = 7.3 \times 10^{-8} \left(\frac{1}{T_e} \right)^{0.67} \left[\frac{cm^3}{s} \right]
\end{gathered}
\tag{4.17}
$$

4.4 Electron Beam and External Ionization, Recombination, and Electrical Conductivity

Now that solutions to the governing equations have been explored for flows with a constant electrical conductivity, the influence of electron beam ionization, external ionization, and recombination is considered. In addition, the plasma transport property models in the preceding section are used to perform simulations with the Hall effect and electron nonequilibrium. The freestream gas is initially ionized via an electron beam placed just upstream of the accelerator portion of the engine. As newly formed ion-electron pairs convect into the MHD accelerator, they gain energy from the applied electric field and begin to orbit around the magnetic field lines, only interrupted by collisions with other particles.

Sustaining significant electron populations is critical to operating any MHD energy converter such as the PFE. In the absence of thermal ionization, the degree of ionization of the argon in the channel is controlled by electron beam ionization, electric field-induced ionization, recombination, and convection. Thus, electron beam power, electron beam current density, electric field strength, and flow residence time in the channel are all needed to compute ionization estimates for different operating conditions. This analysis assumes a Mach 5 freestream flow that is decelerated in the engine inlet upstream of the MHD accelerator. Since the inflow will still be greater than Mach 1, the applied electric field must be greater than E_3 to achieve smooth acceleration. Consequently, for the purposes of this discussion, the electric field is prescribed such that $E = 2E_3$. Furthermore, the magnetic field strength is still assumed to be $B = 1$ T.

Since the freestream density decreases as altitude increases, the minimum reduced electric field required for acceleration increases. Thus, as freestream density decreases, recombination is slower, and electric field induced ionization increases. For each mechanism, the different altitude conditions correspond to the appropriate values of freestream temperature and number densities. The applied electric field strengths, reduced electric field strengths, and effective reduced electric field strengths (that account for the magnetic field) needed to satisfy the $E = 2E_3$ constraint are listed in Table 4.3 for Mach 5 freestream flow across a range of altitude conditions.

Table 4.3: Electric field strengths for altitudes ranging from 0 km to 50 km.

Alt. (km)	E (V/m)	E/N (Td)	E/N_{eff} (Td)
0	2955	0.022	0.022
10	2601	0.057	0.056
20	2563	0.26	0.24
30	2621	1.3	0.33
40	2759	6.5	0.49
50	2439	16	0.63

It is assumed that the electron beams produce 100 keV electrons. However, it is expected that the beam electrons would lose approximately half their energy to the foil, so 50 keV is used to calculate the electron beam ionization rate in Eq. (4.11). Furthermore, the electron beam current density is 0.1 mA/cm^2, within the limits of current electron beam technology [105]. Furthermore, it is assumed that the electron beam region only spans ≈ 1 mm since the spot sizes of the beams are typically in this range, while the channel length is 1 m. Assuming the flow velocity is ≈ 1000 m/s, the residence time in the electron beam region is prescribed to be 1×10^{-6} seconds, and the residence time in the entire channel is 1×10^{-4} seconds. The degree of ionization is plotted in Fig. 4.12 for each altitude condition using these representative time scales and freestream conditions.

Electron beam ionization is the dominant mechanism for all altitude conditions in the regions where it is applied. In this modeling, the electron beam ionization is controlled by the electron beam current, power, and freestream number density. Since the electron beam parameters are held constant for each altitude condition, the degree of ionization varies with the freestream number density. An initial baseline ionization is formed for each case that scales with altitude. However, as the flow convects through the electron beam region, ionization becomes a function of the secondary ionization and recombination mechanisms.

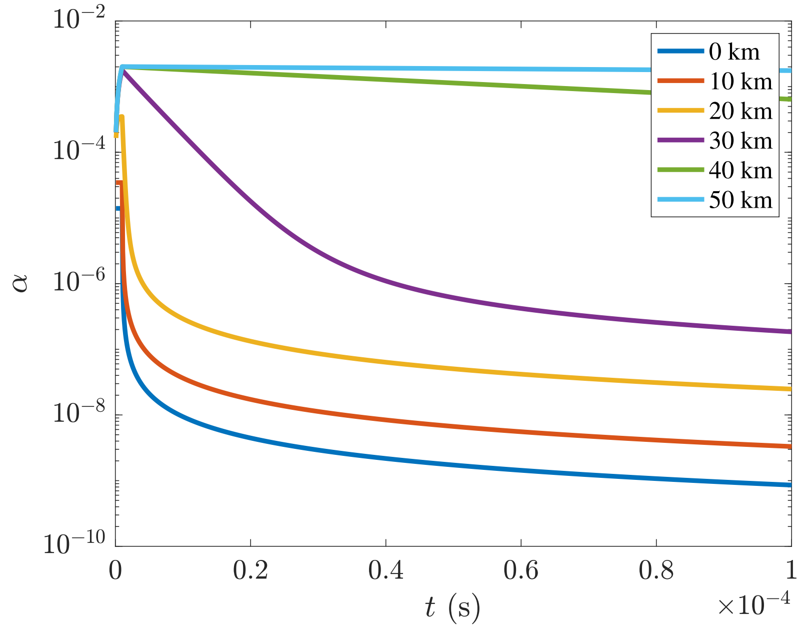

Figure 4.12: **The degree of ionization in a representative channel geometry for several altitude conditions.**

The secondary ionization is not strong enough for the lower altitude cases to offset the recombination. Downstream in the channel, Ar_2^+ is formed and rapidly destroyed through dissociative recombination such that the degree of ionization decreases down the length of the channel and the molecular ion species population remains low. However, three-body recombination plays a more important role in the higher 40 km and 50 km cases when the free electrons and argon ions become more abundant. Without sustained electron beam ionization, the degree of ionization cannot remain high for the 0-30 km cases. For the 40 km and 50 km cases, recombination does not significantly reduce the degree of ionization throughout the channel. This analysis suggests that multiple electron beams placed along the length of the channel will be required to sustain the ionization necessary for flow acceleration for altitudes less than 40 km. Furthermore, larger electron beams capable of supporting more current would be necessary to achieve ionization levels above $\alpha = 1 \times 10^{-4}$ for the lowest altitude cases.

4.4.1 One-Dimensional Solutions with the Hall Effect

Using the models in the preceding section, the consequences of ionization, recombination, and the Hall effect on the one-dimensional solutions are provided. Mach 5 flow at 40 km altitude is chosen to facilitate the discussion of these models and their consequences. The inlet velocity and Mach number are assumed to be approximately 1400 m/s and 3.5 due to oblique shock wave deceleration. For a magnetic field of 1 T, a transverse electric field of $E_z = 1400$ V/m would initially offset the induced field. However, subsequent acceleration would induce an electric field in the opposite direction of the field in a Faraday configuration channel. Applying an axial field that leverages the Hall effect ensures that acceleration still occurs.

Figure 4.13 gives the solutions in velocity versus Mach number space for $E_z = 1400$ V/m and axial fields from $E_x = 1000$ V/m to $E_x = 4000$ V/m. The flow accelerates in each case with stronger axial fields leading to higher total acceleration. However, the Mach number does not always strictly increase with acceleration. For example, in the $E_x = 1000$ V/m and $E_x = 2000$ V/m cases, the flow accelerates with a corresponding increase in Mach number. However, for the $E_x = 3000$ V/m and $E_x = 4000$ V/m cases, the flow does experience heating before accelerating such that the Mach number initially decreases, similar to the behavior of the curves with E_z near E_1 described earlier in the chapter for ideal Faraday configurations.

Note that the transverse electric field definitions, E_1, E_2, and E_3, do not have the same meaning in an axial electric field context. Setting the transverse electric field to $E = E_3 = u_{in}/B$ will offset the induced field caused by the plasma moving through the magnetic field, but it will not entirely negate the Hall current unless E_x is also set to zero. However, setting the axial field $E_x = 0$ will also result in zero transverse current. Thus, the objective is to maximize transverse current while keeping the axial component as close to zero as possible. In a continuous Faraday accelerator, an axial component of current density is inevitable and is a function of the electric field and the electron Hall parameter. The electron Hall parameters for each case above are plotted in Fig. 4.14.

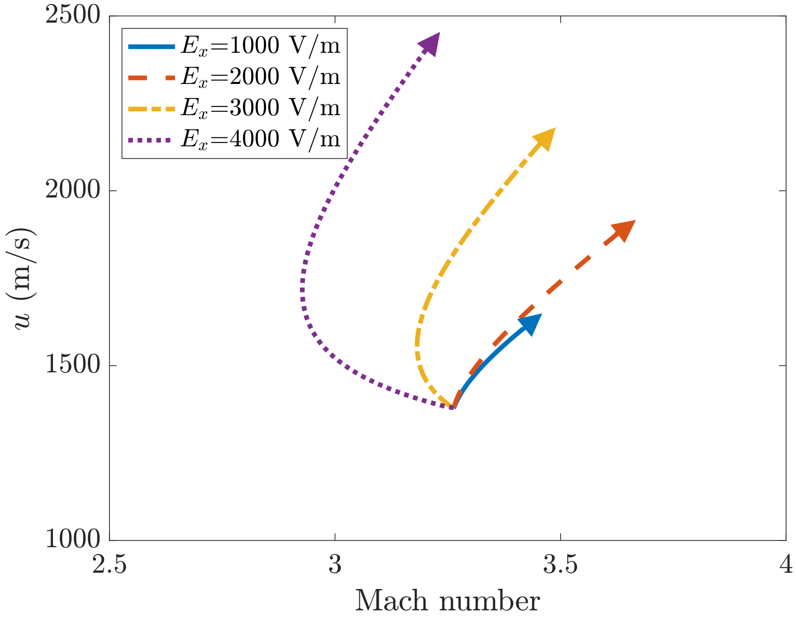

Figure 4.13: **One-dimensional solutions in velocity versus Mach number space including ionization, recombination, and the Hall effect.**

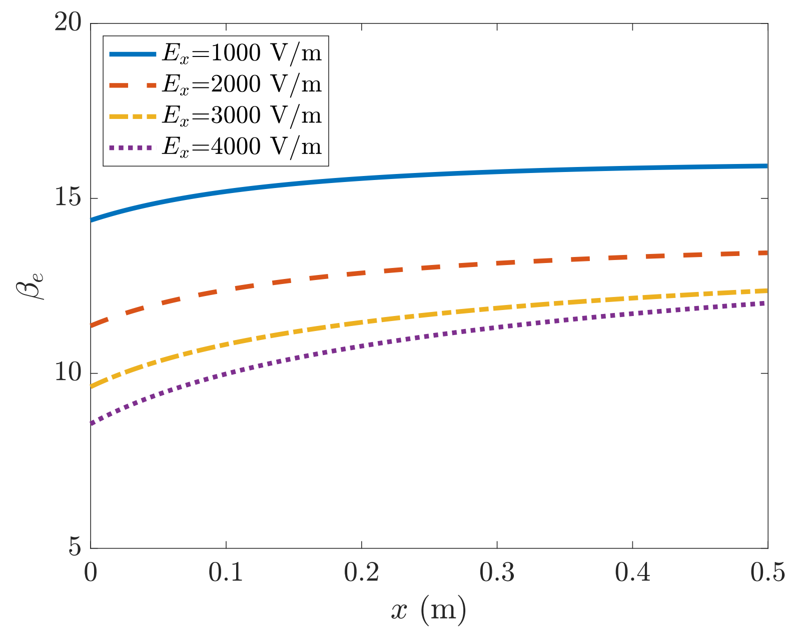

Figure 4.14: **Electron Hall parameters including ionization, recombination, and the Hall effect.**

The Hall parameter varies for each case since it is a function of the electric field strength.

However, it does not vary significantly as a function of distance down the length of the channel since the axial field is held constant. Regardless, the electron Hall parameter varies between approximately 10 and 15 for the $E_x = 4000$ V/m and $E_x = 1000$ V/m cases, respectively. On the other hand, while the Hall parameter increases with decreasing electric field, the degree of ionization increases as the electric field strengthens. The degree of ionization profiles for each axial electric field strength are plotted in Fig. 4.15.

Since the electron beam energy and current density are held constant between each simulation, the electric field strength does not affect the degree of ionization at the inlet. However, the recombination rate controls the electron number density downstream of the inlet. The mean electron energy increases with the electric field strength and, consequently, the degree of ionization. However, the degree of ionization in most of the channel is only decreased by an order of magnitude or less, enabling sufficient conductivity for acceleration. Finally, the electrical conductivity profiles for each electric field strength are given in Fig. 4.16.

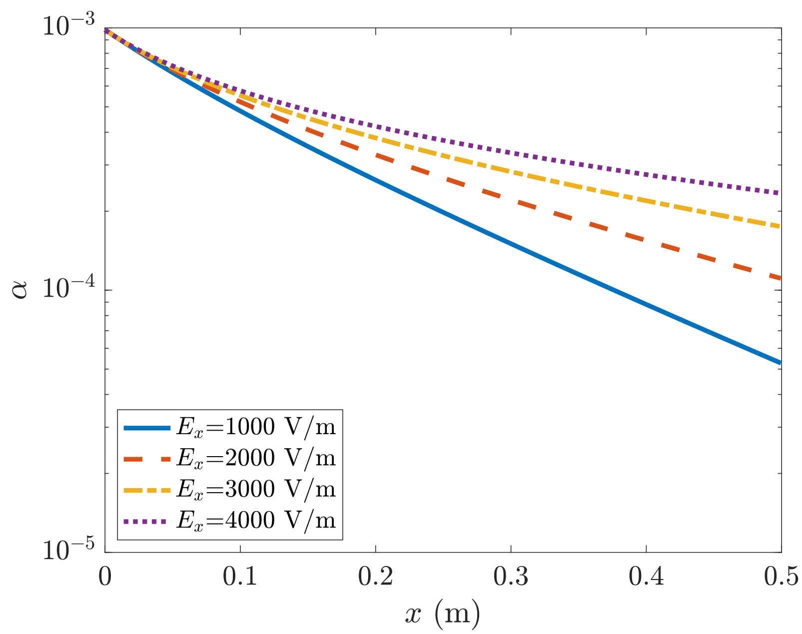

Figure 4.15: **Degree of ionization profiles including ionization, recombination, and the Hall effect.**

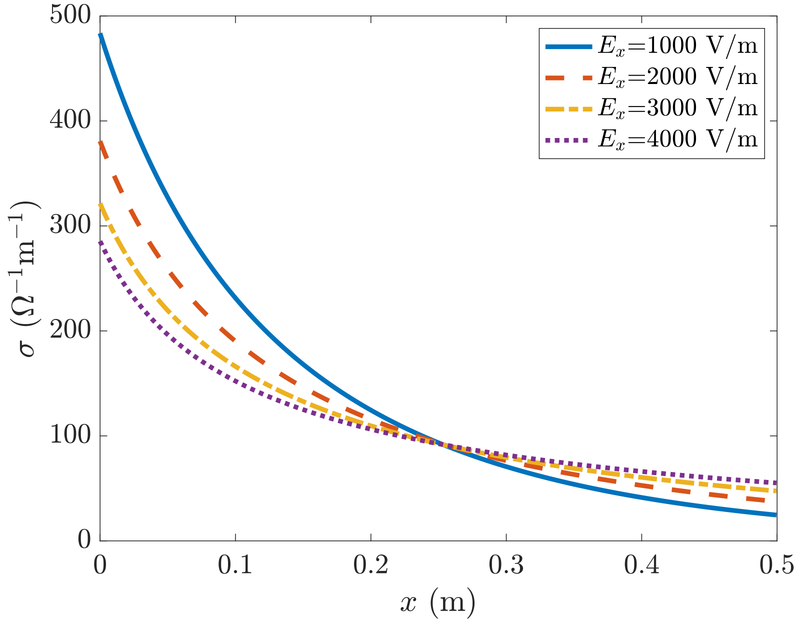

Figure 4.16: **Electrical conductivity profiles including ionization, recombination, and the Hall effect.**

The electron mobility decreases with stronger electric fields for the reduced electric fields at these operating conditions, so the highest conductivity at the inlet is for the cases with the weakest axial electric fields. Then, as the electron populations decay due to recombination, the electrical conductivity also decays. However, as was noted in the degree of ionization profiles in Fig. 4.15, recombination is slower for the stronger electric fields, so the conductivity decreases less for those cases.

The one-dimensional simulations illustrated above exhibit how the plasma chemistry models described in Section 4.3 influence the solutions to the governing equations for various operating conditions. These solutions can inform PFE design and optimal operating envelopes for future simulations and prototypes by accounting for various phenomena, such as ionization and magnetic field effects. Namely, the engine's performance relies not only on the electric and magnetic field strengths but also on the level of recombination and the magnitude of the Hall parameter. Questions about optimal channel geometry, electromagnetic field configuration, and electron beam placement have not been answered. However, it has been demonstrated that the one-dimensional model can be used as a tool to answer these questions for practical systems of interest. Furthermore, the framework stays relatively the same when considering air species. The main difference when extending to molecular species is that the coupling between the vibrational mode and the bound and free electron modes needs to be considered.

4.5 Performance Predictions Using the One-Dimensional Model

Now that the behavior of MHD accelerated flows has been explored for a range of operating conditions and the relevant plasma chemistry and transport models have been identified, the one-dimensional model is used to arrive at performance predictions of electron-beam powered hypersonic MHD accelerators. Since the promise of using electromagnetic body forces to provide thrust lies in high altitude conditions where combustion is difficult, altitudes above or near the air-breathing limit are considered. For this analysis, these conditions represent freestream conditions at 40 km, 45 km, and 50 km, and Mach numbers from 6 to 12. At higher altitudes, low pressures lead to extreme electron Hall parameters. Ion Hall parameters also increase where ion slip can no longer be neglected. In this regime, electrostatic acceleration, where the electrons are effectively trapped by strong magnetic fields and ions are accelerated down the channel to realize thrust, becomes the best candidate for realizing thrust. Eventually, the Knudsen number approaches unity, the continuum assumption breaks down, and particle-based methods are necessary for continued analysis.

When evaluating the feasibility of a novel engine concept, quantifying performance is a critical task, and metrics are needed. Primarily, it is important to determine the proportion of energy being deposited into Joule heating instead of acceleration and the net thrust available for a given electromagnetic configuration. As such, thrust and efficiency are critical indicators when examining the performance of a given MHD channel. Thrust is found through the usual relation for an air-breathing engine. Since vehicle characteristics such as drag and lift coefficients are not available, thrust is non-dimensionalized by the freestream dynamic pressure to determine the coefficient of thrust for a particular engine configuration, as shown in Eqs. (4.18-4.19).

$$F_{PFE} = \dot{m}_{ex}u_{ex} - \dot{m}_{in}u_{in} + p_{ex}A_{ex} - p_{in}A_{in} \tag{4.18}$$

$$C_T = \frac{2F_{PFE}}{\rho_{in}u_{in}^2 A_{in}} \tag{4.19}$$

The effectiveness of the electromagnetic field configuration in generating thrust can be measured by investigating the energy partitioning in the system, namely, by evaluating how much applied electromagnetic energy is being used to accelerate the plasma. The proportion of energy deposited into Joule heating versus acceleration can be quantified by the *Lorentz efficiency*. The Lorentz efficiency is defined as the ratio of the work done on the plasma by the Lorentz force to the total energy deposited into the system via the electromagnetic field, as seen in Eq. (4.20).

$$\eta_L = \frac{\int ujBdx}{\int jEdx} \tag{4.20}$$

The coefficient of thrust and the Lorentz efficiency at a given operating condition are computed using the above relations by varying the inlet conditions. Namely, velocity, temperature, and density are prescribed by assuming the freestream flow passes through a series of oblique shock waves upstream of the engine. Ionization, recombination, and the Hall effect are captured in the same manner as the simulations in the preceding section. For 40 km, 45 km, and 50 km altitudes, recombination does not significantly decrease the electron populations in the channel, so a single electron beam region is applied upstream of the inlet. The electron beam parameters are equivalent to the ones listed above. The applied electromagnetic fields can be tailored to match the operating conditions depending on the inlet Mach number, velocity, and corresponding Hall parameter.

For all solutions in this section, $B_y = 1$ T. At this magnetic field strength and pressure conditions at 40 km to 50 km altitude, the electron Hall parameter is expected to be on the order of $\beta_e = 10$. As such, electric fields are needed in both the transverse and axial directions to combat the Hall effect. As was noted in Chapter 3, strong axial fields are likely required at these altitude conditions, so caution must be exercised when selecting electric field configurations. For the following simulations, the transverse electric field is chosen to be $E_z = 1.5E_3$ (load factor $k = 1.5$), and the axial field is calculated assuming the Hall parameter is $\beta_e = 10$, i.e. $E_x = \beta_e(E_z - u_{in}B_y)$.

First, the Lorentz efficiency is computed for Mach 6-12 flight at 40-50 km altitude. The results are plotted in Fig 4.17. As the freestream Mach number increases, the thrust coefficient decreases for each altitude condition. Although thrust is achieved, increased flight speeds lead to higher dynamic pressures, which lowers the thrust coefficient. It should be noted that the relation for thrust in Eq. (4.18) contains terms for both the change in momentum of the flow and the change in pressure. For strong electric fields, the amount of Joule heating in the flow can be substantial, leading to significant static pressure increases, especially for high Mach numbers at the inlet. As was discussed extensively in Chapter 3 and the beginning of this chapter, high inlet Mach numbers only accelerate after an initial Joule heating phase for a constant area channel. The flow could be further accelerated to ambient pressures by using a nozzle downstream of the engine. When the electromagnetic field configuration is such that Joule heating overwhelms the amount of acceleration imparted on the flow, the PFE behaves closer to an electrothermal thruster than an electromagnetic thruster. However, high temperatures should be mainly avoided so that instabilities do not occur and the engine walls do not degrade.

As altitude increases, so does the coefficient of thrust. For the electromagnetic field configuration used to obtain these solutions, the coefficient of thrust at 40 km altitude decreases below unity by Mach 8. For these conditions, a stronger electromagnetic field configuration is needed to achieve thrust greater than the dynamic pressure acting on a surface the size of the engine's inlet. The dynamic pressure decreases at 45 km and 50 km, and the thrust generated relative to the dynamic pressure increases. For Mach 6 freestream flow at 50 km altitude conditions, the thrust is nearly four times greater than the dynamic pressure at the inlet. This characteristic is a promising feature of MHD accelerating low-pressure hypersonic plasmas. The prospect of achieving thrust at high altitudes is made possible since the technology does not depend on freestream flow compression. This analysis suggests that the promise is improved as freestream altitude increases since less thrust is needed to overcome drag.

Along with thrust, efficiency should also be considered when evaluating the performance

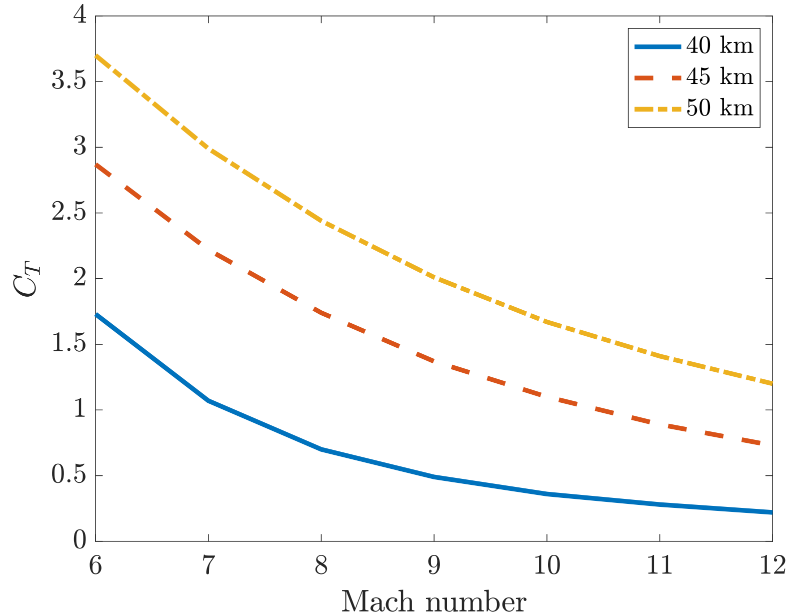

Figure 4.17: **Coefficient of thrust predictions over a range of freestream Mach numbers and altitudes.**

of MHD accelerators. The Lorentz efficiency in Eq. (4.20) only considers the amount of energy deposited into Joule heating and acceleration. It does not include energetic losses that may occur through the walls or in the components that generate the applied fields. Nor does it consider the energy spent on operating the electron beams in the engine. In this sense, the Lorentz efficiency can be seen as an *ideal* efficiency or a maximum that could be achieved without such inevitable processes. Nevertheless, it is still a helpful metric in understanding the effectiveness of electromagnetically accelerating a plasma at different conditions.

The Lorentz efficiency for the same conditions as above, Mach 6-12 flight at 40-50 km altitude, is computed and plotted in 4.18 using the same geometry and electric and magnetic field strengths. Similar to the coefficient of thrust, the Lorentz efficiency also decreases as the freestream Mach number increases. This is an expected result as the acceleration of high Mach number flows becomes increasingly difficult without significant Joule heating for a constant area channel. Thus, more energy is being deposited into heating instead of acceleration.

As the altitude increases, so does the Lorentz efficiency. At the low pressures that occur at

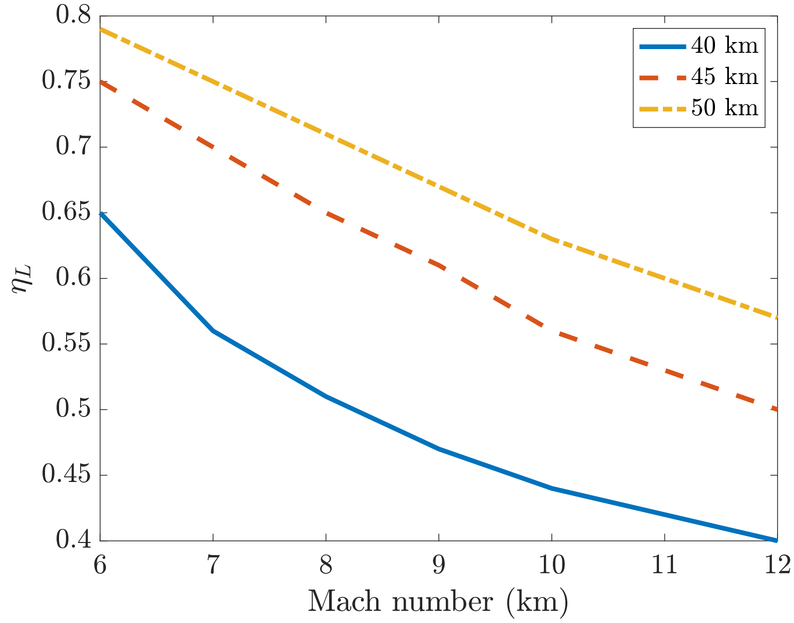

Figure 4.18: **Lorentz efficiency predictions over a range of freestream Mach numbers and altitudes.**

50 km altitude, the magnetic interaction parameter is higher than the lower altitude conditions, meaning the electromagnetic forces can more easily overcome the inertial forces of the bulk plasma. Furthermore, electron number densities do not decay due to recombination as fast for the higher altitude conditions, which leads to more efficient acceleration downstream in the channel. Regardless, the Lorentz efficiencies are greater than 50% for most of the flight conditions simulated here. The conditions where it is not greater than 50% mostly correspond to high Mach number flight at low altitude conditions. Thus, it is reasonable to conclude that using electromagnetic acceleration for hypersonic flows at conditions below 40 km is not as promising as flying at altitudes above 40 km. The recombination studies in the preceding section and the magnetic interaction parameters in the previous chapter support this evidence. It is also noted that the high electron Hall parameters for the 50 km conditions may necessitate an axial field larger than required for the lower altitudes. Thus, although efficiency might be improved, the total power needed to generate the electric field might be more significant. More efficient configurations can be achieved by decreasing the load factor or by varying the cross-sectional area of the channel and electric field strength as was done

earlier in this chapter.

4.6 Conclusion

This chapter used the one-dimensional model to illustrate the behavior of several baseline MHD accelerated flows. A constant conductivity was initially assumed to arrive at solutions to the governing equations for both subsonic and supersonic flows. It was found that the numerical solutions follow the behavior of the solutions produced by the one-dimensional MHD channel theory. Namely, if the electrical conductivity is high enough for an initially subsonic plasma, it will flow through Mach 1 with continuous acceleration. On the other hand, an initially supersonic plasma will undergo significant Joule heating such that the flow will drop below the sonic line near the inlet if the electric field is strong enough. Then, the shock-like structure will pass through the inlet, where momentum and total temperature are prescribed, allowing the inlet to become subsonic. Once this occurs, the flow will behave like the initially subsonic cases from before.

Characteristic electric field strengths that bound different operating regimes of MHD accelerators were defined. It is noted that acceleration still occurs for a Lorentz-mode accelerator as long as the electric field is less than $E_3 = u/B$. However, stronger electric fields do not guarantee more efficient acceleration. These insights were used to motivate the operating regime in which hypersonic MHD accelerators should exist. Several numerical solutions were given for electric fields in this regime.

Furthermore, it was demonstrated how performance can be improved by modifying the channel geometry and electric field configuration. Acceleration in these channels is balanced by the Lorentz force and resulting adverse pressure gradients caused by Joule heating. Large pressure gradients can be combatted by employing expanding channels. Then, to further improve efficiency and decrease overall Joule heating, the electric field can be ramped to keep the electric field close to the characteristic electric field E_3.

Appropriate plasma chemistry models are needed to arrive at predictive simulations of hypersonic MHD accelerators. Two essential transport properties, the Hall parameter and electric conductivity, are functions of plasma mobility. A model for electron mobility as a function of reduced electric field derived from solutions to the electron Boltzmann equation was provided. Then, plasma ionization and recombination rates were presented to evaluate the consequences of variable electron number density populations in MHD energy conversion devices.

Then, the plasma chemistry models were used to calculate an order of magnitude estimate of the electron populations for various operating conditions. It was found that for 30 km and below, a single electron beam at the inlet would not be sufficient for maintaining conductivity in the channel. Instead, multiple electron beams would likely be needed to ensure adequate MHD interaction for those lower altitudes. In the 40 km and 50 km conditions, recombination is slower due to the reduced collisionality of the plasma.

The one-dimensional model was used to evaluate the performance of a Mach 5 MHD accelerator at 40 km. These simulations included ionization, recombination, and the Hall effect. Degree of ionization, electrical conductivity, and electron Hall parameter profiles were given as a function of axial distance in the channel. Since this system's electron Hall parameter is greater than unity, an axial electric field is needed for Lorentz-mode operation. As such, the axial electric field was varied between 1000 V/m and 4000 V/m to highlight that the balance between acceleration and Joule heating still exists outside of the Faraday configuration context that the solutions at the beginning of this chapter assumed for lower electron Hall parameters. Overall, larger electric fields are needed to utilize the Hall currents for acceleration.

Finally, one-dimensional simulations were performed to evaluate the performance of a PFE configuration at a range of freestream Mach numbers and altitude conditions. Two performance metrics, Lorentz efficiency and coefficient of thrust, were introduced to conduct this analysis. The Lorentz efficiency quantifies the amount of energy converted to acceleration as opposed to heating. It was found that as Mach number increases, the Lorentz efficiency decreases. However, as the altitude is increased, the Lorentz efficiency also increases. Similarly, coefficient of thrust decreases with higher freestream Mach number and densities, but increases with altitude. These results suggest that PFE operation is feasible at high hypersonic Mach numbers and altitudes above 40 km.

Before the optimal electromagnetic field configuration and channel geometry for a given operating condition are determined, several questions about the consequences of the Hall effect in multiple dimensions need to be answered. For example, the simulations in this chapter neglected non-axial acceleration due to the Lorentz force. Furthermore, nonuniform flow and electric field properties across the channel were not considered. Multi-dimensional simulations are required to understand the consequence of these physical effects, which must be performed before optimization studies. However, once these multi-dimensional effects are appropriately quantified, the one-dimensional model is ideal for determining optimal configurations for a wide range of operating conditions.

Chapter 5

Multi-Dimensional Modeling

In Chapter 4, one-dimensional solutions to the governing equations were presented for a range of operating conditions that elicited the fundamental behavior of MHD accelerated hypersonic channel flows. Relationships between acceleration, heating, channel geometry, and electric field strength were described in detail from these numerical simulations. Although the one-dimensional solutions are beneficial for reduced-order calculations and building design intuition, they are limited in providing detailed information about the flow structure in physical applications.

In this chapter, higher-dimensional analyses will be performed to uncover aspects of hypersonic MHD channel flow that are inaccessible by one-dimensional models. In viscous channels, acceleration will be balanced by the Lorentz force, pressure gradients, and viscous deceleration due to the no-slip condition at the walls. Furthermore, flow properties will be nonuniform in the spanwise direction, resulting in complicated multi-dimensional flow structures. Previous 3D simulations of MHD bypass scramjets and arc discharge actuators for flow control showed that three-dimensional effects significantly impact the overall flow behavior [52, 64]. On one hand, the Hall effect and ion slip lead to an axial component of current density, especially near the edges of electrodes, which alters the direction of the Lorentz force. On the other hand, complex corner flow structures form due to the intersection of shocks and viscous boundary layers.

The first portion of this chapter will be devoted to developing a test case demonstrating LeMANS-MHD. Namely, simulations of a high-speed flow through a channel with MHD boundary conditions will be performed under several assumptions. This test is useful for benchmarking

LeMANS to the theoretical predictions and other numerical tools such as the one-dimensional models. Then, three-dimensional simulations of a practical MHD accelerator geometry will be performed to highlight the complex multi-dimensional nature of these flows. Comparisons to the one-dimensional theory will be made, and the impact of viscous deceleration will be discussed. Finally, two-dimensional simulations will be performed that include the Hall effect and the challenges of running these simulations will be discussed. These challenges are linked to physical effects that are important to understand for low-pressure hypersonic MHD accelerator technology to advance.

5.1 Two-Dimensional Test Case

The multi-dimensional hypersonic nonequilibrium CFD code, LeMANS-MHD, described in Chapter 2 is used to find solutions to the low magnetic Reynolds number MHD equations for various operating conditions of interest. LeMANS-MHD couples the flow dynamic equations to the applied electromagnetic fields via a finite volume generalized Ohm's law solver. Several options are available in LeMANS-MHD for prescribing magnetic fields in the domain. However, a constant magnetic field will be applied throughout the entire domain in this chapter, automatically satisfying the $\vec{\nabla} \cdot \vec{B} = 0$ constraint. The electric fields are applied by assigning the appropriate MHD conditions at each boundary face of the computational mesh. Table 5.1 categorizes these conditions based on the type of boundary in which they are applied.

Table 5.1: MHD boundary conditions in LeMANS-MHD (also Table 4.1 in [1]).

Boundary Type	Boundary Condition
Conducting wall	$\phi =$specified
Insulating wall	$\vec{j} \cdot \vec{n} = 0$
Other	$\vec{E} \cdot \vec{n} = 0$

For conducting walls (i.e., electrodes), the electric potential, ϕ, is prescribed as an input before simulations begin. In MHD channel simulations, this value is usually chosen by multiplying the desired electric field strength by the width of the channel. For example, if the target electric field strength is 1000 V/m, and the channel is 10 cm wide, then the appropriate boundary condition is prescribing a potential difference of $\phi = 100$ between the electrodes across the channel. In the legacy version of LeMANS-MHD, this boundary condition was assigned by prescribing the electric field and a bounding box in which the electrodes reside. Therefore, seven values per electrode were needed to assign an electric potential in the domain: the electric potential and six spatial coordinates. Since this task becomes increasingly cumbersome and error-prone as more electrodes are included, a new workflow was implemented to streamline simulations. The old approach used a logic-based approach to determine whether the cell centers lived in the electrode-bounding boxes. In the new approach, the electrodes are defined as separate domains in the mesh generation phase by first defining them as "Walls" and then naming them "electrodes." While LeMANS is processing the mesh, it checks the name of each "Wall" face it reads. If a"Wall" face is named "electrodes" it is classified as a standard wall for all of the fluid dynamic boundary condition routines and as an electrode for the MHD routines.

A two-dimensional test case is presented to demonstrate the general characteristics of MHD simulations using LeMANS. This test case is based on a 10 cm by 50 cm channel with electrodes spanning the entirety of the top and bottom walls. The inlet boundary conditions are prescribed based on Mach 5 flow at 20 km altitude. In anticipation of future wind tunnel tests of MHD accelerated hypersonic channel flows, the working gas in this case is nitrogen. As such, the inlet velocity and temperature are 1500 m/s and 216.65 K, respectively. A constant degree of ionization of $\alpha = 1 \times 10^{-3}$ and scalar conductivity is initially assumed such that flow acceleration occurs strictly in the flow's direction.

According to the one-dimensional MHD channel theory in Chapter 3, the range of electric fields that yield acceleration is between $E_3 = 1500$ V/m and $E_1 = 5250$ V/m. As an illustrative example to explore the relationship between acceleration and Joule heating in the multi-dimensional setting, the electrode boundary conditions are specified such that an electric field of $E = 3000$ V/m is obtained in the channel. When prescribing electric potential boundary conditions, the voltage *difference* between electrodes is what generates the electric field, so a voltage drop of 300 V is needed. For this case, the electric voltage potential is specified to be $\phi = 0$ V on the top wall

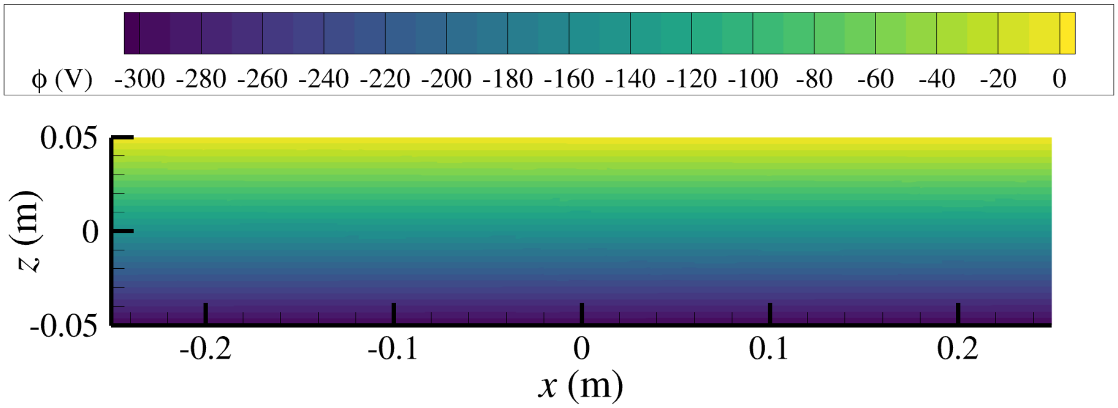

Figure 5.1: **Electric potential contours for two-dimensional test case**.

(anode) and $\phi = -300$ V at the bottom wall (cathode). Figure 5.1 shows the two-dimensional electric potential contours.

In this case, with continuous electrodes, the electric potential field is linear in the z-direction, which is expected with the applied MHD boundary conditions and under the assumption of scalar conductivity. The resulting electric field is solely in the z-direction and does not change with axial distance. Additionally, at the inlet and outlet boundaries, an $\vec{E} \cdot \vec{n} = 0$ condition is applied. This condition is typically applied for boundaries that are sufficiently far from the applied fields, however it is adequate for this geometry since the electric field is expected to only vary in the tangential direction relative to the inlet and outlet boundaries. With these boundary conditions and assumptions, the plasma is smoothly accelerated down the length of the channel. Velocity contours are shown in Fig. 5.2.

The core flow is accelerated from 1500 m/s to approximately 2800 m/s. However, boundary layers are still necessary to ensure the no-slip condition is met at the walls. This case is similar to the canonical Hartmann flow in which pressure-driven flow between two parallel plates is accelerated via the Lorentz force. As the magnetic field strength increases in Hartmann flow, the velocity gradients steepen near the wall and flatten towards the centerline. A similar structure can be observed in

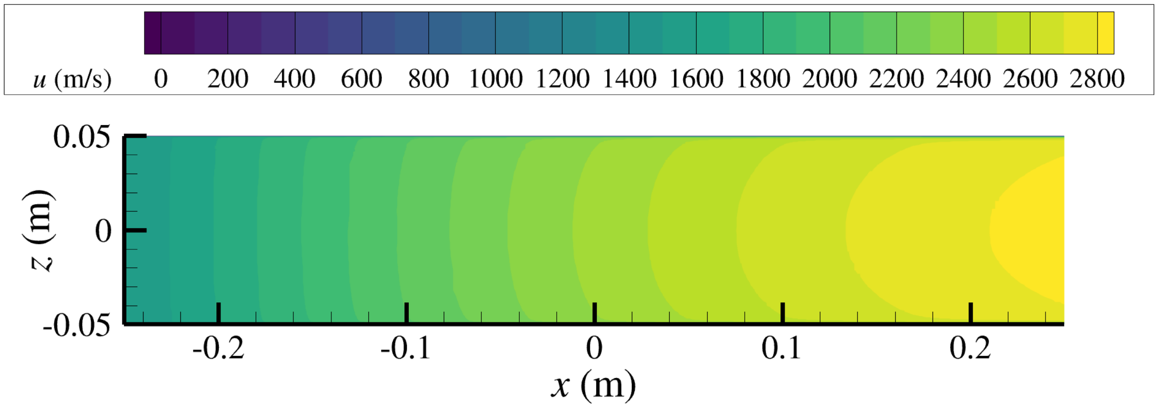

Figure 5.2: **Velocity contours for two-dimensional test case.**

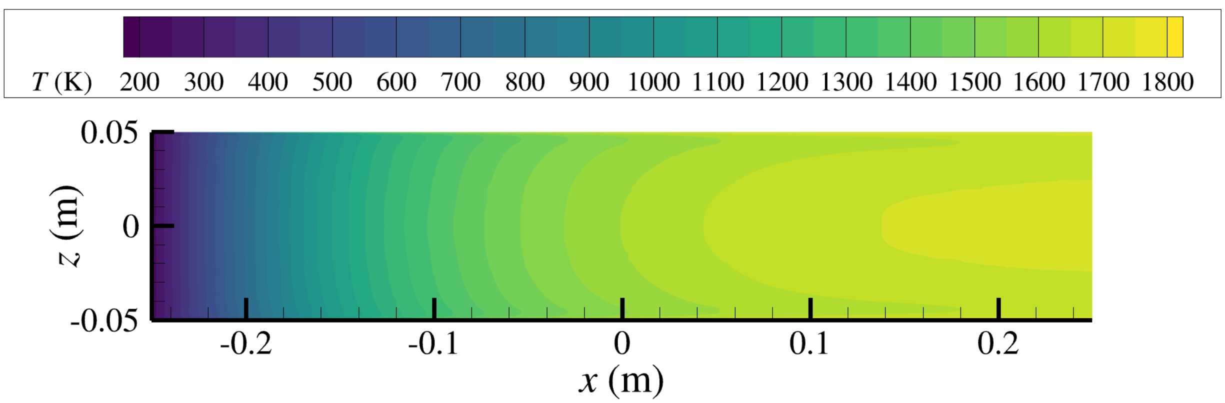

Figure 5.3: **Temperature contours for two-dimensional test case.**

this test case. In addition to acceleration, the applied electric fields heat the core flow, but thermal boundary layers form to meet the isothermal wall boundary condition. Although several wall boundary conditions are available in LeMANS, isothermal boundary conditions mimic wind tunnel conditions where flow residence times are too short to heat the walls above room temperature significantly. Figure 5.3 shows two-dimensional temperature contours for the test case.

The core flow is heated from 216 K at the inlet to nearly 1800 K at the outlet, with the sharpest temperature gradient due to Joule heating near the inlet. Downstream in the channel, the centerline temperature reaches a near-constant value. It is also noted that near the wall, a small region of high temperatures that appear as spikes in the contour plots exists. These spikes are due to the very high shear stresses in wall-bounded hypersonic flows. In addition to viscous heating, Joule heating consumes a more significant portion of the total energy deposited in the boundary layer than it does in the core flow. The effective electric field, $\vec{E}' = \vec{E} + \vec{u} \times \vec{B}$ is stronger in the boundary layers than in the high-speed core flow regions, so the current densities are also higher near the walls. As the velocity goes to zero at the wall, the ratio of Joule heating to total energy deposited, $\frac{\vec{\vec{\sigma}}^{-1} \cdot \vec{j} \cdot \vec{j}}{\vec{j} \cdot \vec{E}}$, goes to unity. As the core flow is accelerated to higher velocities, viscous heating may cause high temperatures such that thermal ionization occurs. These hot boundary layers will lead to a local increase in electron populations thereby increasing electrical conductivity, resulting in greater magnetic interaction than in cooler regions, leading to what has been called *velocity overshoot* in the boundary layer [25]. Similarly, any transient local increase in temperature may lead to an increase in conductivity through ionization, which leads to increased Joule heating in that area. This repeating cycle, the so-called *Joule heating instability*, is made worse by a transverse magnetic field since strong magnetic fields will severely limit the drift of electrons in directions perpendicular to the field lines. Nevertheless, it is noted that peak temperatures occur in the boundary layers that may exceed the temperatures near the center of the channel.

Finally, it is yet to be seen if the one-dimensional theory described in Chapters 3 and 4 remains applicable to multi-dimensional MHD accelerator simulations. The velocity versus Mach number space is used again to examine the behavior of MHD accelerated channel flows, but now for a multi-dimensional viscous channel. Figure 5.4 plots the velocity versus Mach number data from the centerline profile at $z = 0.0$ m along with the analytical solution as defined by the procedure outlined for Eq. 2.78. For these inlet conditions, $u_1 = 857$ m/s, $u_3 = 3000$ m/s, and $c = -0.5101$.

The centerline velocity versus Mach number profile solution matches the behavior of the one-dimensional numerical solutions from the previous chapter. Namely, there is an initial decrease in Mach number due to Joule heating seen in the temperature contours in Fig. 5.3, followed by a region of acceleration with slightly increasing Mach number. Overall, there is good agreement between

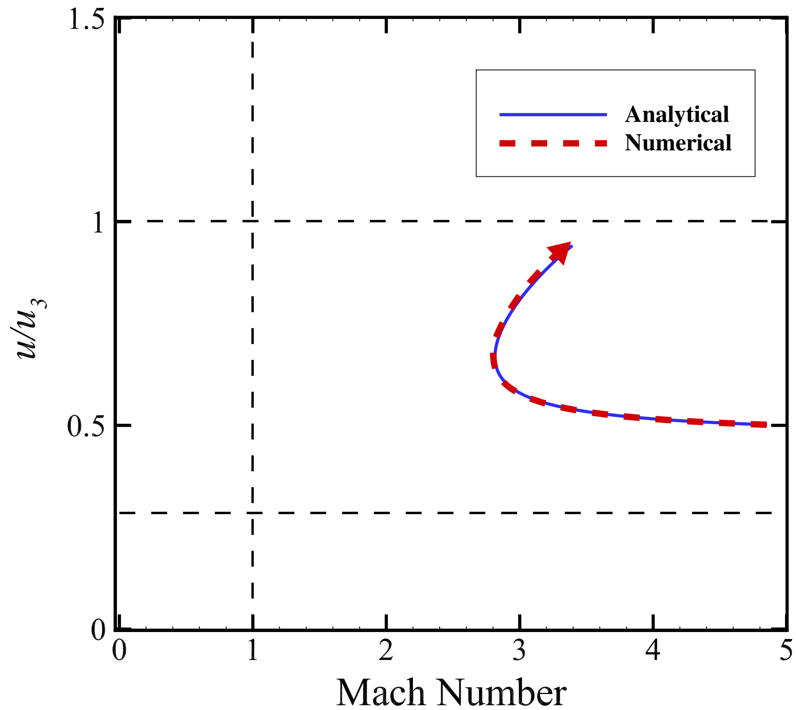

Figure 5.4: **Velocity versus Mach number profile for two-dimensional test case.**

the analytical solution using Eq. 2.78 and the numerical solutions using LeMANS-MHD. Although the flow velocity nearly doubles from the inlet to the outlet, the Mach number decreases from 5 to just above 3 in the same span. These results further motivate the use of the one-dimensional theory to design MHD accelerators and illustrate that solutions obtained with LeMANS replicate the theory under the correct assumptions.

5.2 Three-Dimensional Baseline Simulations

In this section, a three-dimensional MHD accelerator geometry is presented, and a numerical simulation is performed using LeMANS-MHD. This geometry is based on a prior MHD accelerator facility developed at NASA Ames Research Center but with a few differences due to the higher velocity and lower pressure conditions in this application [6]. The electric potential fields are computed using constant ionization and scalar electrical conductivity. Then, electric field and current density profiles in various regions throughout the channel are described. Similar to the one-dimensional discussion in Chapter 5, the balance between Lorentz force acceleration and Joule heating is investigated with the addition of three-dimensional viscous effects and electrode segmentation.

5.2.1 Computational Setup

The MHD accelerated NASA EAST facility is one of the more recent examples of success in accelerating high-speed flows using electromagnetic fields. The channel width and height at the inlet are 2 cm and 1 cm, respectively. The width and height of the outlet are both 2 cm. This configuration consists of 13 electrode pairs, each 1 cm long and spanning the entire width of the channel with 0.5 cm spacing between the edges of the electrodes. These regions in between the electrode pairs are called the insulating wall regions. Figure 5.5 gives the side and top views of this particular configuration. The magnetic field strength is a constant 1 T in the positive y-direction throughout the entire domain. The electric potential is specified on each electrode boundary, and the electric field is solved for using Eq. (2.47). In this work, the electric field is generated mainly in the z-direction by a voltage difference set at opposing electrodes across the channel.

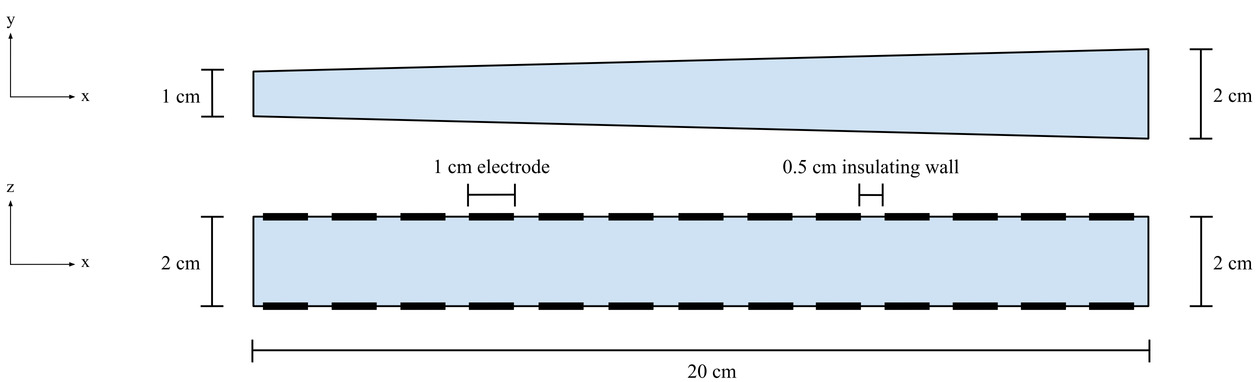

Figure 5.5: **MHD accelerator computational domain based on facility in Ref. [6].**

It is assumed that upstream of the inlet to the MHD accelerator, the freestream gas is slowed via a series of oblique shock waves in an engine inlet. More precisely, the flow is assumed to be diverted by two oblique shocks formed by a 7° wedge. The inlet conditions to the computational domain are then prescribed based on this post-shock state. Since the freestream conditions are hypersonic, the flow is expected to be supersonic at both the inlet and outlet of the channel, so a zero-gradient boundary condition is applied at both domains. The pre-shock velocity, temperature, and pressure correspond to Mach 10 flight at 60 km altitude, which was previously considered a target operating condition since the magnetic interaction parameter is high at low densities. Subsequently, the inlet Mach number is approximately Mach 5, the inlet temperature is 919 K, and the inlet density of argon is 1.836×10^{-3} kg/m^3. The walls are considered isothermal at 1000 K. Additionally, the flow is assumed to be in thermal equilibrium, and each of the internal degrees of freedom is characterized by a single temperature, $T = T_{tr}$. This analysis neglects the electron beam region upstream of the engine. Instead, the degree of ionization is assumed constant throughout the entire domain and is initialized at the inlet to be $\alpha = n_e/N = 1 \times 10^{-4}$.

Point implicit time integration is used until the solution reaches steady-state convergence. Additionally, the Ohm's law solver is coupled to the flow solver to update the electric potential with the flow velocity, $\vec{u}$, and flow scalar conductivity, σ. The computational mesh contains 250 cells in the x-direction and 60 cells each in the other two directions. The simulations are run in parallel across 200 CPUs until convergence.

In this three-dimensional simulation, three-species argon is the working plasma (i.e., Ar, Ar^+, e^-). There are several conductivity models readily available in LeMANS for argon and air. It was highlighted in Ref. [68] that commonly used semi-empirical models for electrical conductivity are inadequate for simulating wide ranges of MHD-augmented hypersonic flows. The model used in this work is based on polynomial curve fits to solutions of the electron Boltzmann equation, similar to the model in Chapter 4. The form of the second-order polynomial is given in Eq. (5.1)

$$\sigma = c_0 + \sum_{i=1}^{ND}(c_i d_i) + \sum_{i=1}^{ND}\sum_{j=1}^{ND}(c_{i,j} d_i d_j) \tag{5.1}$$

where σ is the scalar conductivity and c are the polynomial coefficients. The dimensions of the model, d, are the species molar concentrations, χ_{Ar} and χ_{Ar^+}, as well as the reduced electric field,

E/N, for three-species argon. The molar concentration of electrons is not needed in the model since charge neutrality is assumed throughout the computational domain. ND is the total number of dimensions. Although the model is used for three-species argon in this work, the corresponding electrical conductivity can be found for other systems, such as air, using appropriate coefficients. Additional details about the conductivity model and the electric potential solver can be found in Ref. [1]. The coefficients are read in via input files depending on the working gas and degree of the polynomial fit. It is noted that as ND increases, the number of coefficients also increases. For example, a second-order model for eleven-species air would require 66 coefficients, and third-order model would require 286 coefficients. While higher order models are computationally intensive, they are required to capture the extrema associated with peaks in each of the ionic species. However, the argon model used in this section is sufficient and has been previously shown to work well in MHD reentry flows [68].

5.2.2 Electromagnetic Field

First, to illustrate the structure of the electric fields within this MHD accelerator geometry, steady-state electric potential solutions are shown in Fig. 5.6 for a single electrode pair at the half-length of the PFE. Additionally, vectors are shown indicating the direction of the current density in the x-z plane, but not the magnitude. The electrodes at the top and the bottom of the domain span from $x = 0.095$ m to $x = 0.105$ m.

In this case, an electric potential difference of 140 V is applied across the electrodes, corresponding to a nominal electric field of 7000 V/m in the bulk flow of the channel. This electric field selection combined with a 1 T magnetic field corresponds to an inlet velocity near the characteristic velocity, u_1. Significant acceleration is expected at the cost of a large amount of Joule heating for a sufficiently high degree of ionization. As can be seen for scalar conductivity, the current density is mainly in the negative z-direction. Thus, with a magnetic field in the y-direction, the Lorentz force accelerates the flow in the positive x-direction. The resulting electric field in the z-direction throughout the entire domain is plotted in Fig. 5.7. The electric field in the z-direction is weakest

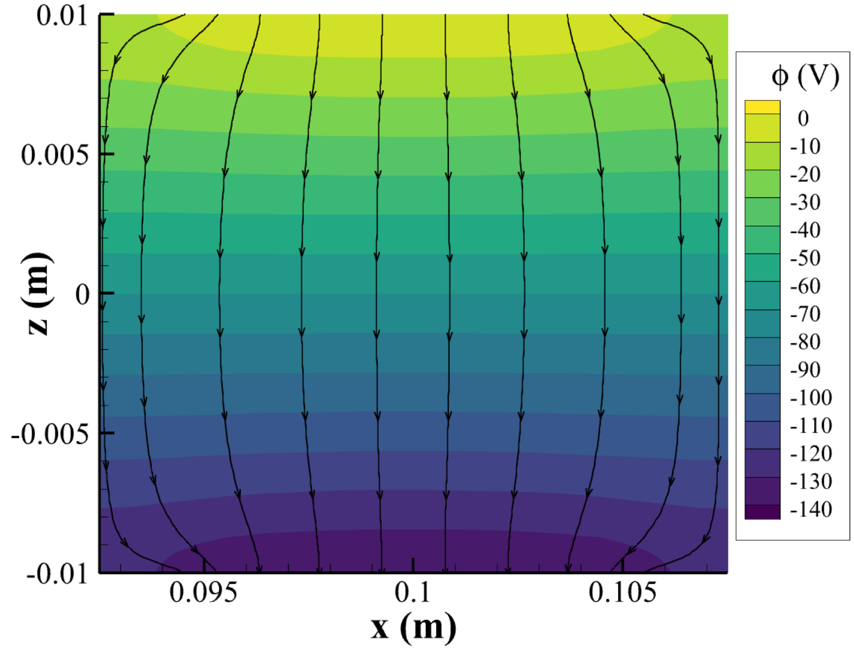

Figure 5.6: **Electric potential solution at a single electrode pair.**

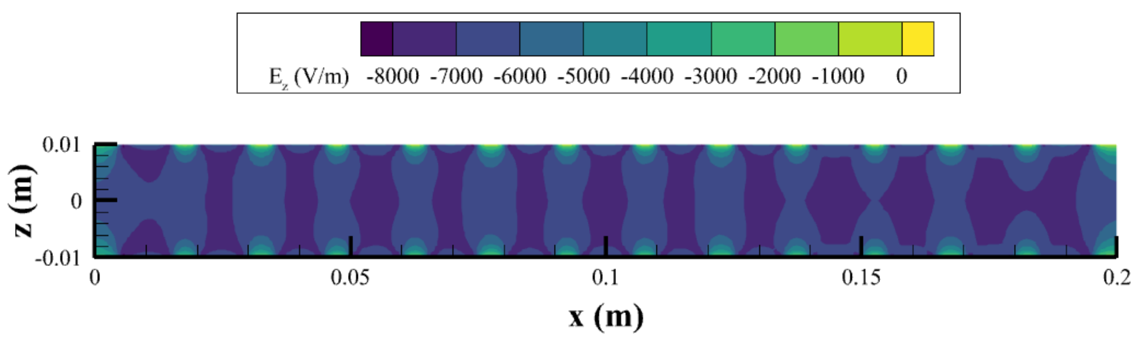

Figure 5.7: **Electric field in z-direction evaluated in the y = 0 plane.**

near the electrode/insulating wall interfaces. At the edges of the electrodes, an axial component in current density forms but is quickly diminished towards the center of the channel.

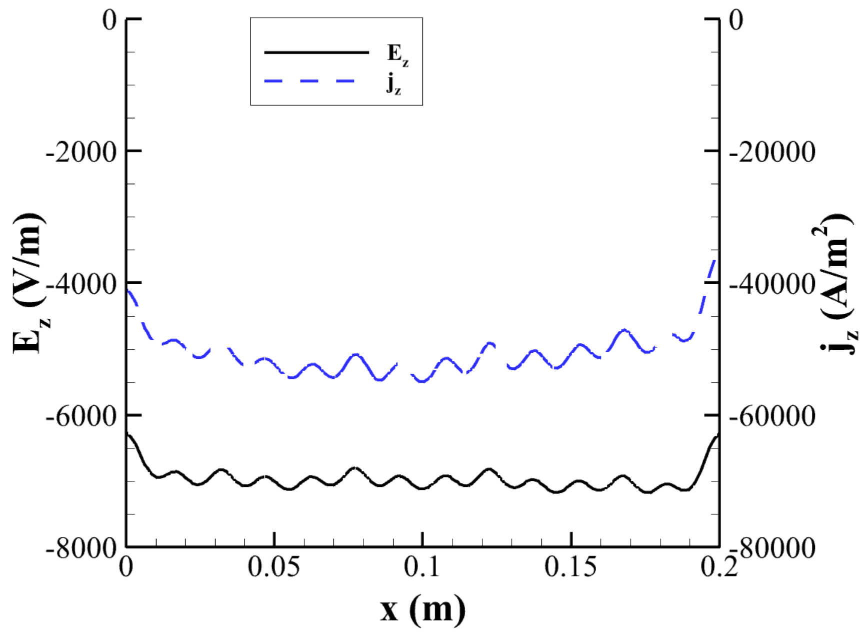

Figure 5.8: **Electric field and current density versus axial position along the centerline of the channel.**

The electric field strength and resulting current density are strongest in electrode regions and decrease in the insulating wall regions. As the electric field induced by the plasma moving through a constant magnetic field increases, the net electric field in the reference frame moving with the plasma decreases. The electric field in the bulk flow is shown via the centerline profiles plotted in Fig. 5.8. The current density along the centerline is also shown. As can be seen, there is noticeable variation in the electric field and the current density along the centerline. This variation can be attributed to the weakened electric field in the insulating wall regions and the weakened conductivity since the conductivity is also a function of the electric field.

Comparisons of the electric fields and current densities at an electrode station and an insulating wall station are made in Fig. 5.9. More specifically, profiles are plotted along the z-direction at the center of the channel ($y = 0$ m) for an electrode located at $x = 0.1$ m and an insulating wall located at $x = 0.1075$ m. A decrease in current density between electrodes in this segmented

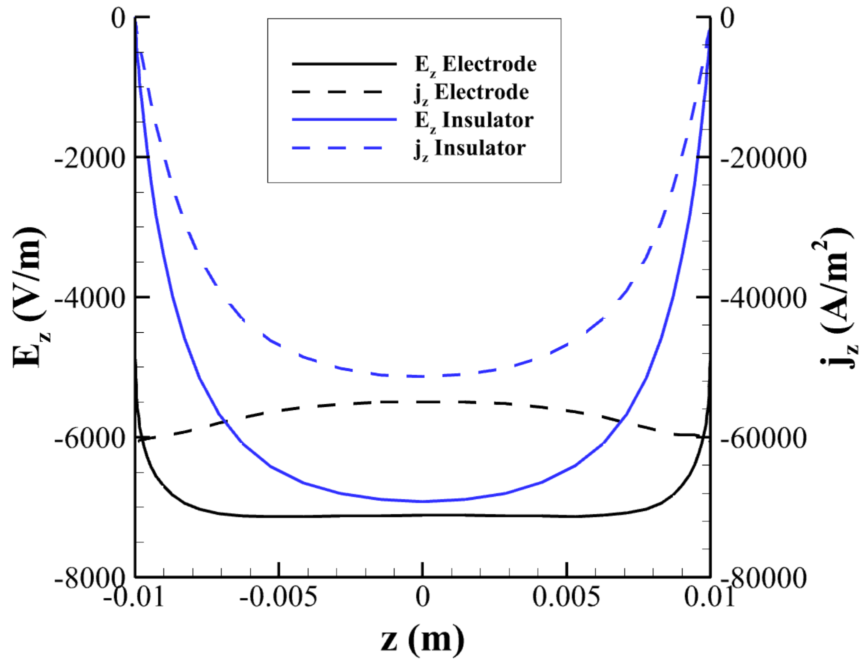

Figure 5.9: **Electric field and current density across the width of a channel at an electrode location (x = 0.1 m) and an insulating wall location (x = 0.1075 m). Both profiles are taken from y = 0 m.**

configuration leads to less acceleration via the Lorentz force. Furthermore, the electric field and, thus, the maximum velocity achievable is also decreased in these regions, especially near the walls. Namely, the insulating wall boundary conditions require no current density in the direction normal to the wall, so the presence of walls will limit the total acceleration.

5.2.3 Flow Field

Now that the electromagnetic field in the MHD accelerator channel has been established, it is possible to examine its effect on the flow field. Figure 5.10 illustrates the three-dimensional behavior of the velocity field within the PFE. The contours in the top and bottom of Fig. 5.10 are taken from the $z = 0$ m and $y = 0$ m mid-planes, respectively. Although the boundary layer grows downstream, it is apparent that the electromagnetic body force limits the final boundary layer thickness such that the majority of the bulk flow is able to accelerate. Additionally, the bulk flow is heated significantly, as shown in the temperature contours plotted in Fig. 5.11.

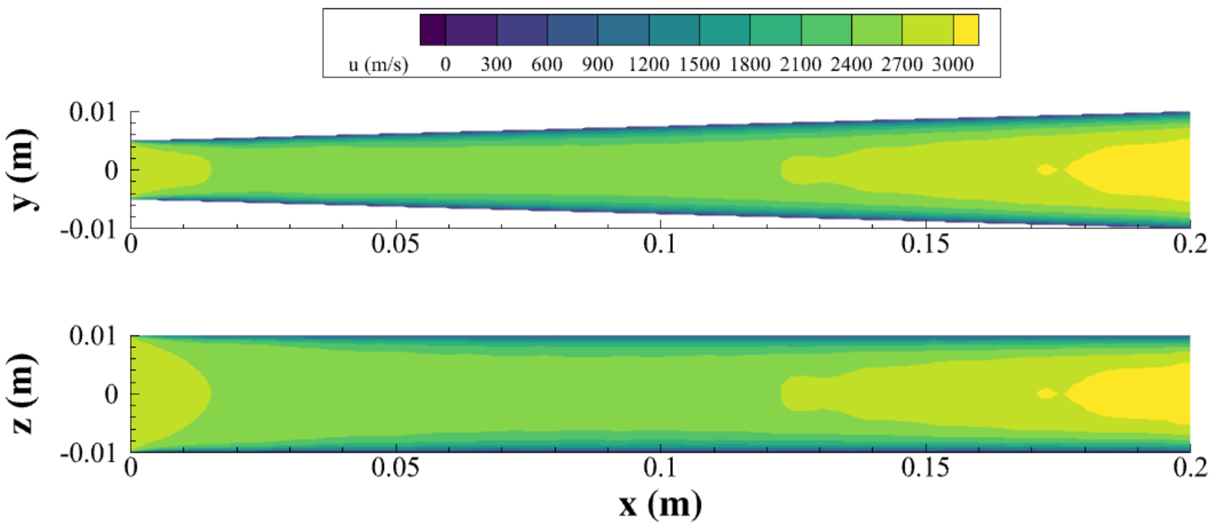

Figure 5.10: **Two-dimensional x-velocity contours evaluated in the z = 0 m plane and the y = 0 m plane.**

The applied electromagnetic fields in the previous section lead to a Lorentz force that provides acceleration to the working gas, which can most easily be seen by observing the velocity profile along the channel's centerline, shown in Fig. 5.12. For a nominal electric field strength of $E_z = 7000$ V/m, the flow experiences a net acceleration from inlet to outlet. An initial deceleration is seen because the applied electric field is not strong enough to overcome the pressure gradient generated by Joule heating. As the velocity increases downstream in the channel, the Mach number also slightly increases near the outlet, as shown in Fig. 5.12.

The decrease in Mach number down the channel is due to increased temperature caused by Joule heating. Centerline temperature and pressure profiles are shown in Fig. 5.13. Extremely high temperatures are seen which would result in thermal ionization throughout the channel and likely breakdown between electrodes. These temperatures qualitatively illustrate the amount of heating

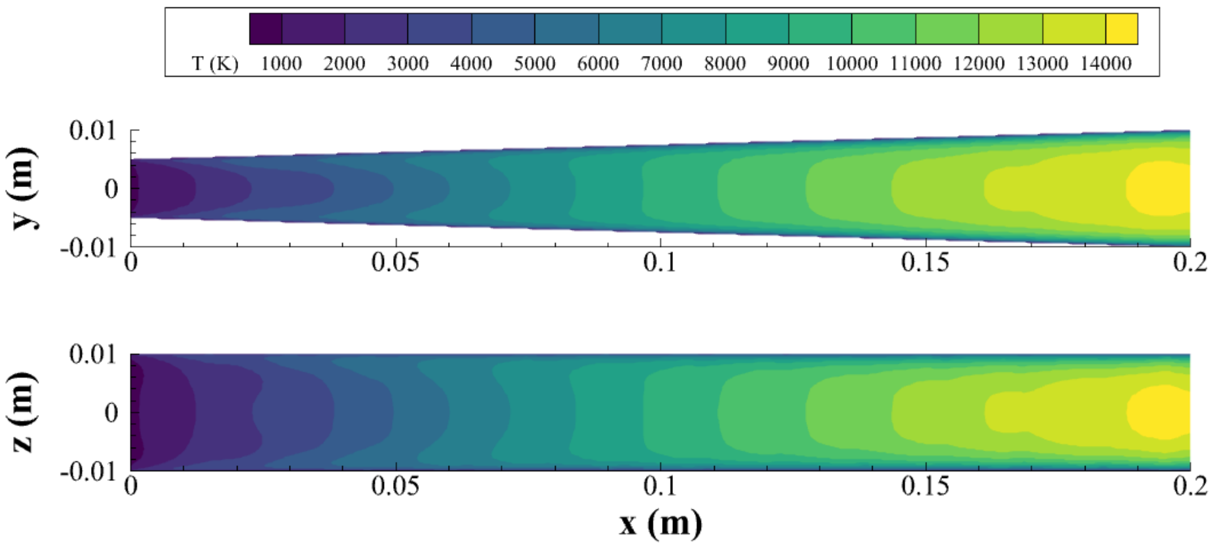

Figure 5.11: **Two-dimensional temperature contours evaluated in the z = 0 m plane and the y = 0 m plane.**

that occurs for these operating conditions which highlights the importance of carefully designing the electromagnetic fields and geometry of MHD accelerated hypersonic channels to avoid inefficient energy deposition. Most of the heating occurs near the beginning of the channel and occurs more rapidly than the acceleration. This corresponds to a preliminary Joule heating phase that occurs before significant acceleration can be achieved for a fixed velocity, Mach number, and electric field strength. A diverging channel is necessary to counteract the viscous and pressure forces acting against the flow for the inlet conditions and electromagnetic fields presented here.

5.2.4 Velocity Versus Mach Number

The three-dimensional solutions presented above can be visualized using a velocity versus Mach number diagram just as the one-dimensional solutions in Chapter 4 and the test case in this Chapter. Observations from this diagram allow for a closer inspection of the balance between Joule heating and Lorentz force acceleration. Figure 5.14 plots the centerline solutions from the three-dimensional analysis onto the velocity-Mach number plane. The vertical axis is normalized by the nominal centerline characteristic velocity $u_3 = 7000$ m/s.

Although a net acceleration is seen for this case, the final velocity remains much lower than the theoretical maximum, $u = u_3$. Furthermore, the decrease in Mach number due to Joule heating outweighs the total Lorentz force acceleration. Viscous deceleration also counteracts the Lorentz force which causes non-smooth acceleration. The relative importance of these two mechanisms can be quantified using the Lorentz efficiency, which is the ratio of work done on the plasma by the Lorentz force to the total energy deposited. For a three-dimensional volume, the Lorentz efficiency is calculated with Eq. (5.2).

$$\eta_L = \frac{\iiint \vec{u} \cdot \left(\vec{j} \times \vec{B}\right) dV}{\iiint \vec{j} \cdot \vec{E} dV} \tag{5.2}$$

In this case, the Lorentz efficiency is calculated to be 40%. Higher Lorentz efficiencies can be

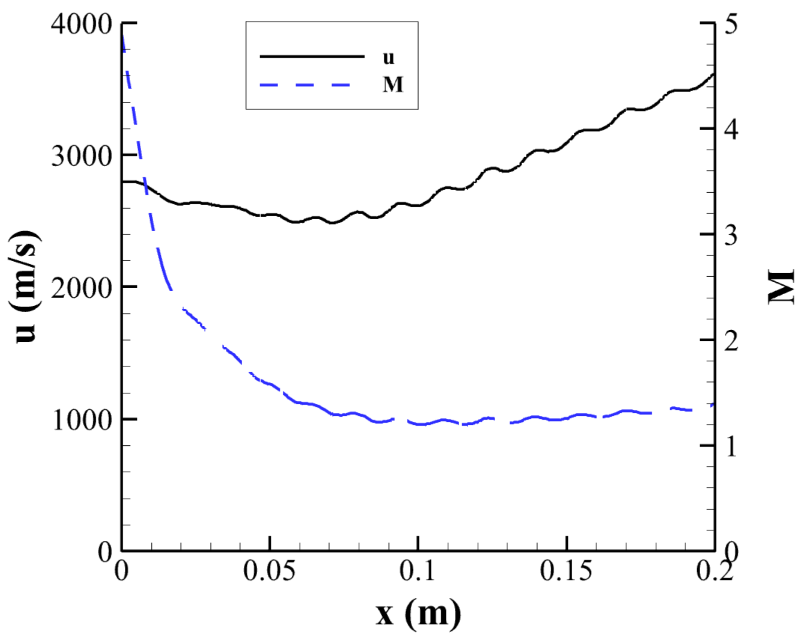

Figure 5.12: **Centerline velocity and Mach number profiles.**

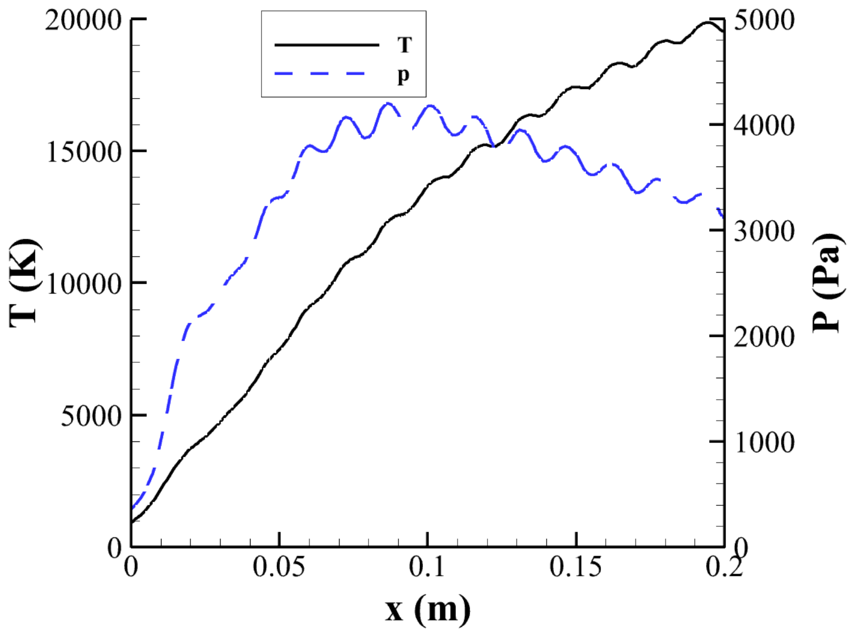

Figure 5.13: **Centerline temperature and pressure profiles.**

achieved by decreasing the electric field such that u/u_3 approaches unity at the inlet. In this case, where a 140 V voltage drop is applied across a 2 cm gap, there is a significant amount of Joule heating in addition to the acceleration, suggesting that more efficient acceleration could be achieved by decreasing the electric field strength. Naturally, this would decrease the net thrust gained by the engine. Longer channels, specially tuned variable electromagnetic fields, or more expansion would be necessary to improve the performance given these flight conditions. However, consideration must be given to keeping the reduced electric fields low in the channel to avoid unstable ionization. Parametric studies, such as the ones presented in the previous Chapter, can be used to further iterate the design variables. Regardless, the general behavior of the curve in Fig. 3.1 agrees with the predictions made by the one-dimensional MHD accelerator theory. For the inlet velocity and Mach number combination shown here, the flow initially experiences a decrease in Mach number followed by a sharp increase in velocity with increasing Mach number.

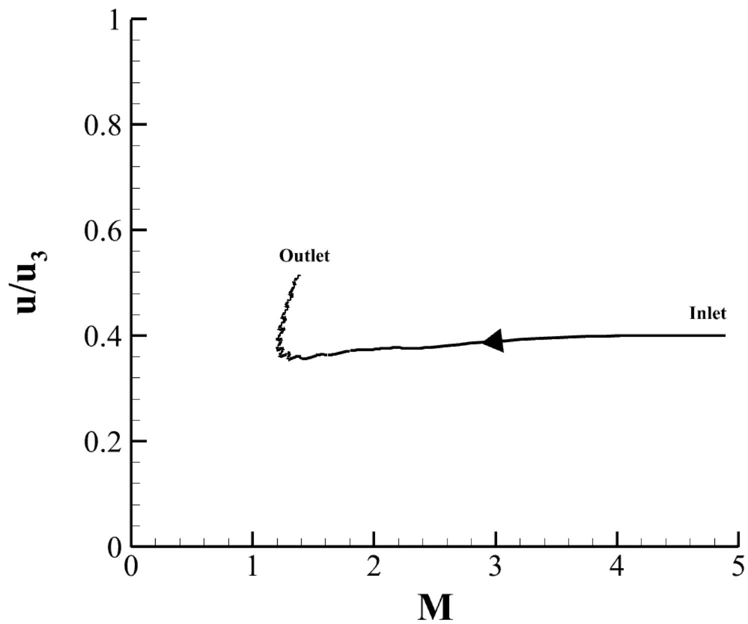

Figure 5.14: **Velocity versus Mach number diagram for three-dimensional solutions.**

5.3 Design Guidance for Electrode Segmentation

The electron Hall parameter is expected to be near unity or above for altitude conditions of 20 km and above. It has been claimed that finite segmentation of the electrodes will aid in mitigating the Hall currents for Faraday configuration channels at these conditions. Namely, the goal is to form a closed path for the current to travel between electrodes by utilizing relatively thin electrodes in the axial direction separated by insulating wall regions. By doing so, the axial current is constrained to zero in the flow, i.e., $j_x = 0$. The topic of electrode segmentation has been studied in the past for MHD converters by various researchers, with some of the most informative conclusions being reported in Ref. [44] by Rosa. Figure 5.15 presents a schematic with the notation to aid this discussion.

By segmenting the electrodes to a finite width, c, the effective Hall parameter and plasma conductivity are lowered across the channel. The factor by which this occurs is also a function of

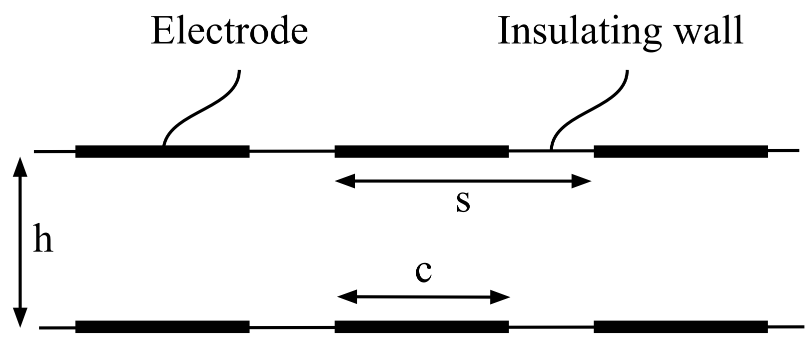

Figure 5.15: **Segmented electrode schematic with notation.**

the channel width, h. The formula in Eq. 5.3 was proposed to account for this effect.

$$\frac{\sigma_{eff}}{\sigma_{calc}} = \frac{\beta_{eff}}{\beta_{calc}} \approx \frac{1}{1 + \frac{s}{h}(\beta - 0.44)} \tag{5.3}$$

Furthermore, another formula was proposed to define the optimal electrode spacing and is provided in Eq. 5.4. The optimal electrode spacing, in this case, is defined by the ratio of the length of the electrode in the axial direction to the length of the electrode and adjacent insulating wall section, s.

$$\left.\frac{c}{s}\right|_{opt} = 1 - \frac{\arctan(\beta)}{\frac{\pi}{2} + \arctan(\beta)} \tag{5.4}$$

The effective conductivity, effective Hall parameter, and optimal electrode spacing in the finite electrode segmentation model depend on the calculated Hall parameter, β. As the Hall parameter increases past unity, the theoretically optimal spacing goes to 0.5 quickly, meaning the insulating wall regions should be as long in the axial direction as the electrodes. At c/s ratios above 0.5, it has been suggested that axial currents between electrodes may be large and lead to breakdown. Similarly, the effective conductivity and Hall parameters are also reduced as the Hall parameter increases. Figure 5.16 illustrates the behavior of these two quantities as a function of the calculated Hall parameter for $s/h = 0.1$, $s/h = 0.5$, and $s/h = 1.0$. As the electrode length to channel width ratio grows, so does the reduction in σ_{eff} and β_{eff} at high Hall parameters.

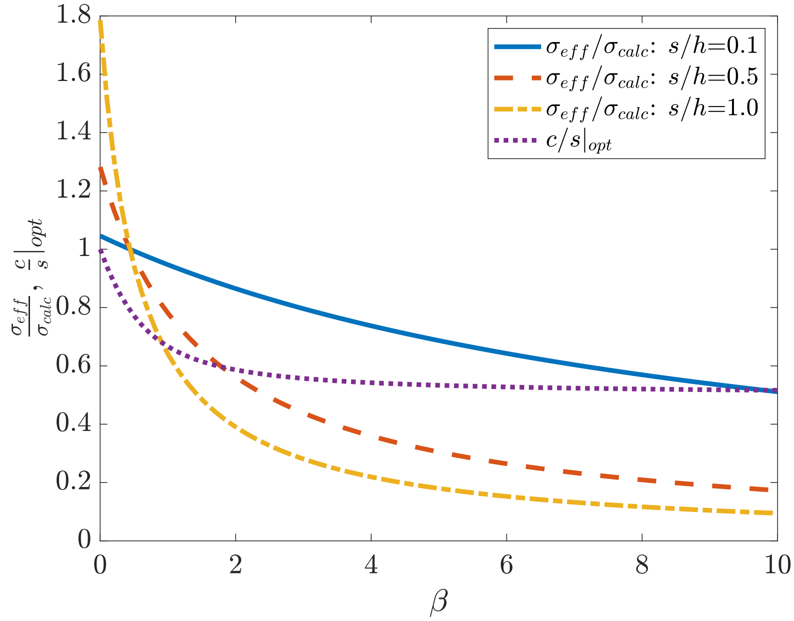

Figure 5.16: **Effective conductivity and optimal electrode spacing versus Hall parameter.**

However, at lower calculated Hall parameters, the effective quantities can actually be greater than the calculated values, especially as s/h is increased.

For altitudes less than 20 km, the electrode spacing may be very dense as the axial fields will not be strong. However, at the lower pressures above 20 km, it is recommended that the electrode spacing be increased. The length of the insulating walls in between the electrodes should be as long as the electrodes themselves. Furthermore, caution be exercised when designing narrow channels with respect to the electrode spacing. As s/h increases above unity, the effective conductivity and Hall parameter will more than double the calculated value.

5.4 Two-Dimensional Simulations with the Hall Effect

Finally, the influence of the Hall effect on a two-dimensional simulation is explored. This simulation represents flow through ten pairs of electrodes that are equally spaced. The electrodes are 1 cm long, with 1 cm spacing between them, as per the recommendations outlined in the previous section. The boundary conditions are the same as the two-dimensional test case, Mach 5 flow at 20 km, to highlight the impact of segmented electrodes and the Hall effect on the electric and flow fields. The channel height is 10 cm, and the length is restricted to the domain that contains the electrodes, i.e. 190 cm. The magnetic field strength is 1 T, and the degree of ionization is constant in the domain at $\alpha = 1 \times 10^{-4}$.

The electron mobility is also held constant through the domain to conduct an initial investigation of the Hall effect. The segmented electrodes are independently biased to generate electric fields in the transverse and axial directions. The voltage difference for each electrode pair is prescribed based on the inlet velocity, $u = 1500$ m/s, and the height of the channel, $h = 0.1$ cm, such that the applied field is 1.5 times stronger than the induced field, i.e., $E_z = -1.5E_3$ (load parameter, $k = 1.5$). Thus, the voltage drop at each pair is $\Delta\phi_z = 225$ V. Then, an axial field is prescribed to generate a transverse current density at high Hall parameters. The Hall parameter in this section is $\beta_e = 5$, representing the value at the freestream conditions and electric fields in this simulation according to a BOLSIG+ calculation for pure nitrogen. The axial electric field strength needed to offset the Hall current is $E_x = -\beta_e(k-1)E_3$. For a 0.19 m long channel, the voltage drop between the first and last pair of electrodes is then $\Delta\phi_x = 712.5$ V, resulting in a nominal transverse field, $E_z = -2250$ V/m, and a nominal axial electric field, $E_x = 3750$ V/m. The electric potential at each pair is prescribed by the values listed in Table 5.2 to generate such an electric field configuration with ten electrode pairs, where x_c is the electrode pair centroid in the axial direction, ϕ_a is the voltage prescribed at the top wall ($z = h/2$), and ϕ_c is the voltage at the bottom wall ($z = -h/2$).

Since the electron mobility is set constant throughout the domain, the scalar electrical conductivity is a function of the electron number density. The tensor conductivity is thus a function of the electron number density, the electron mobility, and the magnetic field strength. Ion slip is neglected. The electric potential is found by solving the multi-dimensional generalized Ohm's law in Chapter 2 using tensor conductivity. Electric potential contours are shown for the entire domain in Fig. 5.17.

The electric field strength at each point is the gradient of the electric potential. A gradient

Table 5.2: Electric potential boundary conditions for two-dimensional case with the Hall effect.

x_c (m)	ϕ_a (V)	ϕ_c (V)
0.005	112.5	-112.5
0.025	33.30	-191.7
0.045	-45.80	-270.8
0.065	-125.0	-350.0
0.085	-204.2	-429.2
0.105	-283.3	-508.3
0.125	-362.5	-587.5
0.145	-441.7	-666.7
0.165	-520.8	-745.8
0.185	-600.0	-825.0

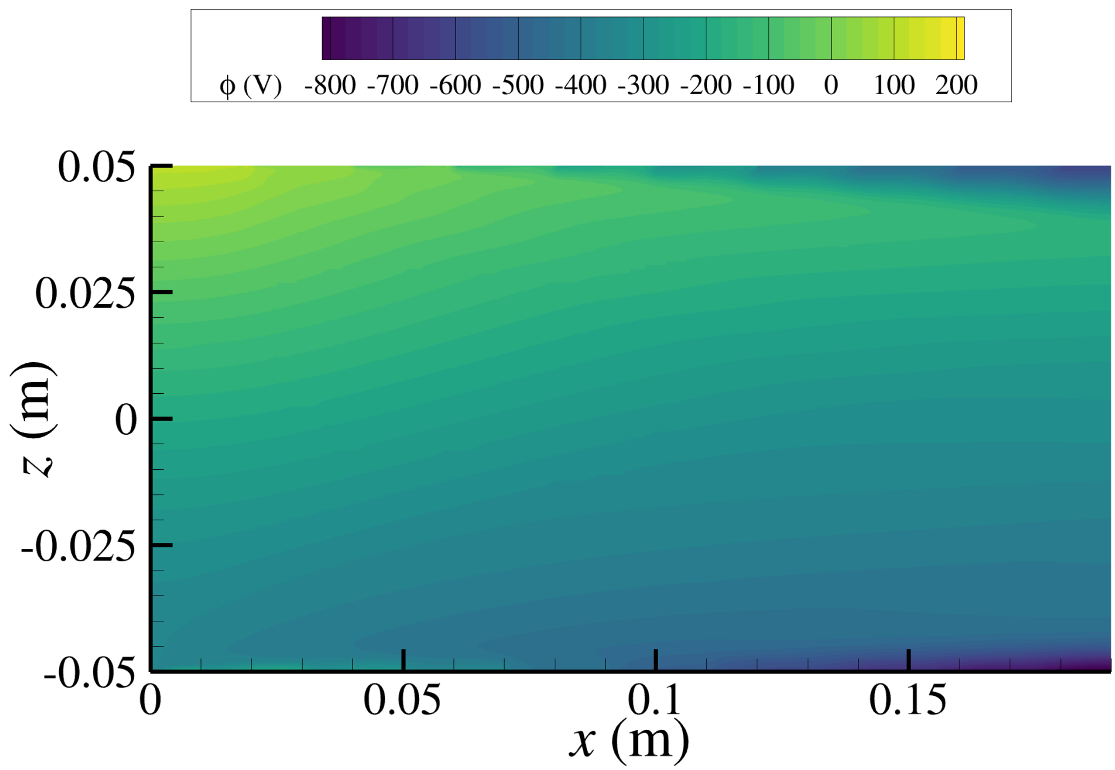

Figure 5.17: **Electric potential contours for two-dimensional case with tensor conductivity.**

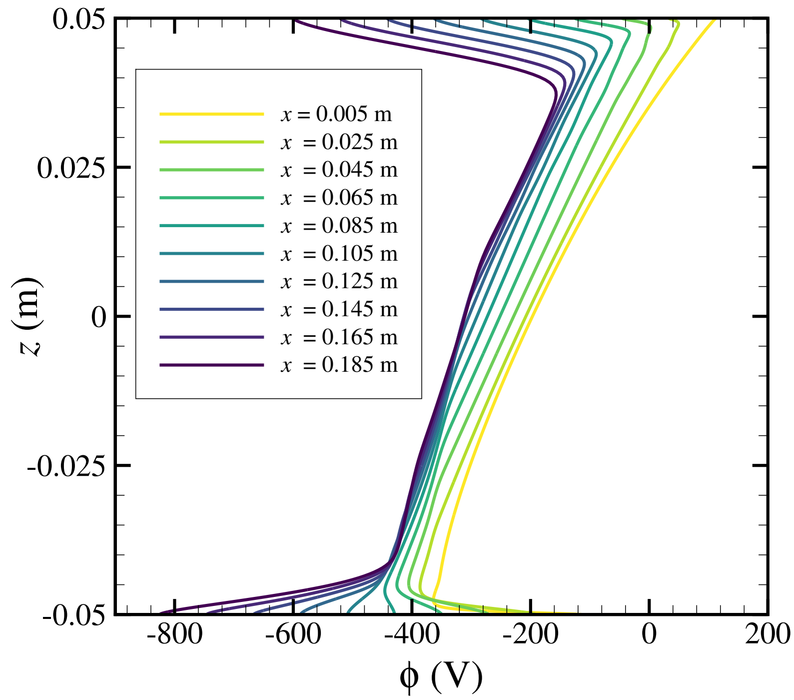

Figure 5.18: **Electric potential profiles across the channel for two-dimensional case with tensor conductivity.**

in the axial direction can be observed in the electric potential contours in Fig. 5.17. However, a strong transverse component of the gradient is still present, especially near the inlet and outlet boundaries where the gradient-free constraint is applied. Near the downstream electrodes, a large gradient forms in the z-direction. Figure 5.18 shows electric potential profiles across the channel at the mid-point of each electrode pair.

At the center of the channel, the electric potential gradient is nearly constant in the axial direction. However, a significant variation can be seen near the electrodes. Near the inlet, the electric potential at the bottom wall initially decreases before increasing with distance in the z-direction. The gradient near the bottom wall decreases with axial distance until the electric potential increases with increasing z-direction downstream in the channel. Then, near the top wall, the gradient reverses direction such that the electric potential decreases. The point at which the gradient changes direction gets further from the wall as the axial distance increases.

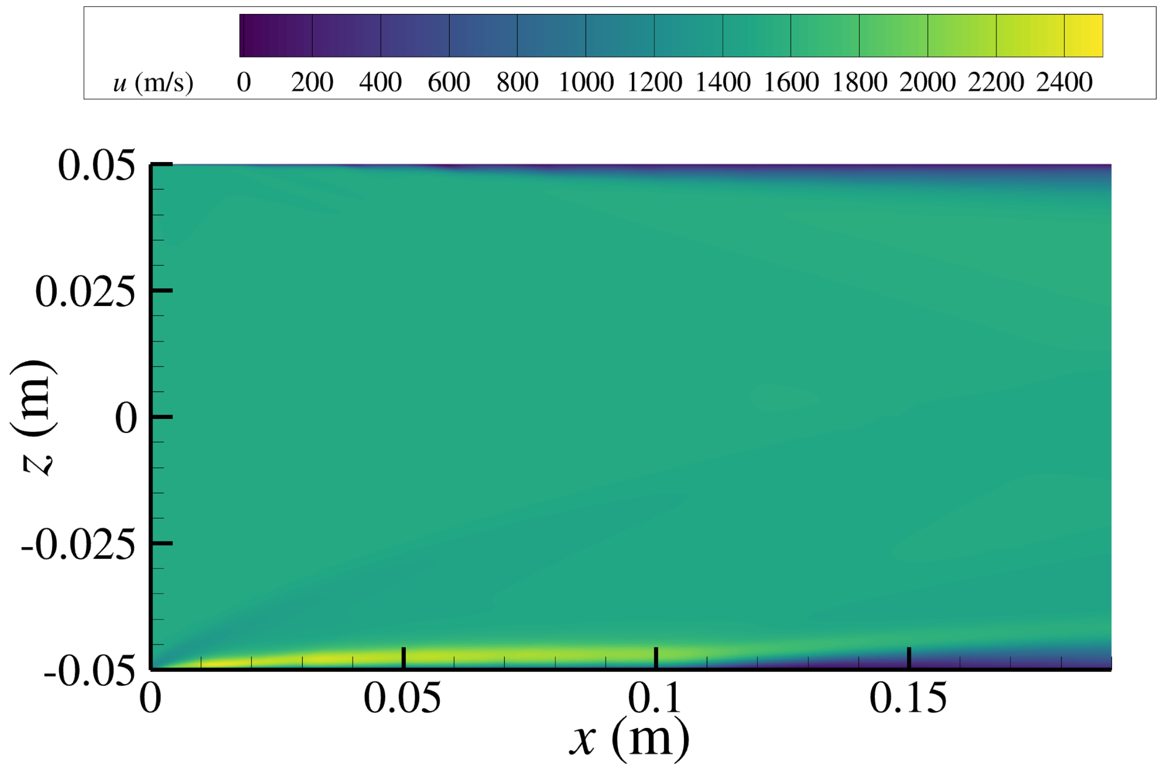

Figure 5.19: **Velocity contours for two-dimensional case with tensor conductivity.**

Near the bottom wall, where the electric potential gradient and thus the electric field in the z-direction, E_z, is the largest, the amount of energy deposition is also the largest. Acceleration and Joule heating are also the most prominent in this region. Figure 5.19 shows velocity contours in the two-dimensional channel with tensor conductivity.

Very little acceleration occurs in the core flow with tensor conductivity and uniform electron mobility. Most of the flow is moving at 1500 m/s, which is the prescribed inlet velocity. Meanwhile, the peak velocity in the bottom wall boundary layer is 2400 m/s upstream in the channel, which resembles the velocity overshoot phenomenon from the prior discussion. However, the underlying mechanism of the velocity overshoot in these simulations differs from the velocity overshoot

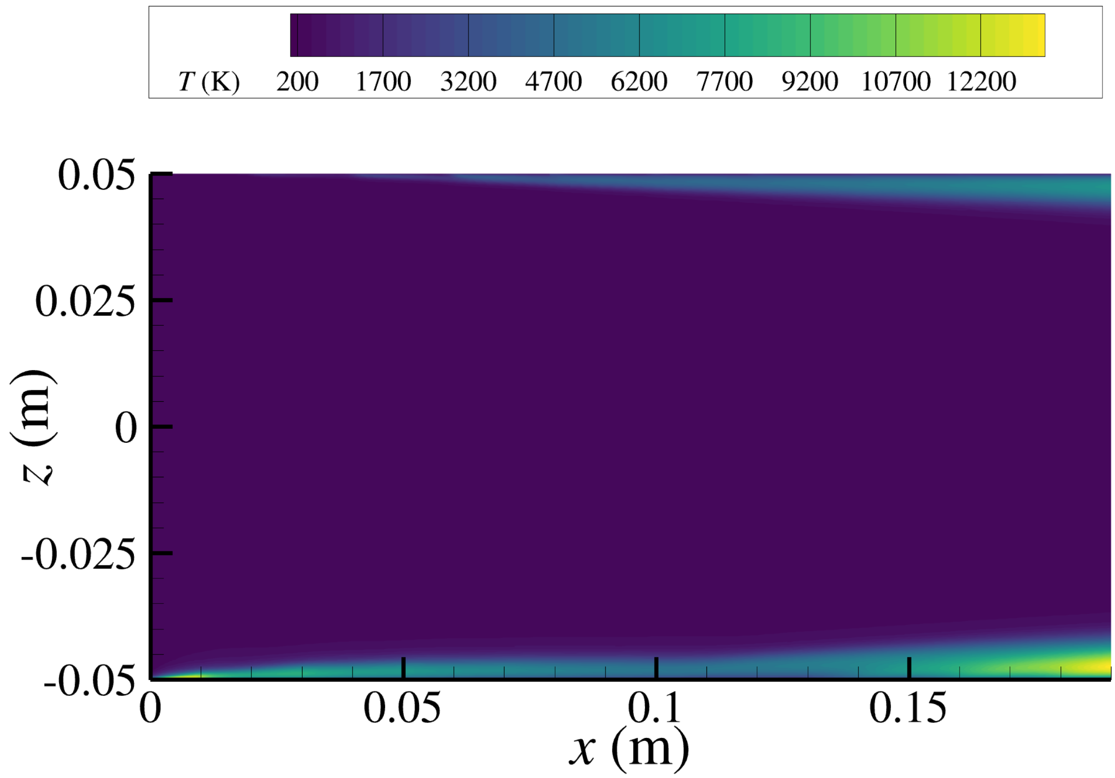

Figure 5.20: **Temperature contours for two-dimensional case with tensor conductivity.**

that may be seen in physical systems. While the velocity overshoot in a physical system may be caused by thermal ionization due to high temperatures in hypersonic boundary layers, the velocity overshoot in these simulations is due to an increased density where temperatures are high, which leads to increased electron density since the degree of ionization is held constant. With increased electron number density comes increased electrical conductivity. Although the increased electrical conductivity does not occur through thermal ionization, these simulations still highlight the effect of high temperatures in the boundary layer. Figure 5.20 shows temperature contours in the two-dimensional channel with tensor conductivity.

Similar to the behavior of the velocity contours in Fig. 5.19, the peak temperatures also occur in the boundary layers, especially near the bottom wall. Namely, temperatures above 10,000 K occur in the boundary layer downstream in the channel due to viscous dissipation and Joule heating. Thermal ionization will occur at these elevated temperatures, inevitably leading to the difficulties discussed earlier in the chapter.

There are several challenges when simulating partially ionized channel flows under applied electromagnetic fields using the present MHD formulation. In numerical simulations of hypersonic flows, the governing equations become *stiff* due to the thermochemical nonequilibrium source terms. With the addition of the Lorentz force term and total energy deposition term, the equations may become even more unstable if the applied fields are strong. Caution must be exercised when choosing simulation parameters such as simulation time step size and grid refinement. Overrefinement near the edges of the electrodes with the present boundary condition formulation causes severe electric potential gradients that cause the entire simulation to become unstable. In this work, the generalized Ohm's law solver uses a successful over-relaxation (SOR) method in which a relaxation parameter must also be chosen carefully before simulation. Otherwise, the electric potential solution becomes unstable. Since a Dirichlet boundary condition is imposed at electrodes, and a Neumann condition is imposed at insulating walls, a more sophisticated mixed boundary condition treatment may alleviate the burden of overrefinement near the electrode-wall boundaries in future work. Furthermore, electrode sheath boundary conditions should be considered for non-neutral regions near the boundaries.

It is essential to highlight the significance of the assumptions used in these multi-dimensional numerical simulations. As discussed in the previous chapter, recombination may be fast, especially at altitudes below 40 km. However, the numerical simulations in this chapter did not include recombination. Although recombination leads to decreased electrical conductivity, it may help dampen some of the deleterious effects of Joule heating and viscous dissipation. Furthermore, thermal nonequilibrium was not considered. In these simulations, the energy was deposited solely into the translational mode. However, a significant amount of the applied electromagnetic energy is also deposited into the vibrational mode for molecular systems. Although including vibrational energy deposition would lead to enhanced dissociation (introducing additional stiffness to the source terms), decreased peak translational temperatures would occur in the simulations. A three-temperature model can also be employed in which the free electron energy equation is solved separately from the vibrational energy equation, and energy relaxation is accounted for between the translational and vibrational modes. However, this increases computational complexity and makes simulations of physical systems even more computationally expensive. LeMANS-MHD also assumes a single fluid, which makes the simulation of vehicle scale geometries more tractable. However, a more detailed physical representation may improve the outlook of magnetohydrodynamically accelerating low-pressure hypersonic channel flows using the configuration described in this section. Furthermore, increased physical fidelity may improve the stability of these simulations. Given the promise outlined in the previous chapters, additional research in this direction is warranted.

5.5 Conclusion

Multi-dimensional simulations of hypersonic MHD accelerated channel flows were performed in this chapter using LeMANS-MHD. A two-dimensional test case was presented to facilitate discussion regarding the MHD boundary conditions that have been implemented. The test case represented two-dimensional flow between two continuous electrodes under constant ionization and scalar conductivity. It was found that the core flow was accelerated by the Lorentz force while simultaneously experiencing Joule heating. When the centerline solution was plotted in velocity versus Mach number space, it was found that the numerical solutions agreed with the one-dimensional theoretical predictions well. However, it was also noted that significant nonuniformity occurs in the spanwise direction as Joule heating and viscous dissipation cause peak temperatures in the boundary layers. These nonuniformities can lead to instabilities if the temperatures become high enough to cause thermal ionization.

Then, a three-dimensional simulation of flow through an MHD accelerator geometry based on a prior facility was performed. This simulation highlighted the electric field and flow field structure in a segmented electrode configuration. It was found that the Lorentz force has to overcome both adverse pressure gradients due to Joule heating along with viscous deceleration. This is coupled with the fact that nonuniform conductivity and electric field strengths exist across the channel that cause inefficient acceleration. In regions between electrode pairs, the electric field is weakened, thus decreasing Lorentz force acceleration. The centerline solutions were again plotted in velocity versus Mach number space to compare the three-dimensional behavior to the one-dimensional prediction. Although the three-dimensional solutions contain more information than is accessible by the one-dimensional model, it was shown that the one-dimensional model may provide value through parametric trade studies to find effective PFE configurations.

Finally, multi-dimensional simulations with tensor electrical conductivity were described. The electron mobility was held constant throughout the domain, and the segmented electrodes were biased according to the electron mobility, the inlet velocity, and the magnetic field strength. However, it was seen how challenges arise for both simulating and operating low-pressure hypersonic MHD accelerators. Several instabilities arise that can be attributed to either physical or numerical natures. The physical instabilities, such as the Joule heating instability, occur due to strong electric fields and local increases in electrical conductivity. The numerical instabilities mimic the physical instabilities due to local increases in electric field and conductivity. However, the numerical simulations in this chapter did not include ionization or any other chemical reaction. The significance of assumptions that were employed in this chapter was discussed. Although simulating physical systems with increased fidelity may increase the computational complexity, the outlook of this technology may be improved along with the behavior of the numerical simulations. Regardless, continued investigation into the physical and numerical models used in vehicle-scale multi-dimensional simulations is justified.

Chapter 6

Conclusion

This dissertation studied an electromagnetic engine concept for hypersonic flight at high altitudes, called the plasma fueled engine, or PFE. The PFE is an example of a magnetohydrodynamic (MHD) accelerator channel that uses the Lorentz force to accelerate the working gas and generate thrust. This technology differs from pre-existing electric propulsion devices such as the Hall effect thruster and gridded ion thruster because it is an airbreathing engine. As the oncoming air travels into the accelerator channel, it is first ionized via high-energy electron beams, an efficient means for ionizing cold low-pressure gases. Then, once the air is ionized enough to be sufficiently electrically conductive, it is accelerated via crossed electromagnetic fields. The electric fields are generated by a series of segmented electrodes on opposing sides of the channel, and the magnetic fields are generated by strong electromagnets on board the vehicle. As the electrons drift in the electric field direction, they gyrate around the magnetic field lines and collide with the neutrals, adding momentum to the flow.

There have been several attempts to model and design high-speed MHD accelerators previously. However, most have focused on higher-pressure gases in wind tunnel applications. The objective in these wind tunnels was to generate very high pressure and temperature gases that would then expand in nozzles to high speeds. As the working gases were accelerated towards the test section, MHD accelerator channels were used to add total enthalpy to the flow. However, for electromagnetic interaction to be possible, sufficient electron populations were necessary. The most common ionization mechanism at the time was seeding with vaporized alkali metals since they have low first ionization energies. Once the electrons are removed from their atomic orbits, they can interact with the applied electromagnetic fields and the working gas, typically air or nitrogen, in these wind tunnels. Unfortunately, leveraging the low ionization potential of alkali metals does not come without several disadvantages. As flow velocity increases, it becomes more challenging to adequately mix the seed with the working air. For wind tunnel applications, seeding comes with the even more significant complication of polluting the freestream gas purity, leading to corrosion of both the wind tunnels and the test sections. For testing airbreathing engines like scramjets, the purity of the freestream air is a primary concern for developing wind tunnel facilities. Although freestream air purity is not a concern for air-breathing hypersonic engine concepts, mixing and wall corrosion are. Furthermore, seeding would require extra weight, decreasing payload capabilities.

Interest in high-speed MHD accelerators disappeared almost entirely in the 1970s and 1980s as investment in hypersonic technologies waned. Furthermore, several engineering problems were yet to be resolved. MHD generators, which operate in the opposite mode of accelerators by converting the flow's kinetic energy into electromagnetic energy, saw continued investment as they showed potential in improving power generation efficiencies in steam turbine-based facilities. However, these systems still had challenges, such as nonequilibrium instabilities that were not overcome until after the original attempts in the 1960s had already passed [106, 107, 108].

Today, hypersonic research and technology development has seen a resurgence in funding, with the Pentagon investing \$4.7 billion in hypersonic research for FY2023 and the global space economy as a whole exceeding \$400 billion in 2022 [109, 110]. With this renewed interest, significant resources have been dedicated to solving some of the most critical challenges surrounding hypersonic vehicle development, including innovative approaches to achieving hypersonic propulsion outside the current operational envelope of today's capabilities, such as the PFE. In many hypersonic applications, analytical, experimental, and numerical studies are necessary to arrive at practical solutions for these challenges. The goal of this dissertation was to advance the state-of-the-art understanding and design of these hypersonic MHD accelerators through numerical modeling.

6.1 Summary and Contributions

The PFE was introduced in Chapter 1 and put into historical context versus other hypersonic engine technologies, such as rockets and scramjets, and other notable MHD accelerator programs over the past half-century. Due to the complex nature of these systems, namely electromagnetic acceleration of low-pressure hypersonic flows, analytical and numerical studies are needed before development can proceed since hypersonic ground testing facilities remain a precious resource.

Chapter 2 presented the sets of equations that govern the behavior of MHD-augmented hypersonic flows, Maxwell's equations of electromagnetics, and the Navier-Stokes equations for compressible flows under thermochemical nonequilibrium. Then, an approach for coupling the two sets of equations was described under the low magnetic Reynolds number assumption. Under this assumption, the magnetic induction equation is no longer solved, and the appropriate MHD source terms are added to the conservation equations. The multi-dimensional parallelized finite volume hypersonic CFD code used to discretize and solve these equations, LeMANS-MHD, was described in detail. LeMANS-MHD couples the flow field to the electromagnetic field via a finite volume generalized Ohm's law solver, which solves for the electric potential in the domain. Once the electric potential is known, the electric field and the current density can be calculated using an appropriate model for electrical conductivity. Since the magnetic field is prescribed throughout the domain, the Lorentz force is simple to compute once current density and electrical conductivity are known. However, strong magnetic fields significantly alter the trajectories of charged particles in electric fields, leading to the commonly known Hall effect. As the magnetic field intensifies, tensor electrical conductivity is needed to capture the behavior of the fluid in directions parallel and transverse to the field lines. A simplified quasi-one-dimensional inviscid MHD model was then presented that can be used to quantify the magnetic field effects and make baseline performance predictions for PFEs at different operating conditions.

The one-dimensional PFE model is the first major contribution of this thesis. The code is written in Matlab and can run in a matter of minutes (as opposed to hours for larger MHD/plasma codes) and provides highly valuable design intuition and understanding for PFE prototypes. Although the model neglects higher dimensional and viscous effects, it can still capture some of the most dominant physical processes in MHD channel operation, such as ionization, recombination, and tensor conductivity. The model is ready-to-use, and all of the necessary information for argon-based systems is self-contained. Vibrational nonequilibrium models have also been implemented for molecular species. Finally, a validation study was outlined using exact solutions to the one-dimensional MHD augmented Euler equations, and the expected convergence rate was achieved.

The one-dimensional MHD equations of motion were used in Chapter 3 to expand upon the classical relations of gas dynamics. Theoretical performance predictions for MHD channels were made nearly sixty years ago; however, they have been largely forgotten in modern numerical studies. Although analytical solutions were found under several assumptions, their conclusions are still very useful to the design and simulation process. Using just the velocity and Mach number at the inlet, the behavior of the flow downstream can be predicted. For example, one of the primary outcomes of this discussion is that for a fixed magnetic field strength, improved performance is not guaranteed by using strong electric fields. As the electric field strength increases, a disproportionate amount of energy is deposited into Joule heating. The limits to this regime and the appropriate operating envelope for hypersonic MHD accelerators based on these theoretical analyses were outlined. Although this approach is limited to idealized operating conditions and PFE configurations, the discussion outlined in 3 provides firm intuition for future researchers interested in high-speed MHD acceleration based on decades-old literature that is either difficult to access or scantly cited.

The Hall effect and its implication on the tensorial nature of electrical conductivity is a critical aspect to model when designing prototypes. The optimal MHD channel configuration is a function of the Hall parameter. The Faraday configuration channel is most effective at generating thrust at very low Hall parameters. However, as it approaches unity, the orientation of the electric field with respect to the flow and magnetic field must change. At high altitudes where the PFE may operate, subatmospheric pressures lead to low collision frequencies such that the Hall parameter is often much greater than unity. The Hall configuration channel is more effective at these conditions than the Faraday condition. Hall parameter estimates using first-order collision frequency calculations were provided. It was found that at altitudes 20 km and above, the electron parameter will be greater than unity at realistic electron energies, and channels at these operations should be configured in the Hall mode. Furthermore, the degree of ionization requirements at different altitudes were quantified based on the amount of magnetic interaction at each. Along with the preceding theoretical discussion, these calculations help define the operating envelope of the PFE and provide a basis for setting up numerical simulations.

One-dimensional solutions were presented in Chapter 4 using the model described in Chapter 2. Several regimes of MHD augmented channel flows were explored using the one-dimensional model. The impact of subsonic boundary conditions on the steady-state flow structures was investigated for initially subsonic and initially supersonic flows. The behavior of the solutions matches the behavior predicted by the one-dimensional theory. However, it was found that for an initially supersonic flow, the Joule heating caused by exceedingly strong electric fields with respect to the magnetic field can cause the flow to become subsonic in the channel, forming a shock-like structure. This structure propagates upstream and eventually passes through the inlet, where total temperature and momentum are conserved, and the entire flow becomes subsonic. Then, if the electrical conductivity is high enough, the flow may become supersonic again downstream of the inlet. Regardless of the initial conditions, the final solution in this regime will lie on the same curve in velocity versus Mach number space. This curve passes through Mach one at a very specific velocity, which exactly matches the theoretical prediction. Thus, along with providing design intuition, the one-dimensional theory has also provided the ability to verify the one-dimensional model described in Chapter 2.

A parameter sweep was performed across multiple design variables using the theoretical guidelines for prescribing the electromagnetic field strength in a hypersonic MHD accelerator. The first of which, the electric field, was varied between the two bounds for smooth acceleration. It was found that with increasing electric fields and Lorentz force acceleration, peak temperatures also increased due to Joule heating. Then, two more design variables were varied to find more efficient

PFE configurations in which heating was mitigated while achieving high acceleration. Since the Lorentz force is opposed by adverse pressure gradients caused by Joule heating, increasing the cross-sectional area of the channel improves performance by allowing the flow to expand while it is being accelerated. Finally, very efficient acceleration can be achieved by also varying the electric field down the length of the channel to limit the Joule heating. Although analytical solutions are not available for configurations with variable cross-sectional areas and electric field strengths, it was shown that the one-dimensional model can readily provide numerical solutions for PFE design.

However, before predictive PFE analysis can occur, the appropriate plasma transport and chemistry models must be identified and implemented. These models, namely, of electron mobility, ionization, and recombination, were presented and described for argon. It was found that a single electron beam region upstream of the electrodes would not be enough to sustain electron populations sufficient for MHD interaction for altitude conditions lower than 40 km. Furthermore, at these conditions, the Hall parameter is likely to be large (with respect to unity), and a tensorial description of electrical conductivity is necessary. Finally, numerical simulations were performed for a Hall configuration channel for a flight condition relevant to PFE operation. Performance predictions were given for a range of freestream Mach number and altitude conditions. The coefficient of thrust decreased with increasing Mach number due to the increase in dynamic pressure that the engine must overcome. Furthermore, with higher inlet Mach numbers, the flow must go through a more substantial Joule heating phase before acceleration occurs. However as the engine climbs in altitude and freestream density decreases, the engine is still able to provide thrust since MHD acceleration is not dependent on flow compression. In fact, the coefficient of thrust increased with an increase an altitude. The results from this analysis suggest that thrust can be obtained at hypersonic Mach numbers and altitudes between 40 km altitude and 50 km. Lorentz efficiency, which is the ratio of energy deposited through heating to the energy converted into acceleration, was also computed for the same operating conditions. Lorentz efficiency also decreased with increasing Mach number for the electric field configuration in this analysis for the same reason as the coefficient of thrust. Although Lorentz efficiency does not account for the various losses in a physical MHD channel, it does quantify the effectiveness of a given electromagnetic field configuration in the ideal limit.

Multi-dimensional simulations were performed in Chapter 5. A two-dimensional test case was developed to facilitate discussion about the fluid and electromagnetic boundary conditions implemented in LeMANS-MHD. This test case consisted of flow through two parallel continuous electrodes. It was found that the behavior of the solution at the centerline agreed with the one-dimensional solutions in velocity versus Mach number space. One of the benefits of using a higher-dimensional framework for analyzing MHD accelerated channel flows is that detailed flow structures around segmented electrodes can be investigated. Again, the pioneering MHD channel work of the 1960s provides guidelines for segmenting electrodes to combat the Hall effect. Three-dimensional simulations of an MHD accelerator geometry were performed that included viscous effects and electrode segmentation. It was found that nonuniformities in the flow profiles between electrodes and in the spanwise direction limit acceleration. These nonuniformities occur even under assumptions of constant ionization and scalar conductivity, and it is expected that these effects may worsen as the Hall effect is included. Nonetheless, it was found that the centerline solutions still qualitatively match the one-dimensional theoretical and numerical predictions. Finally, a two-dimensional simulation with the Hall effect was performed for constant electron mobility. Several numerical and physical challenges of low-pressure hypersonic MHD accelerators were discussed. Numerical instabilities in the flow and electric potential solver arise from overrefinement and local increases in electric field strength and conductivity using the present numerical formulation. These instabilities are linked to physical instabilities discussed in previous MHD accelerator studies. Velocity overshoot occurs in the boundary layer due to increased electric field strengths near the electrodes. Similarly, Joule heating and viscous deceleration cause prohibitively high temperatures near the walls. Several assumptions were made in this work to reduce computational complexity. However, relaxing these assumptions may increase physical fidelity at the cost of computational resources. The performance predictions may improve by including thermochemical nonequilibrium in the numerical simulations. Suggestions for future work to continue these analyses are given below.

6.2 Future Work

Although this work has implemented and used state-of-the-art physical and numerical models to improve the design and simulation of hypersonic MHD accelerators, more work is needed before enough confidence can be instilled in the numerical simulations such that they can be used to mature the technology to the next stage of development. However, the studies performed in this dissertation have highlighted the promise of applying MHD acceleration to low-pressure hypersonic flows. The following tasks are recommended for future work to continue PFE development.

6.2.1 Use the One-Dimensional Model to Analyze Molecular Species Such as Air and Pure Nitrogen

The one-dimensional model described in Chapter 2 and applied in Chapter 4 to investigate the behavior of one-dimensional MHD accelerated channel flows was only used for argon plasmas. This choice was made because of the simplified ionization kinetics and lack of rovibrational states for argon in its ground state. Furthermore, argon is commonly used in wind tunnel facilities that might be used for testing prototypes. While argon helped develop design intuition and extend the one-dimensional theory beyond constant/scalar electrical conductivity, electric field strengths, and cross-sectional areas, it does not fully represent conditions that future vehicles will experience. Free electrons in a molecular plasma will exchange energy with bound electrons, which are closely coupled to the vibrational energy of the molecule. Thus, Joule heating not only increases average translational energy but also increases average vibrational energy. This effect is captured via the energy partitioning constant, η_{vee}, in the conservation of vibrational-electronic-electron energy, which was previously implemented in LeMANS. However, this term has yet to be implemented in the one-dimensional model.

The necessary routines for two-temperature thermal nonequilibrium between the vibrational and translational modes have been implemented but have yet to be tested and applied to air. These routines calculate the vibrational-electronic-electron temperature using a Newton iterative solver, the energy lost in dissociation by a simple preferential model, and relaxation between the two modes using the Landau-Teller model [70]. A three-temperature model with an additional equation for electron energy should be explored and compared to the two-temperature approach. This may come with an increase in fidelity, however, an increase in numerical stiffness is expected due to the short characteristic time scales of electron-dominated processes. Furthermore, the one-dimensional model can be used to determine the impact of excited species on PFE performance, making it a good candidate for conducting sensitivity analyses. Since the one-dimensional model is not computationally intensive, optimization studies can easily be performed by using MATLAB's built-in Optimization Toolbox.

6.2.2 Perform Two-Dimensional and Three-Dimensional Simulations of Wind Tunnel Scale Geometries

The two- and three-dimensional simulations in Chapter 5 represent baseline simulations of low-pressure hypersonic MHD accelerated channel flows, but further research is warranted to simulate practical PFE configurations. Primarily, tensor conductivity is needed for high-altitude flight, as was quantified in Chapter 3. Numerical convergence can be difficult to obtain in the presence of strong Hall fields. With segmented electric fields, extremely strong source terms near the walls cause simulations to become unstable. More sophisticated boundary conditions near electrodes should be investigated. The electrode boundary conditions are simple Dirichlet conditions, but voltage drops may be expected in the sheaths/boundary layers. As such, the appropriate sheath models should be identified and implemented. Furthermore, it may be necessary to compute the charged particle transport equations separately from the bulk momentum equation since non-neutrality may be significant in sheaths. Similar to the one-dimensional model, an additional conservation equation for the electron energy may be necessary. The simulations in Chapter 5 did not include thermal nonequilibrium between the vibrational and translational modes. In physical systems, a significant portion of the applied electromagnetic energy will be deposited into the vibrational modes, such that the vibrational temperature is controlled by electromagnetic field strength, dissociation, and relaxation with the other modes of internal energy. Although incorporating dissociation introduces additional computational complexity, the performance of MHD accelerated hypersonic channel flows may improve if all of the applied electromagnetic energy is not directly deposited into the translational mode.

Additionally, recombination and electron beam ionization were not included in the present simulations. Routines have been added to LeMANS to compute electron beam ionization but have yet to be applied to multi-dimensional simulations. Namely, with a new input file, users can define electron beam locations and the ionization mechanisms for the species of interest during problem setup.

Viscous effects on PFE performance were described in Chapter 5. Namely, it was found that the Lorentz force needed to be strong enough to overcome adverse pressure gradients and viscous deceleration in a three-dimensional geometry for significant acceleration to occur. Furthermore, it was highlighted that temperatures may become very high in the boundary layers due to the combination of Joule heating and strong velocity gradients. However, all of the simulations in this work were done assuming laminar flow. Thus, future work should include turbulence modeling to investigate the impact of electromagnetic forcing on turbulent boundary layer growth. LeMANS contains several Reynolds-averaged Navier-Stokes (RANS) models that have yet to be coupled to the MHD routines.

6.2.3 Acquire Experimental Data to Test the Feasibility of Low-Pressure Hypersonic MHD Accelerators and Benchmark Numerical Tools

Finally, perhaps the most critical task in ensuring the continued development of the systems discussed in this work is generating wind tunnel data of low-pressure hypersonic MHD accelerators. Experimental data will be extremely valuable to evaluate the feasibility of using MHD accelerators for hypersonic propulsion and solve some of the engineering issues that come with designing and manufacturing such complicated devices. For example, several analytical and experimental studies, such as the ones mentioned earlier in this Chapter, from the mid-twentieth century discussed the possibility of plasma instabilities at high Hall parameters. For MHD acceleration to become a realistic option for hypersonic thrust generation, it will be critical to explain these instabilities and quantify the conditions in which they occur. Unforeseen discoveries will likely be made in ground testing that must be explained via modeling. Ultimately, analytical and numerical models are most valuable when they can be adequately validated by high-quality experimental data. Although wind tunnel testing may not replicate every aspect of flight relevant to the PFE, successfully validated models can be confidently used to simulate more extreme operating conditions.

Bibliography

[1] N. J. Bisek, Numerical Study of Plasma-Assisted Aerodynamic Control for Hypersonic Vehicles. PhD thesis, University of Michigan, 2010.

[2] "X-43A Image Gallery - NASA." https://www.nasa.gov/centers/armstrong/multimedia/imagegallery/X-43A/index.html. Accessed: 2023-09-16.

[3] S. E. Cusson, B. A. Jorns, and A. D. Gallimore, "Non-invasive *in situ* measurement of the near-wall ion kinetic energy in a magnetically shielded hall thruster," Plasma Sources Science and Technology, vol. 28, no. 10, 2019.

[4] M. Mitchner and C. H. Kruger, Jr, Partially Ionized Gases. Wiley, New York City, NY, 1973.

[5] F. E. C. Culick, "Compressible magnetogasdynamic channel flow," Journal of Applied Mathematics and Physics (ZAMP), vol. 15, pp. 126–143, 1964.

[6] D. W. Bogdanoff and U. B. Mehta, "Experimental demonstration of magneto-hydro-dynamic (MHD) acceleration," 34th AIAA Plasmadynamics and Lasers Conference, AIAA Paper 03-4285, 2003.

[7] BAE Systems, "BAC Concorde." https://www.baesystems.com/en/heritage/bac-concorde. Accessed: 2023-10-02.

[8] NASA Facts, "SR-71 Blackbird." https://www.nasa.gov/wp-content/uploads/2021/09/495839main_FS-030_SR-71.pdf. Accessed: 2023-10-02.

[9] C. Gelzer, "X-43A Hyper-X." https://www.nasa.gov/centers-and-facilities/armstrong/x-43a/, 2014. Accessed: 2023-10-02.

[10] United States Air Force, "X-51A Waverider." https://www.af.mil/About-Us/Fact-Sheets/Display/Article/104467/x-51a-waverider/. Accessed: 2023-10-02.

[11] C. Park, Nonequilibrium Hypersonic Aerothermodynamics. Wiley, New York City, New York, 1990.

[12] J. J. Bertin, Hypersonic Aerothermodynamics. American Institute of Aeronautics and Astronautics, Washington, D.C., 1994.

[13] M. Evans, The X-15 Rocket Plane: Flying the First Wings into Space Flight Log. Mach 25 Media, 2020.

[14] J. L. Hunt and J. G. Martin, "Rudiments and methodology for design and analysis of hypersonic air-breathing vehicles," in Scramjet Propulsion (E. T. Curran and S. N. B. Murthy, eds.), vol. 189 of Progress in Astronautics and Aeronautics, pp. 939–978, AIAA, Reston, VA, 2001.

[15] J. W. Hicks, "Flight testing of airbreathing hypersonic vehicles," NASA TM 4524, 1993.

[16] R. G. Jahn, Physics of Electric Propulsion. McGraw-Hill, New York City, New York, 1965.

[17] S. Weston, "State-of-the-art small spacecraft technology," TP-2022–0018058, 2023.

[18] M. Andrenucci, "Magnetoplasmadynamic thrusters," Encyclopedia of Aerospace Engineering, 2010.

[19] H. Alfven, "Existence of electromagnetic-hydrodynamics waves," Nature, vol. 150, pp. 405–406, 1942.

[20] E. L. Resler and W. R. Sears, "The prospects for magneto-aerodynamics," Journal of the Aerospace Sciences, vol. 25, no. 4, pp. 235–245, 1958.

[21] S. Gu and H. Olivier, "Capabilities and limitations of existing hypersonic facilities," Progress in Aerospace Sciences, vol. 113, 2020.

[22] D. R. Lide, "Ionization potentials of atoms and atomic ions," Handbook of Chemistry and Physics, vol. 10, 1992.

[23] T. Trickl, E. F. Cromwell, Y.-T. Lee, and A. H. Kung, "State-selective ionization of nitrogen in the $X^2\Sigma_g^+ v_+ = 0$ and $v_+ = 1$ states by two-color (1+1) photon excitation near threshold," The Journal of Chemical Physics, vol. 91, no. 10, pp. 6006–6012, 1989.

[24] I. V. Adamovich, J. W. Rich, and G. L. Nelson, "Feasibility study of magnetohydrodynamics acceleration of unseeded and seeded airflows," AIAA Journal, vol. 36, no. 4, pp. 590–597, 1998.

[25] J. A. Baughman, D. A. Micheletti, G. L. Nelson, and G. A. Simmons, "Magnetohydrodynamic accelerator research into advanced hypersonics (mariah)," NASA CR-97-206242, 1997.

[26] T. R. Brogan, "The 20MW LORHO MHD accelerator for wind tunnel drive; design, construction and critique," AIAA Plasmaphysics and Lasers Conference, AIAA Paper 99-3720, 1999.

[27] G. L. Whitehead, W. N. MacDermott, L. G. Siler, and R. G. Roepke, "Assessment of MHD applications to hypersonic propulsion testing facilities," AEDC-TMR-87-V54, 1987.

[28] L. E. Rittenhouse, J. C. Pigott, J. M. Whoric, and D. R. Wilson, "Theoretical and experimental results with a linear magnetohydrodynamic accelerator operated in the Hall current neutralized mode," AEDC-TR-67-150, 1967.

[29] C. J. Harris, C. H. Marston, and W. R. Warren Jr., "MHD augmented shock tunnel experiments with unseeded, high density air flows," AIAA Journal, vol. 13, no. 2, pp. 229–231, 1975.

[30] G. P. Wood and A. F. Carter, "NASA considerations in the design of steady D.C. plasma accelerators," NASA Langley Research Center, 1963.

[31] A. F. Carter, R. W. Willard, D. R. McFarland, and G. P. Wood, "Development and initial operating characteristics of the 20-megawatt linear plasma accelerator facility," NASA TN D-6457, 1971.

[32] A. F. Carter, G. P. Wood, D. R. McFarland, and W. R. Weaver, "Research on a one-inch-square linear D-C plasma accelerator," AIAA 4th Electric Propulsion Conference, AIAA Paper 64-699, 1964.

[33] A. F. Carter, G. P. Wood, D. R. McFarland, W. R. Weaver, and S. K. Park, "Operating characteristics, velocity and pitot distribution, and material evaluation tests in the langley one-inch-square plasma accelerator," AIAA Plasmadynamics Conference, AIAA Paper 66-180, 1966.

[34] W. R. Grabowsky, D. A. Durran, and H. Mirels, "Performance of a 500-kJoule MHD wind tunnel," AIAA Journal, vol. 7, no. 10, pp. 1846–1852, 1969.

[35] S. R. Pate, L. G. Siler, D. W. Stallings, and D. A. Wagner, "Development of an MHD-augmented, high enthalpy, shock tunnel facility," AIAA Journal, vol. 12, no. 3, 1974.

[36] V. I. Alferov, "Current status and potentialities of wind tunnels with MHD acceleration," High Temperature, vol. 38, pp. 300–313, 2000.

[37] R. J. Litchford, J. W. Cole, J. T. Lineberry, J. N. Chapman, H. J. Schmidt, and C. W. Lineberry, "Magnetohydrodynamic augmented propulsion experiment: I. performance analysis and design," NASA TP, vol. 2003-212285, 2003.

[38] R. J. Litchford and J. T. Lineberry, "Status of magnetohydrodynamic augmented propulsion experiment," 38th AIAA Plasmadynamics & Lasers Conference, AIAA Paper 07-3884, 2007.

[39] S. O. Macheret, M. N. Shneider, R. B. Miles, and R. L. Lipinski, "Electron-beam-generated plasmas in hypersonic magnetohydrodynamic channels," AIAA Journal, vol. 39, no. 6, 2001.

[40] M. L. Laster, C. C. Limbaugh, and J. L. Jordan, "RDHWT/MARIAH II hypersonic wind tunnel research program," AEDC-TR-08-20, 2008.

[41] D. S. Baranov, V. A. Bityurin, A. N. Bocharov, S. S. Bychkov, V. A. Grushin, N. V. Tretyakova, N. I. Batura, E. B. Vasilevsky, N. G. Zhurkin, and N. M. Kolushov, "Flow characteristics in the water-cooled channel of the MHD accelerator," Journal of Physics: Conference Series, vol. 1112, 2018.

[42] E. L. Resler and W. R. Sears, "Magneto-gasdynamic channel flow," Journal of Applied Mathematics and Physics (ZAMP), vol. 9, pp. 509–518, 1958.

[43] L. E. Ring, "General considerations of MHD acceleration for aerodynamic testing," AEDC-TDR-64-256, 1964.

[44] R. J. Rosa, Magnetohydrodynamic Energy Conversion. McGraw-Hill, New York City, NY, 1968.

[45] J. A. Shercliff, A Textbook of Magnetohydrodynamics. Pergamon Press, Oxford, 1965.

[46] R. A. Crawford, J. N. Chapman, and R. P. Rhodes, “Potential application of magnetogydrodynamic acceleration to hypersonic environmental testing,” AEDC-TR-90-6, 1990.

[47] B. L. Liu, J. T. Lineberry, and H. J. Schmidt, “Three-dimensional fluid and electrodynamic modeling for MHD DCW channels,” AIAA 21st Aerospace Sciences Meeting, AIAA Paper 83-0464, 1983.

[48] E. P. Gurijanov and P. T. Harsha, “AJAX: New directions in hypersonic technology,” Space Plane and Hypersonic Systems and Technology Conference, AIAA Paper 1996-4609, 1996.

[49] S. O. Macheret, M. N. Shneider, and R. B. Miles, “Magnetohydrodynamic control of hypersonic flows and scramjet inlets using electron beam ionization,” AIAA Journal, vol. 40, no. 1, 2002.

[50] B. Parent and I.-S. Jeung, “Fuel-cell-powered magnetoplasma jet engine with electron beam ionization,” Journal of Propulsion and Power, vol. 21, no. 3, pp. 433–441, 2005.

[51] B. Parent, S. Macheret, M. Shneider, and N. Harada, “Numerical study of an electron-beam-confined faraday accelerator,” Journal of Propulsion and Power, vol. 23, no. 5, 2007.

[52] G. V. Gaitonde, “Magnetohydrodynamic energy-bypass procedure in a three-dimensional scramjet,” Journal of Propulsion and Power, vol. 22, no. 3, pp. 498–510, 2006.

[53] M. Anwari, N. Sakamoto, T. Hardianto, J.-I. Kondo, and N. Harada, “Numerical analysis of magnetohydrodynamic accelerator performance with diagonal electrode connection,” Energy Conversion and Management, vol. 47, no. 13, pp. 1857–1867, 2006.

[54] M. Anwari, S. Takahashi, and N. Harada, “Numerical simulation for the performance of a magnetohydrodynamic accelerator,” Transactions of the Japan society for Aeronautical and Space Sciences, vol. 48, no. 160, pp. 57–62, 2005.

[55] N. Harada, J. Ikewada, and Y. Terasaki, “Basic studies on an MHD accelerator,” in 33rd Plasmadynamics and Lasers Conference, (Maui, Hawaii), American Institute of Aeronautics and Astronautics, 2002.

[56] M. Turner, C. Hawk, and R. Litchford, “Three-dimensional numerical modeling of the magnetohydrodynamic augmented propulsion experiment,” 46th AIAA Aerospace Sciences Meeting and Exhibit, 2008.

[57] B. Parent, M. N. Shneider, and S. O. Macheret, “Detailed modeling of plasmas for computational aerodynamics,” AIAA Journal, vol. 54, no. 3, pp. 898–911, 2016.

[58] B. Parent, S. O. Macheret, and M. N. Shneider, “Electron and ion transport equations in computational weakly-ionized plasmadynamics,” Journal of Computational Physics, vol. 259, pp. 51–69, 2014.

[59] V. A. Bityurin, A. N. Bocharov, and N. A. Popov, “Numerical simulation of an electric discharge in supersonic flow,” Fluid Dynamics, vol. 43, no. 4, pp. 642–653, 2008.

[60] J. Poggie, “Numerical simulation of direct current glow discharges for high-speed flow control,” Journal of Propulsion and Power, vol. 24, no. 5, pp. 916–922, 2008.

[61] S. T. Surzhikov and J. S. Shang, "Two-component plasma model for two-dimensional glow discharge in magnetic field," Journal of Computational Physics, no. 2, pp. 437–464, 2004.

[62] A. L. Ward, "Effect of space charge in cold-cathode gas discharges," Physical Review, vol. 112, no. 6, pp. 1852–1857, 1958.

[63] Y. P. Raizer, Gas Discharge Physics. Springer-Verlag, New York City, New York, 1987.

[64] M. D. Atkinson, J. Poggie, and J. A. Camberos, "Control of separated flow in a reflected shock interaction using a magnetically-accelerated surface discharge," Physics of Fluids, vol. 24, no. 12, 2012.

[65] T. Wan, G. V. Candler, S. O. Macheret, and M. N. Shneider, "Three-dimensional simulation of the electric field and magnetohydrodynamic power generation during reentry," AIAA Journal, vol. 47, no. 6, pp. 1327–1336, 2009.

[66] Y. Imamura and T. Fujino, "Numerical simulation of magnetohydrodynamic flow control in reentry flight with three-temperature model," in 2018 AIAA Aerospace Sciences Meeting, American Institute of Aeronautics and Astronautics, 2018.

[67] A. Martin, L. C. Scalabrin, and I. D. Boyd, "High performance modeling of atmospheric re-entry vehicles," Journal of Physics: Conference Series, vol. 341, Article 012002, 2012.

[68] N. J. Bisek, I. D. Boyd, and J. Poggie, "Numerical study of magnetoaerodynamic flow around a hemisphere," Journal of Spacecraft and Rockets, vol. 47, pp. 816–827, 2010.

[69] B. Parent, M. N. Shneider, and S. O. Macheret, "Sheath governing equations in computational weakly-ionized plasmadynamics," Journal of Computational Physics, vol. 232, no. 1, pp. 234–251, 2013.

[70] W. G. Vincenti and C. H. Kruger, Introduction to Physical Gas Dynamics. Kreiger Publishing Company, Malabar, Florida, 1965.

[71] G. J. M. Hagelaar and L. C. Pitchford, "Solving the boltzmann equation to obtain electron transport coefficients and rate coefficients for fluid models," Plasma Sources Science and Technology, vol. 14, no. 4, pp. 722–733, 2005.

[72] I. D. Boyd, G. Chen, and G. V. Candler, "Predicting failure of the continuum fluid equations in transitional hypersonic flows," Physics of Fluids, vol. 7, pp. 210–219, 1995.

[73] C. Park, "Assessment of two-temperature kinetic model for ionizing air," Journal of Thermophysics and Heat Transfer, vol. 3, no. 3, pp. 233–244, 1989.

[74] J. H. Lee, "Basic governing equations for the flight regimes of aeroassisted orbital transfer vehicles," 19th Thermophysics Conference, AIAA paper 84-1729, 1984.

[75] P. A. Gnoffo, R. N. Gupta, and J. L. Shinn, "Conservation equations and physical models for hypersonic air flows in thermal and chemical nonequilibrium," NASA TP 2867, 1989.

[76] J. J. Shang, Computational Electromagnetic Aerodynamics. Wiley, Hoboken, New Jersey, 2016.

[77] L. Scalabrin, Numerical Simulation of Weakly Ionized Hypersonic Flow Over Reentry Capsules. PhD thesis, University of Michigan, 2007.

[78] G. Karypis and V. Kumar, "A fast and high quality multilevel scheme for partitioning irregular graphs," SIAM Journal on Scientific Computing, vol. 20, no. 1, pp. 359–392, 1998.

[79] C. Park, "Review of chemical-kinetic problems of future NASA missions. I - Earth entries," Journal of Thermophysics and Heat Transfer, vol. 7, no. 3, pp. 385–398, 1993.

[80] R. S. Chaudhry, Modeling and Analysis of Chemical Kinetics for Hypersonic Flows in Air. PhD thesis, University of Minnesota, 2018.

[81] R. S. Chaudhry, I. D. Boyd, E. Torres, T. E. Schwartzentruber, and G. V. Candler, "Implementation of a chemical kinetics model for hypersonic flows in air for high-performance CFD," AIAA SciTech 2020 Forum, AIAA Paper 2020-2191, 2020.

[82] K. Sutton and P. Gnoffo, "Multi-component diffusion with application to computational aerothermodynamics," 7th AIAA/ASME Joint Thermophysics and Heat Transfer Conference, AIAA Paper 98-2575, 1998.

[83] F. G. Blottner, M. Johnson, and M. Ellis, "Chemically reacting viscous flow program for multi-component gas mixtures," Technical Report SC-RR-70-754, 1971.

[84] C. R. Wilke, "A viscosity equation for gas mixtures," The Journal of Chemical Physics, vol. 18, no. 4, pp. 517–519, 2004.

[85] G. E. Palmer and M. J. Wright, "Comparison of methods to compute high-temperature gas viscosity," Journal of Thermophysics and Heat Transfer, vol. 17, no. 2, pp. 232–239, 2003.

[86] T. E. Magin and G. Degrez, "Transport algorithms for partially ionized and unmagnetized plasmas," Journal of Computational Physics, vol. 198, no. 2, pp. 424–449, 2004.

[87] H. Alkandry, I. Boyd, and A. Martin, "Comparison of models for mixture transport properties for numerical simulations of ablative heat-shields," 51st AIAA Aerospace Sciences Meeting including the New Horizons Forum and Aerospace Exposition, 2013.

[88] R. N. Gupta, J. M. Yos, R. A. Thompson, and K.-P. Lee, "A review of reaction rates and thermodynamic and transport properties for an 11-species air model for chemical and thermal nonequilibrium calculations to 30000 K," NASA RP-1232, 1990.

[89] M. J. Wright, D. Bose, G. E. Palmer, and E. Levin, "Recommended collision integrals for transport property computations part 1: Air species," AIAA Journal, vol. 43, no. 12, pp. 2558–2564, 2005.

[90] D. Gaitonde and J. Poggie, "Elements of a numerical procedure for 3-D MGD flow control analysis," 40th AIAA Aerospace Sciences Meeting & Exhibit, AIAA Paper 2002-0198, 2002.

[91] D. V. Gaitonde, "A high-order implicit procedure for the 3-D electric field in complex magnetogasdynamic simulations," Computers & Fluids, vol. 33, no. 3, 2004.

[92] E. H. Niewood and M. Martinez-Sanchez, "Quasi-one-dimensional numerical simulation of magnetoplasmadynamic thrusters," Journal of Propulsion and Power, vol. 8, no. 5, pp. 1031–1039, 1992.

[93] K. Tang and K. Hara, "Numerical study of ionized nozzle flows with electromagnetic propulsion enhancement," AIAA Aviation 2021 Forum, 2021.

[94] J. D. Anderson, Fundamentals of Aerodynamics. McGraw-Hill, New York City, New York, 2007.

[95] US Standard Atmosphere, 1976. National Oceanic and Atmospheric Administration, National Aeronautics and Space Administration, United States Air Force, 1976. Accessed: 2023-09-29.

[96] Y. Itikawa, M. Hayashi, A. Ichimura, K. Onda, K. Sakimoto, K. Takayanagi, M. Nakamura, H. Nishimura, and T. Takayanagi, "Cross sections for collisions of electrons and photons with nitrogen molecules," Journal of Physical and Chemical Reference Data, vol. 15, no. 3, pp. 985–1010, 1986.

[97] Y. Itikawa, "Cross sections for electron collisions with nitrogen molecules," Journal of Physical and Chemical Reference Data, vol. 35, no. 1, pp. 31–53, 2006.

[98] Y. Tsujikawa and G. B. Northam, "Optimization of scramjet engine performance with the three-temperature flow model," International Journal of Hydrogen Energy, vol. 20, no. 7, pp. 593–599, 1995.

[99] T. E. Kava, J. A. Evans, and I. D. Boyd, "Numerical simulation of electron-beam powered plasma fueled engines," AIAA Propulsion and Energy 2021 Forum, 2021.

[100] M. Suzuki, T. Taniguchi, and H. Tagashira, "Momentum transfer cross section of argon deduced from electron drift velocity data," Journal of Physics D: Applied Physics, vol. 23, no. 7, pp. 842–850, 1990.

[101] A. Bogaerts, "Effects of oxygen addition to argon glow discharges: A hybrid monte carlo-fluid modeling investigation," Spectrochimica Acta Part B: Atomic Spectroscopy, vol. 64, pp. 1266–1279, 2009.

[102] S. Neeser, T. Kunz, and H. Langhoff, "A kinetic model for the formation of Ar_2 excimers," Journal of Physics D: Applied Physics, vol. 30, no. 10, p. 1489, 1997.

[103] Y. Ikezoe, S. Matsuoka, M. Tekebe, and A. Viggiano, Gas Phase Ion-molecule Reaction Rate Constants Through 1986. Ion Reaction Research Group of the Mass Spectroscopy Society of Japan, 1987.

[104] F. J. Mehr and M. A. Biondi, "Electron-temperature dependence of electron-ion recombination in argon," Physical Review, vol. 176, pp. 322–326, 1968.

[105] Kimball Physics. `https://www.kimballphysics.com/product-category/electron-gun-systems/`. Accessed: 2023-08-15.

[106] J. L. Kerrebrock, "Nonequilibrium ionization due to electron heating - I - theory," AIAA Journal, vol. 2, no. 6, pp. 1072–1080, 1964.

[107] E. P. Velikhov, "Hall instability of current-carrying slightly-ionized plasmas," in Proceedings of 1st International Conference on MHD Electrical Power Generation, Newcastle upon Tyne, pp. 135–162, 1962.

[108] J. P. Petit and J. Geffray, "Non-equilibrium plasma instabilities," Acta Physica Polonica A, vol. 115, no. 6, pp. 1170–1172, 2009.

[109] K. M. Sayler, "Hypersonic weapons: Background and issues for congress," Congressional Research Service, 2023.

[110] Space Foundation, "2022 annual report," 2022.